Computational screening strategies for rational biocatalyst and electrocatalyst design and development

by

Ashraf Ali

A Dissertation Submitted to the Graduate Faculty of
Auburn University
In partial fulfilment of the
Requirements for the Degree of
Doctor of Philosophy

Auburn, Alabama
August 06, 2022

Keywords: Biocatalyst, electrocatlayst, computational chemistry,
multiscale modeling, protease, hydrogen generation

Approved by

Dr. Andrew J. Adamczyk, Chair, Assistant Professor, Department of Chemical Engineering,
Dr. Allan E. David, Associate Professor, Department of Chemical Engineering,
Dr. Christopher A. Kieslich, Assistant Professor, Department of Chemical Engineering,
Dr. J. Vincent Ortiz, Professor, Department of Chemistry and Biochemistry,
Dr. Xinyu Zhang, Professor, Department of Chemical Engineering,

Abstract

In most of the important aspects of modern civilization such as food production, energy usage, or biomedical and biochemical advances, catalysis plays a crucial role in supporting these efforts. For a greener and sustainable future, catalysis research has been increased many-fold, and one of the first steps toward this end is to understand the fundamental structure-property relationships underlying catalysis for crucial systems. Another critical step to advancing the field of catalysis is to look into the microscopic details of the underlying reaction pathways and key intermediates. In order to probe these steps and gain new insights, computational modeling employing computational chemistry and chemical engineering principles from the atomistic to macroscopic levels is a potent tool. In the dissertation presented, the catalytic phenomena of enzyme and electrolysis is elucidated with computational chemistry tools.

In the study of biocatalysis, the activity of one of the most commonly used industrial biocatalysts, serine protease, has been explored to provide new insights. The reaction pathway analysis of serine protease is investigate using quantum mechanical cluster (QM-cluster) calculations with density functional theory (DFT). A new pathway has been proposed to resolve the long standing debate surround the His-flip mechanism established in literature. The Gibbs free energy of activation, rate coefficient, and the Gibbs free energy of reaction are used compare the both pathways. With these critical thermochemical and kinetic parameters, detailed reaction path analysis has been performed on a peptide bond cleavage by the active site of a serine protease, and hitherto results of this study indicate the viability of the proposed pathway.

In the study of electrocatalysis, first, a systematic study of various non-hybrid and hybrid molybdenum dichalcogenides/graphene ($MoCh_2$/Gr; Ch = S, Se, Te) nanocomposite for the hydrogen evolution reaction (HER) has been performed using periodic plane-wave DFT calculations. The electronic structure, adsorption energetics, and adsorption site specificity for hydrogen adsorption for several different catalytic sites on the nanocomposite have been investigated. Combining the computational results with experimental descriptors provided by a collaborative group, screening of $MoCh_2$/Gr materials for HER electrocatalyst is carried out, MoSTe/Gr is found to be the best cathodic material for HER.

In the second project of electrocatalysis, a rational strategy has been developed to design a better cathodic material for HER. The material for this catalyst is based on the result of previous project: molybdenum sulfotelluride/graphene (MoS_xTe_y/Gr) nanocomposite. Molecular modeling studies have been performed with periodic plane-wave DFT, and hydrogen binding energetics for various MoS_xTe_y/Gr is carried out with multiple ratio of Mo, S, and Te. These studies show that the nanocomposites consisting of slightly more Te than S atom and higher amount of Mo than the stoichiometric ratio should demonstrate enhancement in catalytic performance. An independent experimental study performed by a collaborative group supported these computational findings.

Acknowledgements

I would like to first express my gratitude to my advisor, Professor Andrew J. Adamczyk. He set himself as an example of hard work, tenacity, thoughtfulness, and inquisitiveness, which is essential for being a successful researcher. I want to thank my committee members: Professor Vincent Ortiz, Professor Xinyu Zhang, Professor Allan David, and Professor Christopher Kieslich, along with my university dissertation reader Professor Ryan Comes, for their guidance and essential suggestions. I am gratefully indebted to my committee for their time and patience.

I would also like to especially thank all my group members, Yeseul Choi, Katherine Lawson, Siyuan Wu, and Tanzina Azad (colleague in both life and work) for their kind support and valuable discussions. I would also like to thank all faculty members, staff, and especially my friends inside and outside the Department of Chemical Engineering at Auburn University. Finally, I would like to extend a special thank you to my mother, brothers, and again my wife, Tanzina Azad. Whatever distance I have walked, most of its credit goes to them.

Table of Contents

List of Figures

List of Tables

List of Abbreviations:

Abbreviation	Elaboration
*	Adsorption site in the electrocatalyst
[X]	Concentration of chemical species X
a	Tafel constant
AO	Atomic orbital
b	Tafel Slope
BEP	Brønsted(/Bell)-Evans-Polanyi Principles.
B3LYP	Becke, 3-parameter, Lee–Yang–Parr exchange-correlation functional
BLYP	Becke88 exchange and the Lee-Yang-Parr correlation functional
COSMO	Conductor like screening model
DFT	Density functional theory
DNP	Double numerical plus polarization basis set
E	Energy
E^0	Standard thermodynamic potential of an electrolytic cell
e	Elementary charge, 1.602×10^{-19} C
e^-	An electron
E_a	Activation energy
ERK	Extracellular signal-regulated kinase. An MAPK type enzyme.
EVB	Empirical valence bond theory
F	Faraday constant, 96485.33 C $\cdot$ mol^{-1}
FEP	Free energy perturbation
G	Gibbs free energy
GGA	Generalized gradient approximation
H	Enthalpy
$\hat{H}$	Hamiltonian Operator
H*	Adsorbed hydrogen atom on electrocatalyst surface.
h	Planck constant, 6.626×10^{-34} J $\cdot$ s
$\hbar$	Reduced Planck Constant, 1.0546×10^{-34} J $\cdot$ s
H-F	Hartree-Fock method
HER	Hydrogen evolution reaction
i	Current density of hydrogen evolution reaction
i_0	Exchange current density of hydrogen evolution reaction
KP	Catalytic proficiency. The ratio of the rate of catalyzed and uncatalyzed reaction
k	Reaction rate constant
K_{eq}	Equilibrium constant of a chemical reaction
k_B	Boltzmann constant, 1.381×10^{-23} J $\cdot$ K^{-1} or 3.298×10^{-27} kcal $\cdot$ K^{-1}
LCAO	Linear combination of atomic orbital
LRA	Linear response approximation
MM	Molecular Mechanics
MO	Molecular orbital

Abbreviation	Elaboration
N_A	Avogadro number, $6.022 \times 10^{-23} \text{mol}^{-1}$
OER	Oxygen evolution reaction
P	Pressure
PBE	Perdew–Burke-Ernzerhof functional
QM	Quantum Mechanics
R	Universal gas constant, $8.314 \text{J} \cdot \text{K}^{-1}\text{mol}^{-1}$ or $1.987 \times 10^{-3} \text{kcal} \cdot \text{K}^{-1}\text{mol}^{-1}$
S	Entropy
SCF	Self-consistent field method
T	Temperature
$\hat{T}$	Kinetic energy operator
T_D	Debye temperature
TMD	Targeted molecular dynamics
TNP	Triple numerical plus polarization basis set
TPSD	Two point steep descent method
TS	Transition state
V	Potential Energy
VBT	Valence bond theory
α	Symmetry factor of the electrode
β	Variations in the rate constant of the Brønsted-Evans-Polanyi coefficient
Δ	Denotes changes (from initial to final)
ε_i	Energy of ith Kohn-Sham orbital
η	Overpotential
ν	Reaction rate of hydrogen evolution reaction
Ψ/ψ	Wave function

1. Introduction:

1.1. Introduction to Catalysis:

From the beginning of life on earth to modern-day civilization, catalysts play crucial roles by efficiently accelerating essential chemical and biochemical reactions. The annual catalyst-manufacturing business was valued at around 18 billion USD in 2019 with a 4.4% complex annual growth rate (CAGR)[1], where more than 30% of the global gross domestic product (GDP) depends on industrial catalysis[2,3]. In addition to the fact that more than 80% of industrial chemical processes depend on catalysts[4], the practicing chemical engineer uses catalysis mainly for three reasons in process scale-up efforts. Firstly, catalysts make reaction rates faster, thus shortening the production time. Secondly, catalysts can make reactions occur in relatively milder conditions (i.e., lower pressure and temperature) in many situations, thus saving energy. Finally, catalysts help increase the selectivity of desired products relative to undesired products, resulting in a decrease in the production of waste and lower cost in separations processes. These three aspects are also essential for a greener and sustainable future.

The term catalysis for the current chemical context was coined by Jön Jacob Berzelius in 1835. However, the concept of catalysis was first discovered and described by the Scottish scientist Elizabeth Fulhame in 1794. The etymological source of the term is the ancient Greek word κατλύεινω (pronunciation: ka.taˈly.o) meaning unbind or loosen.

By definition, a catalyst is generally a substance added to a reacting mixture that can change (generally increase) the rate of a specific chemical reaction without itself being consumed

in the reaction.[5] Catalysis is classified broadly into four classes: positive catalysis, negative catalysis, auto-catalysis, and induced catalysis.

In positive catalysis, the catalyst increases the rate of a chemical reaction. Commonly, when the word catalysis is mentioned, it generally refers to positive catalysis.

Negative catalysis is the process where the presence of a specific substance (also known as a reaction inhibitor) decreases the rate of a chemical reaction. An example is the decomposition of hydrogen peroxide, where the reaction rate is reduced in the presence of acetanilide (N-Phenylethanamide). Similarly, presence of alcohol acts as a negative catalyst for the oxidation of chloroform.

$$2H_2O_{2\ (aq.)} \xrightarrow{-\ (C_6H_5NH-CO-CH_3)} 2H_2O_{(l)} + O_{2\ (g)}$$

$$2CHCl_{3\ (l)} + O_{2\ (g)} \xrightarrow{-\ (C_2H_5OH)} 2COCl_{2\ (g)} + 2HCl_{(g)}$$
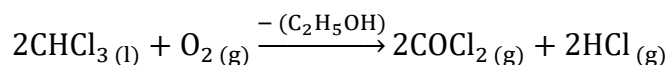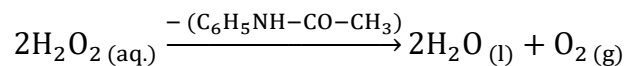
In autocatalysis, the product of a chemical reaction acts as a catalyst and increases the reaction rate. For example, in the reduction reaction of permanganate, the product manganese ion behaves as a catalyst. In the case of hydrolysis of ethyl acetate, the product acetic acid also acts as an autocatalyst.

$$2MnO_{4\ (aq.)}^{-} + 5(HOOC)_{2\ (aq.)} + 6H_{(aq.)}^{+} \xrightarrow{Mn_{(aq.)}^{2+}} 2Mn_{(aq.)}^{2+} + 10CO_{2\ (g)} + 8H_2O$$

$$CH_3COOC_2H_{5\ (aq.)} + H_2O \xrightarrow{CH_3COOH_{(aq.)}} CH_3COOH_{(aq.)} + C_2H_5OH_{(aq.)}$$
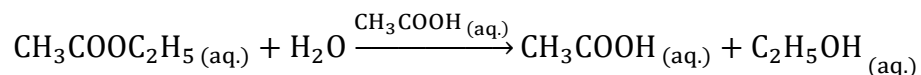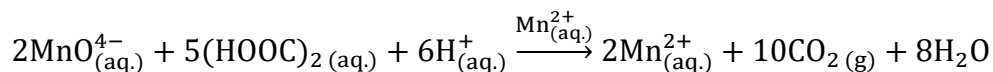
In induced catalysis, the rate of reaction increases due to another chemical reaction, not due to any specific catalyst. An example is the oxidation of sodium arsenite (Na$_2$AsO$_3$), which does not occur with the presence molecular oxygen in air. However if it is mixed with sodium sulphite (Na$_2$SO$_3$), oxidization happens to both substances with increased reaction rates. Another example is the reduction of HgCl$_2$ by oxalic acid, which is also catalyzed inductively by the reduction of acidic KMnO$_4$.

$$Na_2AsO_3 + \frac{1}{2}O_2 \xrightarrow{Na_2SO_3 + \frac{1}{2}O_2 \rightarrow Na_2SO_4} Na_2AsO_4$$

$$2HgCl_2 + (COOH)_2 \xrightarrow{2KMnO_4 + 6HCl + 5(COOH)_2 \rightarrow 2KCl + 2MnCl_2 + 8H_2O + 10CO_2} Hg_2Cl_2 + 2HCl + 2CO_2$$
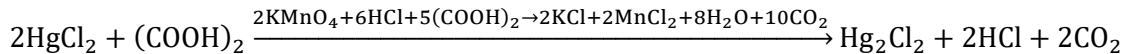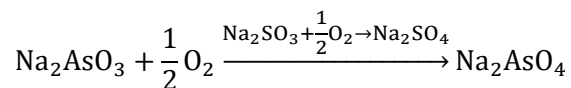
Our research is focused on **positive catalysis**, and in this document, the term "**catalysis**" will be used instead of "**positive catalysis**" unless otherwise stated.

Catalysis is not a thermodynamic but a kinetic phenomenon. It increases both forward and backward rate of the reactions. Thus, catalysis cannot change the extent of reactions or the equilibrium constant. It simply serves as a means to reach chemical equilibrium faster. The change in the reaction rate occurs due to the change in the energy difference between reactants and the transition states, usually known as activation energy barrier. Catalysts achieve this through multiple ways, e.g. stabilizing the transition state thus lowering the free energy, or by accessing an alternative reaction pathway through different transition state(s). These different catalytic processes for catalysis are illustrated in figure 1.1. Furthermore, catalysts are broadly classified based on their phase and phase of reactants (or substrates). The three types of catalysts are, homogeneous catalyst, heterogeneous

catalyst, and biocatalyst. Homogeneous catalysts function in the same phase as the reactants, generally in solution phase. Heterogeneous catalysts function in a different phase
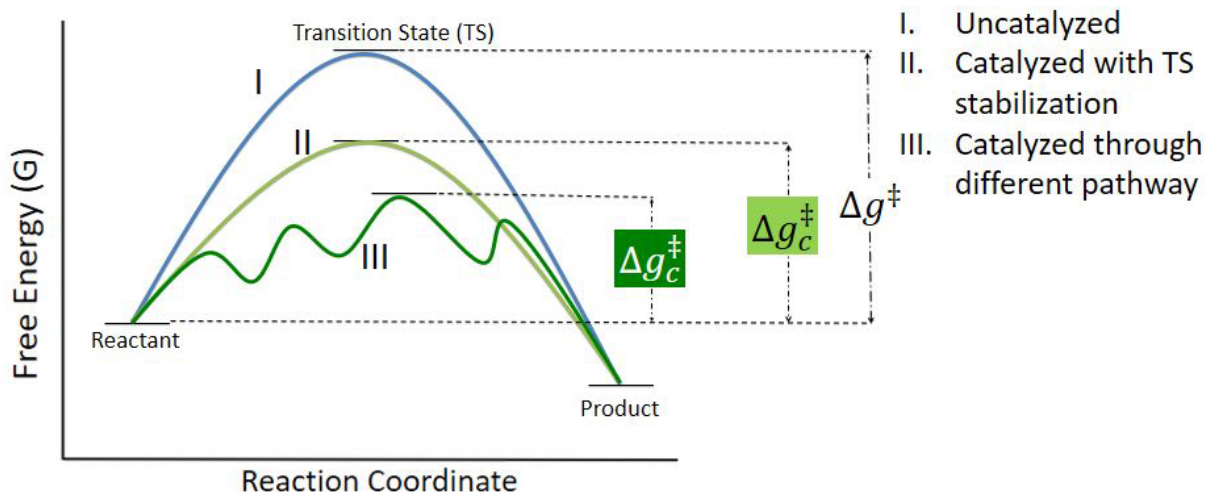
Figure 1.1: Comparative reaction energy profiles (Gibbs free energy vs. reaction coordinate) of catalyzed and uncatalyzed reactions.

(e.g., solid) than the reactants (e.g., liquid or gaseous). Electro-catalysts are a special type of heterogeneous catalyst which catalyze electrochemical reactions while acting simultaneously as an electrode. Lastly, biocatalysts function by catalyzing virtually all metabolic reactions pertaining to life from bacteria to humans. Most biocatalysts are globular proteins called enzymes. Enzymes can function as homogeneous or heterogeneous catalysts, and thus enzymes are considered as an intermediate between the two catalyst types and classified separately as biocatalysts.

1.2. Enzymes and Electrocatalysts for a Sustainable Future:

The importance of environment and eco-friendly technologies in the fields of science and engineering has become apparent since the publication of the 'Silent Spring' by Rachel Carson and other similar books in the 1960s.[6,7] It developed into a robust discipline of science and engineering in the 1990s and become known as green technology or sustainable technology, with twelve guiding principles.[8–10] These principles are prevention of waste, atom economy, less hazardous chemical synthesis, safer chemical design, use of benign solvents and auxiliary, use of renewable raw materials, minimizing the generation of derivatives, catalysis, designing ecofriendly degradation of materials, real-time monitoring and controlling the pollution, and using inherently safer chemistry and process.

Catalysis plays a key role among the above mentioned twelve points, since it allows attaining atom economy and minimizing the generation of derivatives (through raising selectivity) and converting the process inherently safer (by reaction occurring in relatively milder conditions). Since the inception of Green Chemistry Challenge Awards in 1996, catalytic process and products are frequently awarded by US environment protection agency (EPA).[11] Among the various type of catalysts, electrocatalysts and biocatalysts hold more promises than the homogenous and heterogeneous catalysis. One of the problems of heterogeneous catalysis is the harsh reaction conditions, and in case of homogeneous catalyst, the solvent in many cases are not necessarily benign and the catalyst recovery can be very expensive.[12] The general focuses of this research (i.e. biocatalysts and the electrocatalyst for hydrogen generation (HER)) have the common theme of green catalysis.

Biocatalysis has a great potential for green technology, since it can provide mild reaction conditions (pH and temperature), and the catalysts (enzymes) and the solvent (usually water) are environmentally compatible. Enzymes also have very high selectivity, thus high atom economy. Almost all enzymes are safe catalysts: non-flammable, non-toxic, and non-toxic. The ecofriendly applications of enzymes for many industrial sectors are already in places. Especially hydrolytic enzymes (hydrolases) are used in pulp and paper industry, laundry and dishwashing detergents, industrial/medical cleaning puposes.

Electrocatalysts allow efficient conversion of electrical energy to chemical energy and vice versa. Since production of electricity from renewable and environment friendly sources such as solar, wind, and water has become economically competitive, electrocatalysts are showing a lot of promises for diverse applications. Research on electrocatalysis spans transition to clean energy, energy storage, CO_2 capture, electrosynthesis of important small molecules (NH_3, hydrocarbons, alcohols), and electrosysnthesis of more complex organic reactions. A great advantage of elctrocatalysis is the relatively safer process due to milder reaction conditions. Electrocatalytic generation of molecular hydrogen (H_2) is one of the cleanest and atom efficient raw materials with diverse applications.[13,14]

Chemical engineering is a diverse multidisciplinary branch of engineering that has been playing a key role in the developments of green technology since its inception. Multiscale modeling techniques provide a versatile toolbox for the chemical engineering research in the fields of sustainable technology and catalysis.[15]

Multiscale modeling can be defined as a methodology to solve problems by spanning multiple scales of time and/or length. In multiscale (also known as multilevel) modelling, usually the following strata are distinguished, e.g. quantum mechanical models

(information about electrons), molecular mechanics/dynamics (information about individual atoms), coarse grained models (information about atoms and/or groups of atoms), continuum models, and process level macroscale models (Figure 1.2).[15]
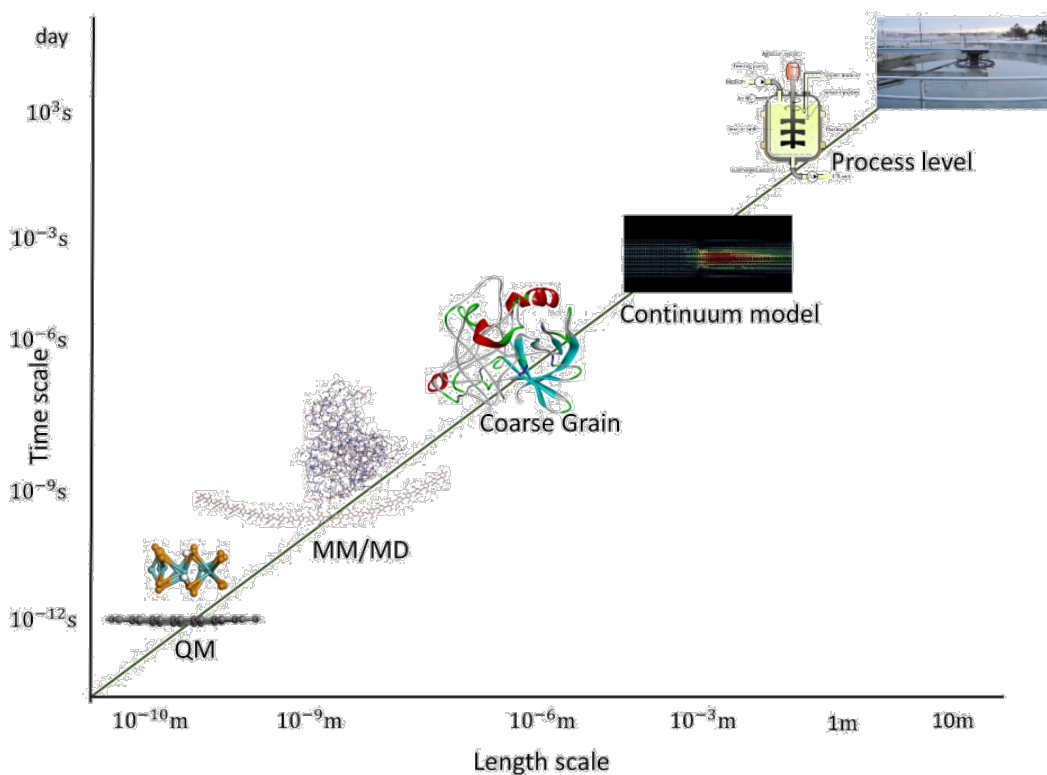
Figure 1.2: A general schematic for multiscale modeling at various time and length scale

Computational chemistry or molecular modeling (i.e. the first three levels described in Figure 1.2) provides the fundamental insights of the multiscale modeling used in key structure-property relationships.[16–18]

In this research, the reaction pathway analysis, thermodynamic and kinetic properties have been probed with the molecular modeling. These insights provides the pivotal parameters

for designing process level reactors and catalysts by way of more traditional chemical reaction engineering principles.[19–21]
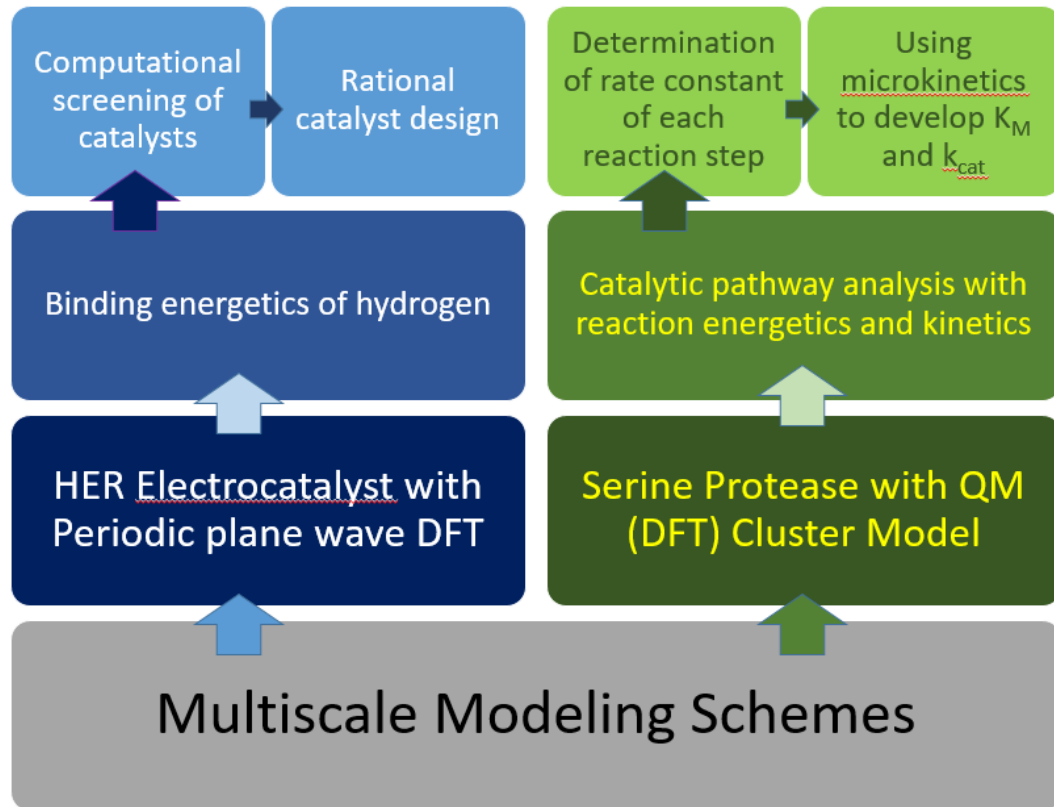
Figure 1.3: Connectivity of studied research project topics and objectives

1.3. Background physical theory:

Physical laws describing the world, are conventionally categorized into two strata: classical and quantum. Most of the common day observable phenomena can be described by classical mechanics, which is deterministic and continuous in nature. Quantum mechanics (QM) come into play in the realm of extremely small scale (e.g. fundamental particles such as electrons, neutrons, and protons). The main features of QM are discrete values (quantization), the wave-particle duality of objects, the effect of measurement on the system (uncertainty principle), and inherent probabilistic nature. In QM, all measurable quantities are called observables, and each observable is associated with a mathematical operation called an operator which imparts specific mathematical properties when applied. These operators work on a certain mathematical function called quantum state or wave function (typically denoted as ψ or Ψ). The wavefunction (ψ/Ψ) can provide the probability of values for certain observables, when attached to the pertaining operator. One of the ways to determine the wave function is solving of time-dependent Schrödinger equation.

$$\widehat{H}\Psi(r,t) = i\hbar \frac{\partial \Psi(r,t)}{\partial t}$$

Here, $\widehat{H}$ is called Hamiltonian operator and $\hbar$ is the reduced Planck's constant. For a single nonrelativistic particle, the Schrödinger equation can be represented by the equation below. The Hamiltonian operator representing the total energy of the system can be expanded into two operating terms which provide information on the respective kinetic and potential energies of a single nonrelativistic particle.

$$i\hbar \frac{\partial}{\partial t}\Psi(r,t) = \left[-\frac{\hbar^2}{2m}\nabla^2 + V(r,t)\right]\Psi(r,t)$$

As mentioned, the two equations shown above are also known as the time-dependent Schrödinger equation. However, the structural and electronic properties of atoms or molecules can be approximately described with a simpler formalism known as time-independent Schrödinger equation. The corresponding equations are

$$\hat{H}\psi(r) = E\psi(r)$$

and for single nonrelativistic particle

$$\left[-\frac{\hbar^2}{2m}\nabla^2 + V(r)\right]\psi(r) = E\psi(r)$$

In the time independent Schrödinger equation, the Hamiltonian operator $(\hat{H})$ is still described as a sum of the kinetic energy operator and the potential energy operator. E represents the discrete energy values which are allowed for the system (also called energy eigenvalues).

For the sake of simplification, considering atoms and molecules are consisted of only nuclei and electrons and only electrostatic potentials exist among each the electrons and nuclei, the time-independent Schrödinger equation becomes

$$\left\{ -\frac{\hbar^2}{2}\left[\sum_i \frac{1}{m_e}\nabla_i^2 + \sum_i \frac{1}{m_k}\nabla_k^2 \right] - \sum_i \sum_k \frac{e^2 Z_k}{r_{ik}} + \sum_{i<j} \frac{e^2}{r_{ij}} + \sum_{k<l} \frac{Z_k Z_l e^2}{r_{kl}} \right\} \psi(r) = E\psi(r)$$

Here, indices i and j denotes electrons, k and l denotes nuclei, m_e is the mass of an electron, m_k is the mass of a nucleus k, ∇^2 is the Laplacian operator, e is the elementary charge, Z_k is the atomic number of the nucleus k, and r_{mn} is the distance between particles (can be an electron or nucleus) m and n. The nucleus comprised of protons and neutrons is treated as a single lumped particle, and this lumped particle is significantly heavier than an individual electron relatively.

Further simplification of this equation is performed with the Born-Oppenheimer approximation, which states that the motions of nuclei and electrons in a molecule can be treated separately. While considering only the motion of an electron, nuclear motion can be considered stationary compared to electronic motion since nuclei are many thousands fold heavier than electrons. With this approximation, the kinetic energy term for nuclear motion is removed and the repulsion potentials between the nuclei are then considered as constant for a given geometry. The resultant equation becomes

$$\left\{ -\frac{\hbar^2}{2}\sum_i \frac{1}{m_e}\nabla_i^2 - \sum_i\sum_k \frac{e^2 Z_k}{r_{ik}} + \sum_{i<j}\frac{e^2}{r_{ij}} + \sum_{k<l}\frac{Z_k Z_l e^2}{R_{kl}} \right\} \psi_e(r) += E_e \psi_e(r)$$

$$\left(\widehat{H}_e + V_N\right)\psi_e = E_e \psi_e$$

Here $\widehat{H}_e = -\frac{\hbar^2}{2}\sum_i \frac{1}{m_e}\nabla_i^2 - \sum_i\sum_k \frac{e^2 Z_k}{r_{ik}} + \sum_{i<j}\frac{e^2}{r_{ij}}$ and $V_N = \sum_{k<l}\frac{Z_k Z_l e^2}{R_{kl}}$

Here, the subscript e denotes application of the Born-Oppenheimer approximation, and R_{mn} represents the constant distances between the center of mass of nuclei for a given geometry. Eigenvalue E_e is the electronic energy of the system, and $E_e - V_N$ is pure electronic energy. Besides simplifying the Schrödinger equation, the Born-Oppenheimer approximation also provides the firm idea of the shape of molecule, thus making the modeling of potential energy surfaces (PES) feasible.

1.4. Computational Chemistry:

Computational chemistry (also known as molecular modelling or atomistic simulation) is a branch chemistry that utilizes the methods of theoretical chemistry and computer simulations. It facilitates investigation of molecular shape, energies of molecules, transition states, chemical reactivity, various spectroscopic peaks, interaction between molecules, physical properties of molecules in macroscopic amounts, and many additional areas as the computational tools (i.e., supercomputing resources) become more readily available.
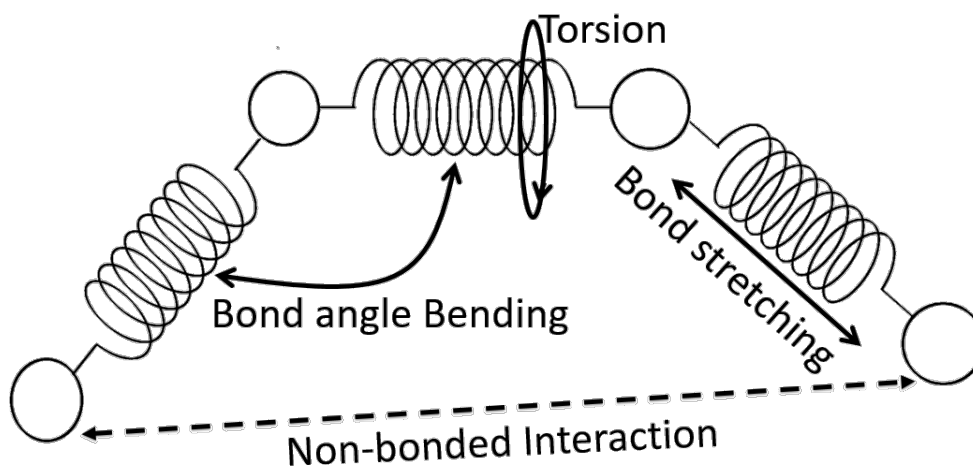
Figure 1.4: General schematic for molecular mechanics. Spheres and springs represent atoms and bonds respectively.

There are four major methods under computational chemistry: molecular mechanics (MM) and molecular dynamics (MD), ab-initio, semi-empirical, and density functional theory (DFT). In a broader sense, the MM and MD approach treats the atoms and bonds in molecules as balls (hard spheres) connected by springs, respectively, and the interactions

that exist among the balls (atoms) and springs (chemical bonds) follow classical Newtonian mechanics. Since this method does not take QM into account, electronic structure and properties cannot be evaluated with MM and MD. Among all the approaches under computational chemistry, MM is the least expensive from a computational resources perspective. In MD, physical movements of atoms and molecules are simulated by numerically solving Newton's laws of motion. The forces are generally computed with interatomic potentials, and these interatomic potentials are parameterized with models in the MM force field. The following equations are the fundamental equations underlying the MM and MD methods.

$$\vec{F}(r) = -\nabla V(r) = m\vec{a} = m\frac{d\vec{v}}{dt} = m\frac{d^2\vec{r}}{dt^2}$$

$$V(r) = V_{bond\ stretching}(r) + V_{bond\ bending}(r) + V_{torsion}(r) + V_{nonbonded}(r) + V_{cross}(r)$$

$$V_{nonbonded}(r) = V_{electrostatic}(r) + V_{van\ der\ Waals}(r)$$

MM and MD are mainly utilized to study a system comprised of a large number of atoms such as proteins and polymers, which may contain on the order of hundreds to thousands of atoms in the computational model.

In ab-initio methods, the _exact_ electronic Schrödinger equation is _approximately_ solved for the wavefunction and energy of the system. Since the electronic Schrödinger equation cannot be solved exactly for a system containing more than one electron, ab-initio

approaches use approximations. With milder approximations, the 'higher' the level of the ab-initio calculations is said to be. The simplest level of ab initio calculation is the Hartree-Fock method, where the average electron-electron repulsion effects (mean field) of electrons are considered instead of instantaneous change in the effect due to the movement of the electron. Many higher level ab-initio methods begin calculation with Hartree-Fock method, and then correct for the instantaneous change in repulsion effect. These higher level theories are called post-Hartree-Fock methods, such as Møller-Plesset perturbation theory (MPn), couple cluster theory (CC), configuration interaction (CI), etc.

In the semi-empirical method, additional levels of *approximation* are used to determine the solution of the *exact* Schrödinger equation. A major difference between the semi-empirical and ab initio methods is that in semi-empirical methods some quantities are parameterized with the help of experimental data, where as in ab-initio all quantities are calculated without using any parameters other than fundamental physical constants (hence, the name ab initio meaning from fundamentals). Semi-empirical methods are computationally less expensive than ab initio methods. Examples of some established semi-empirical methods are Hückel Method, Extended Hückel Method, Austin Model 1 (AM1), Neglect of Diatomic Overlap (NDO), Modified Neglect of Diatomic Overlap (MNDO), Parametric Method 3 (PM3), etc.

Lastly, the density function theory (DFT) method is based on two Hohenberg-Kohn theorems. Here, the *approximate* electronic Schrödinger equation is *exactly* solved for the

electron density (i.e., the wavefunction squared, instead of the wavefunction) and energy of the system. The first theorem states that the ground state properties (including energy) of a many-electron systems can be expressed as a functional of the electron density of that system. A functional is a mathematical rule that can turn a mathematical function into a number (e.g., definite integral). The second theorem states that for the value of the functional that gives the energy of a system, is minimized by the correct ground state electron density. Based on these two theorems, the Kohn-Sham equation is constructed considering a model system (also called a reference system or Kohn-Sham system) where electrons do not interact with each other. This model system contains a local effective potential (known as Kohn-Sham potential, typically denoted as $v_s(r)$) so that the electron density of the Kohn-Sham system is the same as the real target system. For this model system the Kohn-Sham equation is

$$\left[-\frac{\hbar^2}{2m_e}\nabla^2 + v_s(r)\right]\varphi_i = \varepsilon_i\varphi_i$$

Here φ_i is the Kohn-Sham orbital for i^{th} electron and ε_i is the energy eigenvalue of this orbital. The kinetic energy operator for this equation is $\widehat{T}_s = -\frac{\hbar^2}{2m_e}\nabla^2$, and the electron density is expressed as

$\rho(r) = \rho_s(r) = \sum_i |\varphi_i(r)|^2.$

Now, in DFT formalism, energy of the particle in a real system is expressed as

$$\hat{h}_i \phi_i = \varepsilon_i \phi_i$$

Here, $\hat{h}_i = -\frac{\hbar^2}{2m_e}\nabla_i^2 + V_N(r) + V_H[\rho(r)] + V_{XC}[\rho(r)]$. V_N terms represent the electron-nuclear attraction potential, V_H denotes the electron-electron coulomb repulsion as it is in the Hartree-Fock method, and the term V_{XC} is called exchange-correlation potential. V_{XC} includes all the corrections due to electronic effects according to the Pauli's exclusion principle (or the exchange effect), instantaneous changes in the repulsion potential (also known as the correlation effect), and the deviation of the T_s from the real system kinetic energy. Based on the second Hohenberg-Kohn theorem, changing ϕ_i iteratively so that its effects on V_H and V_{XC} can minimize the total energy E, make DFT self-consistent. DFT can be relatively less expensive than the higher level ab initio methods, while keeping similar level of accuracy. One of the major drawbacks of DFT methods is that, unlike ab initio methods, systematic improvement of accuracy is not yet achieved. In other words, ab initio methods are becoming more accurate as greater computational resources become available to access higher levels of theory to better describe the real system. Another problem of DFT is the inability to account accurately for van der Waals dispersion force, although this can be remedied with inclusion additive terms or using improved functional form[22–25]. Nonetheless, DFT methods are used widely in many applications from electronic structure to reaction pathway analysis to successfully reproduce experimental data trends, provide novel microscropic insights, and serve as a virtual screening tool to reduce experimental costs.[26,27]

1.5. Computational Chemistry to Investigate Enzymatic catalysis and Electrocatalysis:

1.5.1. Tools for Computational Study of Reactions Catalyzed by Enzymes

There are multiple computational methods have been employed over the last decades. (Fig. 1.5). Except for the reactive forcefield method, all are based on QM methodologies.
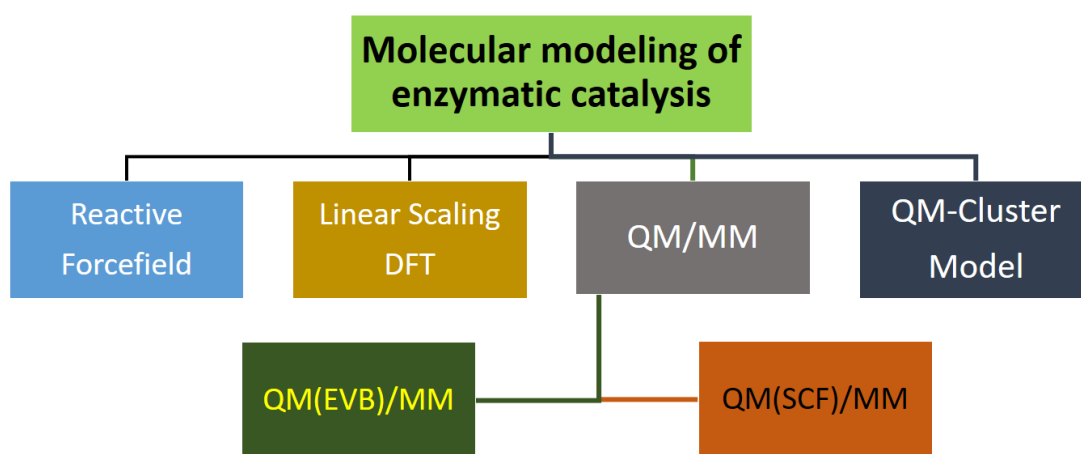
Figure 1.5: Molecular modeling methodologies to study enzymatic catalysis.

The reactive forcefield methods use classical theory with embedded parameterized terms allowing chemical reactivity. Such forcefields include ReaxFF, MMPT (Molecular Mechanics with Proton Transfer), ARMD (Adiabatic Reactive Molecular Dynamics), etc.

Among the molecular modeling methodologies employing QM, linear scaling DFT (a.k.a. large-scale DFT) is a relatively new approach. Whereas applying conventional DFT (and other QM approaches) for a large system is unfavorable resource-wise, the development of

linear-scaling DFT allows to circumvent such computational bottlenecks.[28] This method is already applied successfully to study enzymatic systems, and also holds a lot of potential for future applications.[29,30]

The hybrid QM/MM method and the QM cluster method are the two most commonly used computational chemistry tools to study enzymatic catalysis. In both cases, QM methodologies range from ab initio techniques to DFT to various semi-empirical schemes. In the hybrid QM/MM scheme, QM methods are employed to study the relatively smaller chemically reactive part of the system (substrate, active site, and necessary residues), while the remaining large portion of the system (surrounding protein and solvents) are modeled with MM. On broad stroke the hybrid QM/MM can be classified into two farther methodology, QM(EVB)/MM and QM(SCF)/MM. In empirical valence bond (EVB) method QM part is modeled with a two-diabatic-state using Marcus parabola based on valence bond theory. It should be mentioned that application-wise QM(EVB)/MM is more similar to the reactive force field methods.[31–34] In our study of biocatalyst, this method was initially used.

In the QM(SCF)/MM, QM part is treated with conventional first principle based methodologies. The overall general scheme in this methodology to generate potential energy surface can be expressed with following equations.

$$E = E_1^{QM} + E_{1,2}^{MM} - E_1^{MM}$$

Here E_1^{QM} is the energy of the QM calculated energy of the QM system (subsystem 1), E_1^{MM} is the MM energy of the same subsystem, $E_{1,2}^{MM}$ is the MM energy of the total system

(subsystem 1 and larger subsystem 2). In another approaches, the following additive method is used

$$E = E_1^{QM} + E_2^{MM} + E^{QM/MM}$$

$E^{QM/MM}$ represents the interaction energy between QM treated subsystem 1 and MM treated subsystem 2. Three approaches have been widely used to express these interactions between QM and MM parts: (i) electrostatic, (ii) mechanical, and (iii) polarizable embedding.

A significant issue in all QM/MM models is the treatment of the covalent bonds across the QM-MM boundary. Multiple schemes have been employed to address this issue (e.g., boundary schemes, link atom schemes, boundary atom schemes, and localized orbital schemes.)

The method used to study enzymatic catalysis in this dissertation is the QM-cluster (also known as 'QM-only').35 Instead of treating the whole enzymatic system, this model treats only the part of the system that is quantum-mechanically significant; which usually consists of the active site and the surrounding residues relevant for the course of enzymatic catalysis. A QM-cluster model is generally built from an existing structure from a protein databank. It should be mentioned that the resolution of the structure can play a critical role in the QM-cluster method; for accurate results, better resolution (<2Å) is necessary. Thus, selecting the truncated system is one of the most significant issues in cluster modeling.

The selection of the truncated system from the enzyme plays a crucial role in QM-cluster modeling, since the system contains only limited number of atoms compared to the total enzyme. For accurate result the truncated system should contains all atoms participating in the reaction, as well as ll residues responsible for binding and stabilizing substrate and maintaining necessary configurations with short and long-range non-covalent interactions.

Due to the absence of a sizable part of the enzyme in a QM-cluster model, addressing the steric and polarization effects of the complete systems can be a significant issue. The conventional strategy to model the electrostatic influence of the protein environment is by assuming a homogeneous polarizable medium using a dielectric constant. Although the continuum solvation model brings many advantages toward an accurate description of solvation effects, the choice of dielectric constant seems arbitrary. However, it has been pointed out that as larger models are employed, the choice of dielectric constant becomes increasingly less important.[35]

1.5.2. Computational Tools for Electrocatalytic Reaction Study:

First-principles-based quantum mechanical calculations have allowed elucidation of reaction mechanisms for various heterogeneous catalysis processes, but for electrocatalytic reactions, it has a significant drawback. Conventional QM calculations (mainly DFT) can be used to investigate the thermodynamics of electrochemical reactions but are not very suitable for kinetic study. Moreover, allowing an electrochemical double layer into QM models to elucidate the structures and interactions of the electrolyte over the electrode is very challenging. Several DFT modeling approaches have been developed and can be found in literature to study electrocatalytic reactions (Fig. 1.6).
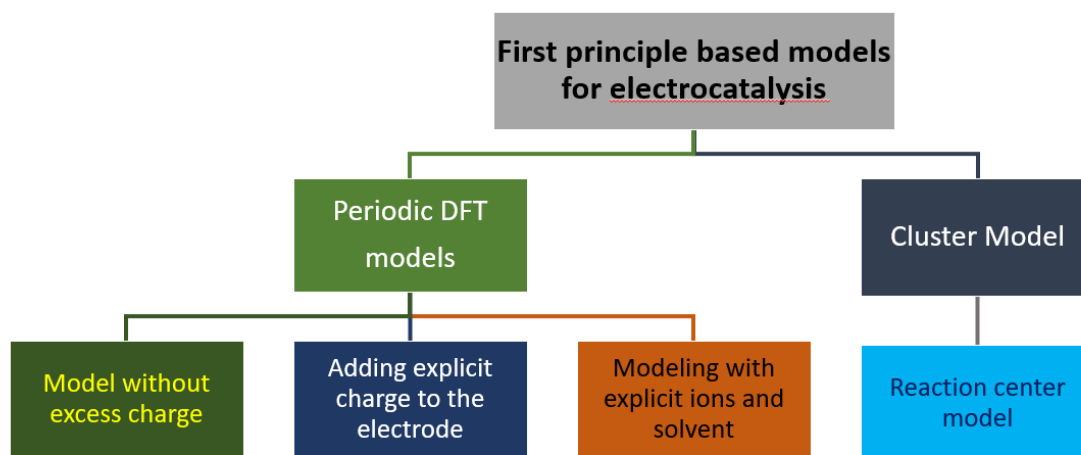
Figure 1.6: Various QM based computational chemistry methods to study electrocatalytic system.

DFT methods can be differentiated by cluster and periodic representation of the electrode surface. The ''reaction center'' model, is an early attempt to evaluate potential dependent reaction energies and activation barriers. It relies on using a small cluster to represent the ''reaction center'' of the electrode and evaluates the electron affinity of such cluster. Its

fidelity is questionable given its arbitrarily small representation of the electrode when considering its electronic structure and lack of scalability to a more accurate electrode representation.

The remaining models to be discussed typically use a periodic representation of the electrode surface, allowing for accurate consideration of the electronic structure of the extended solid. All of the methods take advantage of thermochemical relationships to represent the chemical potential of electrons, ions, or electron–ion pairs. This method employed the linear free energy relationship and applied a computational reference electrode to perform reaction energy calculations. Because this approach allows the direct use of standard DFT calculations for heterogeneous catalysis, it has been widely used in electrocatalytic systems to predict the reactivity of metal or alloy catalysts. As discussed above, it is not possible to take into account the dynamic electrolyte structure within a DFT model, and therefore all of the methods surveyed represent an approximation to the actual system.

2. Reaction Pathway Analysis of Serine Protease with QM Cluster Study

2.1. Introduction to Enzymatic Catalysis:

Enzymatic catalysis is one of the key factors underlying the existence of life. Virtually all metabolic reactions essential for life, cannot occur without an enzyme. Besides sustenance of life, enzymes have been used by mankind from prehistoric time, e.g., for the fermentation of cereal products to form alcoholic beverages around 3000 BC.[36] The current global enzyme market has been estimated to be around eight billion dollars with increasing market demand (Figure 2.1)[37].

U.S. enzymes market size, by product, 2014 - 2025 (USD Billion)

Source: www.grandviewresearch.com
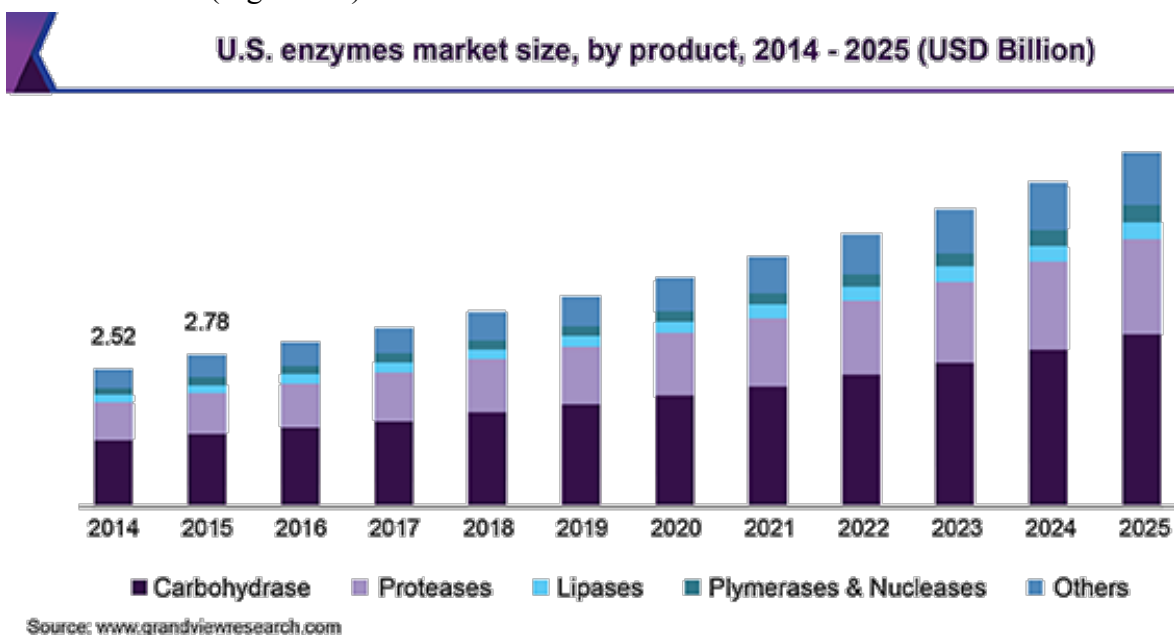
Figure 2.1: Enzyme market estimation with future projection in USA (with the permission of GrandViewResearch Inc.)

In addition to the financial perspective, enzymes have become a major interest among scientific researchers for a greener and sustainable future. Compared to traditional heterogeneous catalysts, enzyme (or biocatalysts) can ensure higher selectivity, lower

toxicity, and the ability to function under milder conditions (pressure and temperature) thus increasing process safety[12].

Enzymes are globular proteins, each of which acts as a catalyst for a particular type of biochemical reaction. Currently around 5,000 reactions are known to be catalyzed by enzymes[38]. In these catalytic processes, a reactant or substrate is bound to a specific site of enzyme, which called the active site. Substrate binding to the active site can occur multiple ways, such as covalent bonding, hydrogen bonding, van der Waals interactions, or electrostatic interactions. Some enzymes need an additional organic or inorganic chemical substance (known as the cofactor) to carry out the full catalytic function. Based on the reaction that is catalyzed enzymes are classified into six major different classes (with additional subclasses)[39].

1. Oxyreductases: This class of enzymes catalyzes redox reactions. An example of this is alcohol dehydrogenase enzyme, that facilitate the reaction below

   1.1. $CH_3CH_2OH + NAD^+ \xrightarrow{\text{alcohol dehydrogenase}} CH_3CHO + NADH + H^+$
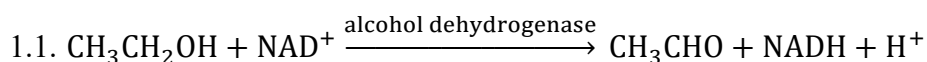
2. Transferases: Transferase enzymes work as a catalyst in the reaction where a functional group is transferred from one molecule to other. For example, phosphotransferase catalyzes the reaction below

   2.1. $R' - PO_4^{2-} + R - OH \xrightarrow{\text{phosphotransferase}} R - PO_4^{2-} + R' - OH$
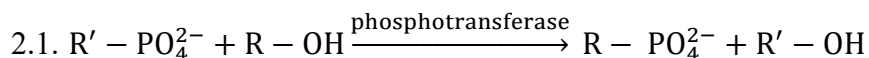
3. Hydrolase: Hydrolase enzymes catalyze various types of bond cleaving through hydrolysis. The overall reaction for the hydrolase enzyme is generally described as

$$A - B + H - OH \xrightarrow{hydrolase} A - H + B - OH$$
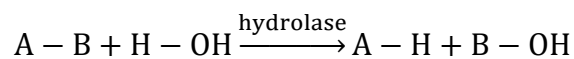
There are thirteen subclasses under the hydrolase class based on the type of bonds the hydrolase facilitates to cleave. These thirteen subclasses are as follows

3.1. Hydrolases acting on ester bonds

3.2. Glycosidases, or hydrolases acting on glycoside bonds

3.3. Hydrolases acting on ether bonds

3.4. Protease, or hydrolases acting on peptide bonds (i.e., amide bonds)

3.5. Hydrolases acting on carbon-nitrogen bond other than the peptide bonds (i.e., amide bonds)

3.6. Hydrolases acting on acid anhydrides

3.7. Hydrolases acting on carbon-carbon bonds

3.8. Hydrolases acting on halide bonds

3.9. Hydrolases acting on phosphorous-nitrogen bonds

3.10. Hydrolases acting on sulfur-nitrogen bonds

3.11. Hydrolases acting on carbon-phosphorous bonds

3.12. Hydrolases acting on sulfur-sulfur bonds

3.13. Hydrolases acting on carbon-sulfur bonds

2254.2 (27.54%)
454 (5.55%)
430.8 (5.26%)
1133.4 (13.85%)
3911.8 (47.8%)

Amounts in Million USD

Carbohydrase
Protease
Lipases
Polymerases &Nucleases
Others
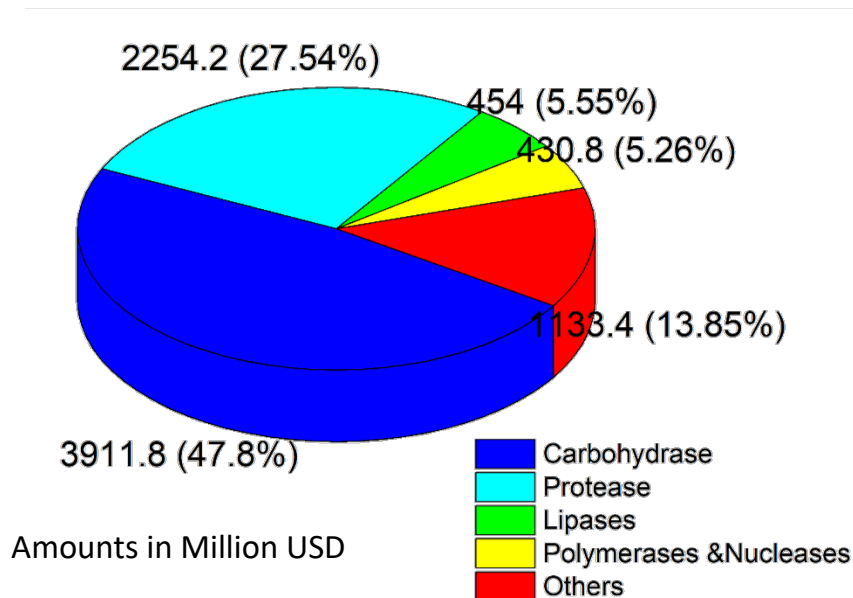
Figure 2.2: Market share of different types of enzyme. Carbohydrase, protease, and lipase all fall under the hydrolase class. (GrandViewResearch Inc.)

Hydrolases have the largest (more than 80%) share on the current enzyme market (Figure 2.2)[40]. In this document the hydrolase enzymes are one of the main focus of research interest. The study has been carried out with serine proteases.

4. Lysase: This type of enzyme catalyzes the removal of a functional group from the substrate molecule. An example of lysases is deaminase.

$$R - CH_2 - CH(NH_2) - R' \xrightarrow{\text{deaminase}} R - CH_2 = CH - R' + NH_3$$
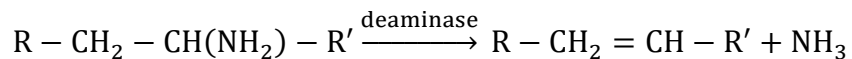
5. Isomerases: Isomerase enzymes function as catalysts by converting one isomer to another. An example of isomerases is racemases that catalyze the inversion of stereochemistry in biological molecules. Racemases catalyze the stereochemical inversion around the asymmetric carbon atom in a substrate having only one center of asymmetry.
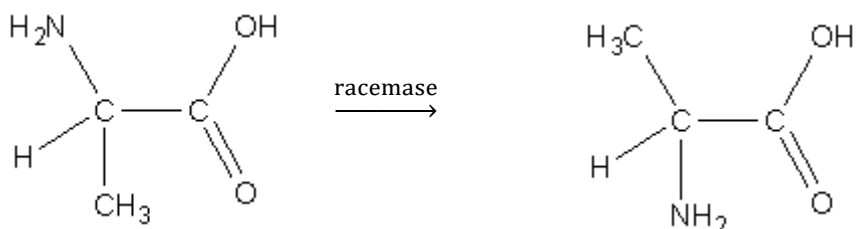
6. Ligase: This class of enzyme catalyzes reactions leading to the joining of two molecules usually accompanying a bond breaking in some other molecule.

$$CH_3C - CO - COO^- + H_2CO_3 + ATP \xrightarrow{\text{pyruvate carboxylase}} HOOC - CO - COO^-$$
$$+ ADP + P$$
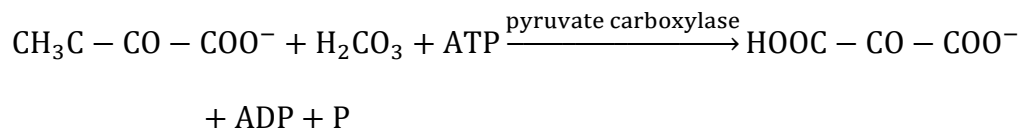
Reaction mechanisms involved in enzyme catalysis can vary from one enzyme to another. In enzymes the catalytic processes occur in a relatively small active sites where the substrate molecules bind and undergo the relevant reactions. The main principle is lowering the overall activation energy barrier (E_a or $\Delta g^{\ddagger}$). The catalytic power, or proficiency (KP), of an enzyme can be expressed as

$$KP = \frac{\text{rate coefficient with enzyme}, k_c}{\text{rate coefficient of uncatalyzed reaction}, k}$$

Using the Eyring equation, we can express KP as the equation below

$$KP = \frac{\frac{k_B T}{h} e^{-\frac{\Delta g_c^\ddagger}{RT}}}{\frac{k_B T}{h} e^{-\frac{\Delta g^\ddagger}{RT}}} = e^{\frac{\Delta g^\ddagger - \Delta g_c^\ddagger}{RT}} = e^{\frac{\Delta H^\ddagger - \Delta H_c^\ddagger}{RT}} \times e^{\frac{\Delta S_c^\ddagger - \Delta S^\ddagger}{R}}$$

Here, k_B, R, and h denotes Boltzmann constant, universal gas constant, and Planck's constant, respectively. H, S, and g represent the enthalpy, entropy, and Gibbs free energy, respectively. The superscript '$\ddagger$' denotes the thermodynamic property is an activation to form a transition state, the subscript 'c' represent the catalytic process, and the 'Δ' denotes the difference of the thermodynamic properties between transition state and the reactant(s). The enthalpic terms in the equation represent the ability of the enzyme to stabilize a highly strained transition (or high energy transition state)[41], and the entropic term represents the ability of the enzyme to increase the probability of collision to form transition state[42]. In the case of certain enzymes, instead of decreasing the activation barrier of transition state, the enzyme decreases the energy of near attack conformation of substrates, thus decreasing overall barrier[43].

One of the aspects in the mechanism of enzyme catalysis is the conformational changes (or allosteric transition) of enzyme[44]. Despite the fact that allosteric transition or conformational coordinate is a relatively slow process (in the range of microseconds to milliseconds) compared to the reaction phenomena or chemical coordinate (femto seconds to nanoseconds)[45,46], the allosteric transition can play a major role in catalysis through two mechanisms. Firstly, there is the select-fit model, which states that only certain conformation(s) of enzyme allow substrates to bind[47]; whereas, the second model known

as induced-fit model allows the initial substrate binding itself to cause the allosteric changes in enzyme[48].

Several organisms and micro-organisms have been considered, from an anthropocentric point of view, to successfully thrive in extreme environmental conditions due to a diverse array of adaptive strategies spanning from structural to physiologic adjustments[49,50]. Temperature is one of the most important environmental factors for life and the clarification of adaptation mechanisms at different temperature conditions are of crucial relevance for both fundamental research[51–53] and industrial applications aimed at developing new biocatalysts, active in different temperature ranges [54]. On the two opposite sides of the scale of temperature adaptation, psychrophilic and thermophilic micro-organisms have to cope with extremely low or high temperature environments, respectively. Among the available adaptive strategies, these micro-organisms have evolved their enzymatic repertory through natural selection to be able to survive and reproduce successfully. It has been suggested that the optimization of enzyme function at a given temperature requires a proper balance between a sufficient structural rigidity for the maintenance of the enzyme three-dimensional (3D) architecture and flexibility for the ''breathing'' of critical protein functional regions to incorporate water or allow limited structural reorganization of amino acid side chains[55,56]. However, the molecular determinants and the relationships between catalytic activity, thermal stability, and flexibility in psychrophilic enzymes are still a matter of debate.

Ionizable residues in proteins play major roles in almost all biological processes, including enzymatic reactions, proton pumps, and protein stability. Understanding these roles can

41

require evaluating both the interactions of the ionized groups and the energetics of the ionization process itself. Thus, an ability to calculate pK$_a$ of ionizable groups in proteins can be crucial for structure–function correlations as well as for validating different treatments of electrostatic energies[57]. Extremely high or low pH values generally result in complete loss of activity for most enzymes. pH value is also a factor in the stability of enzymes. As with activity, for each enzyme, there is also a region of pH values for optimum stability. The optimum pH value will vary greatly from one enzyme to another, and, for native alkaline proteases of both bacterial and fungal origin, this optimum pH value range can be as wide as 8.0 to 13.0[58]. In addition to temperature and pH values, there are other factors, such as presence of other soluble molecules or properties of solvent, which can affect the enzymatic reaction efficacy.[59–61] Each of these physical and chemical environmental variables must be considered and optimized in order for an enzymatic reaction to be accurate and reproducible.

2.1.1. Introduction to Serine Proteases:

As previously mentioned, the preliminary results for modeling enzymatic catalysis that are presented herein were carried out on the serine protease. The largest known category in the protease enzyme subclass with more than one third of all proteases is the serine protease category[62,63]. Due to its ubiquitous presence in nature (all known organisms), evolution allowed serine proteases active under diverse conditions with temperature ranges from 4ºC to 65ºC[64,65].

More than ninety percent share of current global protease market is held by serine protease based products[66–68]. The application sectors span household detergent products, leather processing industry, food industry, waste management, biomedical applications, among many others[66]. Almost all US Food and Drug Administration (FDA) approved proteases in biomedical applications are serine proteases[69].
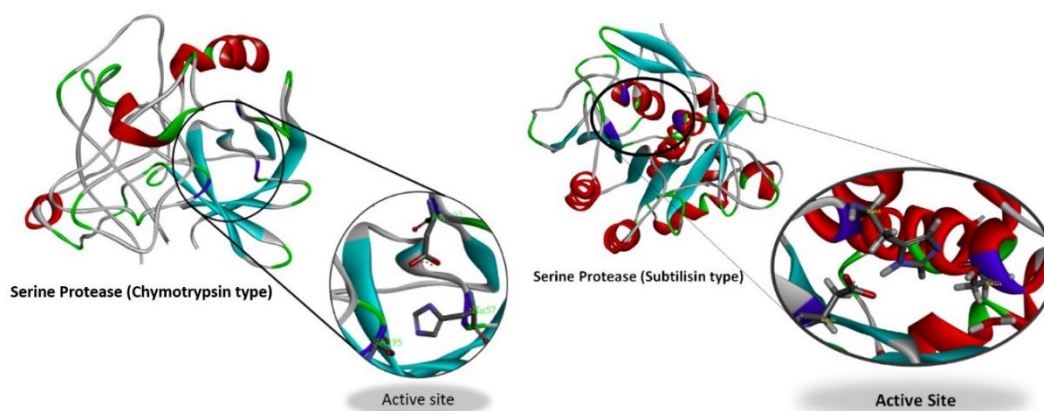
Figure 2.3: Structures of chymotrypsin-like (left image) and subtilisin-like (right image) serine proteases with the active sites highlighted. The red color represents alpha helices and cyan represents beta sheets in each enzyme crystal structure

Structurally serine proteases can be categorized broadly into two types: chymotrypsin-like and subtilisin-like[70] (Figure 2.3). Chymotrypsin-like serine proteases have a dominant double beta-barrel sheet present in its structure. The structure of subtilisin-like serine proteases consists of several alpha-helices and a large beta-sheet. In spite of the structural differences, the active site of all serine proteases is conserved and contains the same catalytic triad of amino acids with a charge relay network. This catalytic triad is comprised of an aspartate (Asp), a histidine (His), and a serine (Ser) amino acid[62,71–73]. All serine enzymes perform covalent catalysis using this catalytic triad. The serine amino acid of the

triad acts as the nucleophile attacking the targeted scissile peptide bond, thus the critical role of this amino acid during catalysis gives the serine protease its namesake.

In the generally accepted reaction pathway of serine proteases[71] (Figure 2.4), the first step is histidine acting as a general base and the proton receptor from serine hydroxyl group, leaving serine as a net negatively charged nucleophile. This nucleophilic serine then attacks the carbonyl of the scissile peptide bond, thus forming the first tetrahedral intermediate. In the subsequent step nitrogen breaks away from the peptide bond by taking the proton from His-H$^+$ (which acts as an acid) to yield the acylenzyme intermediate. The acylenzyme intermediate is characterized by the acyl moiety of the substrate being transiently attached to a serine hydroxy group of the protease. This step is known as His-flip (or ring-flip), and all amino acids and intermediates become net neutral charged in the active site.
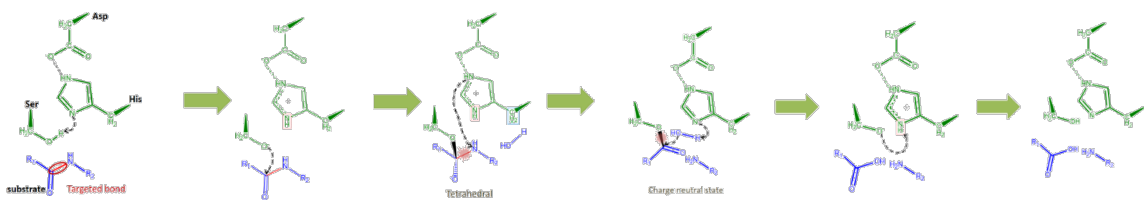
Figure 2.4:   Reaction pathway of the serine protease according to literature.

In the next step, the water molecule is then deprotonoted by the histidine, attacks the carbonyl of the acylenzyme moiety on the substrate side, and forms a second tetrahedral intermediate. This second tetrahedral intermediate immediately collapses by breaking a nearby bond to form a negatively charged serine on the enzyme side and the product carboxylic acid functionality on the substrate side. In the final step, the net negatively

charged serine takes the proton away from His-H+, and thus restoring the enzyme. The role

of aspartate, which is net negatively charged, is to stabilize the protonated histidine (net

$$E+S \underset{}{\overset{1}{\rightleftharpoons}} ES \underset{}{\overset{2}{\rightleftharpoons}} ES^* \underset{}{\overset{3}{\rightleftharpoons}} ES' \overset{4}{\longrightarrow} EA \overset{H_2O}{\underset{5}{\longrightarrow}} EP \overset{6}{\longrightarrow} E' \overset{7}{\longrightarrow} E$$

$$P_1 \qquad\qquad P_2$$
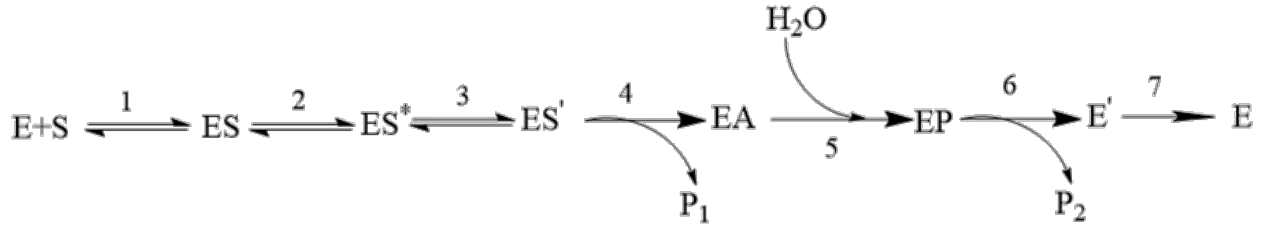
positively charged) by forming hydrogen bond supported by additional strong nonbonded

electrostatic interactions. The tetrahedral intermediate is stabilized by the presence of an

oxyanion hole. The reaction mechanism analysis for the established pathway is given

below:

For this pathway reaction kinetics can be shown with following equations:

$$V_{P_1} = k_4[ES'] = \frac{k_1 k_2 k_3 k_4}{k_{-1}k_{-2}k_{-3} + k_{-1}k_{-2}k_4 + k_{-1}k_3 k_4 + k_2 k_3 k_4}[E][S] = V_{P_2} = V$$

$$[E_T] = \Big\{ 1 + \frac{k_1}{k_{-1}k_{-2}k_{-3} + k_{-1}k_{-2}k_4 + k_{-1}k_3 k_4 + k_2 k_3 k_4}\Big(k_{-2}k_{-3} + k_{-2}k_4 + k_3 k_4$$

$$+ k_2 k_{-3} + k_2 k_4 + k_2 k_3 + \frac{k_2 k_3 k_4}{k_5[H_2 O]} + \frac{k_2 k_3 k_4}{k_6} + \frac{k_2 k_3 k_4}{k_7} \Big)[S] \Big\}[E]$$

With this kinetic equations takes the form of Michaelis-Menten equation:

$$\frac{V}{E_T} = \frac{k_{cat}[S]}{1 + K_M[S]}$$

Where catalytic rate constant, $k_{cat} = \frac{k_1 k_2 k_3 k_4}{k_{-1}k_{-2}k_{-3} + k_{-1}k_{-2}k_4 + k_{-1}k_3 k_4 + k_2 k_3 k_4}$,

and Michaelis constant, $K_M = \dfrac{k_1}{k_{-1}k_{-2}k_{-3}+k_{-1}k_{-2}k_4+k_{-1}k_3k_4+k_2k_3k_4}\left(k_{-2}k_{-3} + k_{-2}k_4 + k_3k_4 + k_2k_{-3} + k_2k_4 + k_2k_3 + \dfrac{k_2k_3k_4}{k_5[H_2O]} + \dfrac{k_2k_3k_4}{k_6} + \dfrac{k_2k_3k_4}{k_7}\right)$

Despite being the established, some serious issues have been raised about the details of this pathway[62,74–77], especially about the His-flip step[78]. For nitrogen to take the proton from the imidazole ring of histidine, the ring needs to flip, thus the name (Figure 2.5). For this flipping to occur, three hydrogen bonds need to be broken, which requires a significant
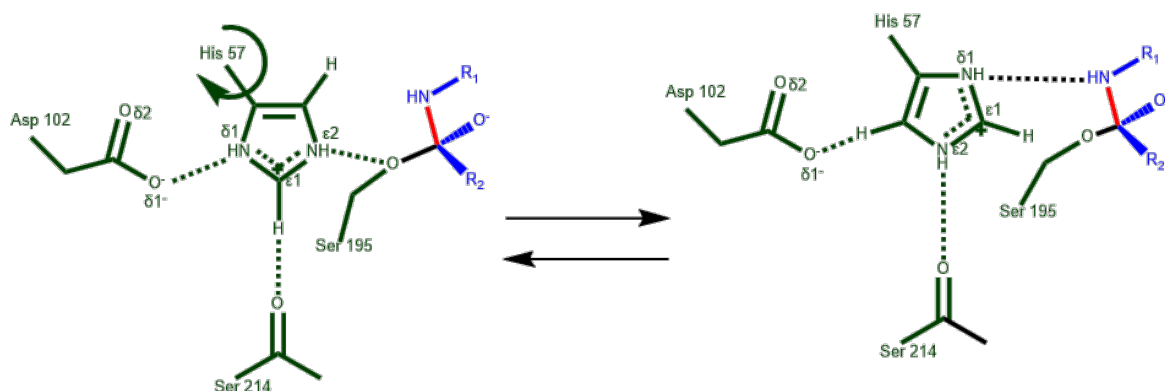
Figure 2.5: The 'His-flip' mechanism. Enzyme, substrate, and the scissile bond is represented with green, blue and red color respectively

amount of energy[79,80]. Moreover, there is a significant steric barrier also present for imidazole ring to donate proton to the nitrogen atom.

To probe the complications around the reaction mechanism, atomistic modeling and simulation are powerful tools to test and validate hypotheses. Although many computational studies have been carried out on serine proteases, only a very few computational studies calculating the thermochemical and kinetic properties have been performed for the full reaction pathway(s) [75–77,81].

In our study herein, another alternative yet potentially competitive reaction pathway is hypothesized for serine protease catalysis.
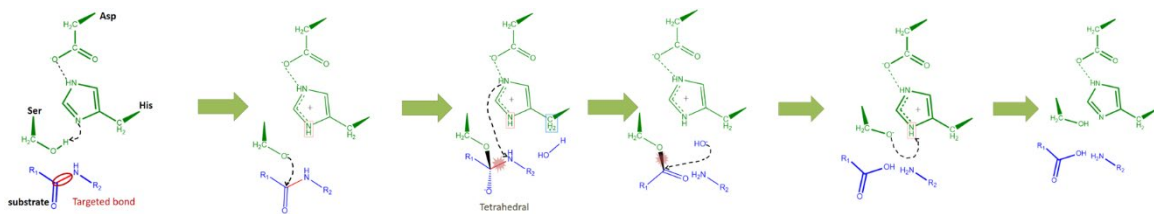
Figure 2.6: Proposed alternative reaction pathway of the serine protease.

This proposed pathway differs from the established one in the third step (His-flip), that is, instead of a net positively charged imidazole ring, a reactant water is considered for the donation of the proton to the scissile nitrogen atom (Figure 2.6). Histidine remains protonated, and thus, in all intermediate steps of our proposed mechanism, the net charge separation remains between ionized amino acids. Our proposed reaction mechanism is consistent with 'proton shuttling' mechanisms which are common in solvents, such as water, with relatively high dielectric constants.[82]

Construction of thermochemical and kinetic profiles for both the established and proposed reaction mechanisms with atomistic modeling tools is ongoing. The preliminary results presented herein are from QM cluster calculations employing DFT methodology. The DFT cluster calculated used a truncated active site model comprised of a peptide substrate, reactant water molecule, and only the histidine and serine amino acids of the catalytic triad of the protease. Here, the peptide employed is arbitrary, and other amino acid pairs or polypeptides undergo a similar reaction pathway and could have been used. The

comparative profiles based on this QM cluster data show that the alternative pathway is competitive in terms of the overall apparent activation barrier with the established pathway.

From the current available literature, the value of expected activation free energy barriers ranges from 18 to 25 kcal mol^{-1} (depending upon both the substrate and the enzyme), and shape of the reaction energy profile according to the established mechanism appears to have a deep potential energy well immediately after the his-flip step, where all amino acids and intermediate states in the active site are net charge neutral (Figure 2.4).

The preliminary results from our study for the established reaction mechanism are in accordance with the expected reaction profile shape. The shape of the free energy profile for the proposed reaction mechanism constructed from the preliminary QM cluster calculations does not have any potential energy well, but it does have the same overall apparent activation barrier height as the established pathway. The value of the overall apparent activation barrier height for both reaction mechanisms is found to be relatively high and over predicted with our QM cluster calculation. Due to the nature of the truncated active site model used in the QM cluster calculations, the overall apparent activation barrier height is expected to significantly decrease with the simulation of the full enzyme system.

2.2. Method:

All the calculations performed in this study were based on the structure of bovine trypsin (which is a chymotrypsin type serine protease) with PDB entry number 4XOJ.

In this work we chose to study the catalytic mechanism of the enzyme with a quantum mechanical calculation based cluster model that contains all the amino acid residues that

are directly involved in the catalytic process, as well as all neighboring amino acids that are important to maintain the active site topology. QM cluster method is chosen instead of the others since it facilitates a higher and more accurate theoretical level and free TS determination (not just a free energy surface or profile of reduced dimensionality). It should be mentioned that two points are commonly raised about the disadvantages of the QM cluster model. One is the replacement of the long-range interactions by a dielectric continuum and the fact that the small size of the model might not capture medium and large-scale conformational rearrangements.

In the model built to study the present enzymatic system these problems do not seem to be relevant. To address the first disadvantages, all the residues of the enzyme that participate directly or indirectly in the reaction were included explicitly in the cluster model. All the residues that establish hydrogen bonds, or other electrostatic interactions with the reacting atoms were also included. Finally, the contribution of the dielectric continuum is quite small (less than 4 kcal mol), which means that medium/long range interactions beyond the model are not expected to be very relevant, and that the inclusion of the dielectric continuum is a good approach to account for the medium/long-range interactions. This is also reflected by the free energies that were calculated for the rate limiting step of the full catalytic process, which agree very well with the available experimental data.

Considering second problem, we can say that the network of hydrogen bonds gives origin to a robust model, where minimal geometry restrictions (i.e. frozen atoms) were introduced. Indeed, only backbones of the four amino acids were frozen during the geometry optimizations, which allows for significant conformational rearrangements

within the active site region, if they are to take place. The active site is quite rigid, due to an extensive network of hydrogen bonds.

The cluster model used to study the catalytic mechanism contains a total of 191 atoms (57 C, 96 H, 17 N and 21 O atoms) and consists of substrate Ala-Phe-Arg-Ala peptide, Ala56, His57, Asp102, Gly193, Asp194, Ser195, Gly196, Gly 197, Ser 214 and, a water molecule. The terminal amino acid residues were capped with methyl groups.

The cluster model was then subjected to geometry optimizations. In this process, the carbon from the methyl groups was constrained to keep the geometry of the cluster model close to what is observed in the X-ray structure. All geometry optimizations were performed with Gaussian 16 applying the density functional theory with an empirical dispersion correction.[83,84] BLYP functional as implemented in Gaussian 16 and the 6-311+G** basis set.[85,86] To provide an improved description of the nonlocal nature of the electron correlation, in particular hydrogen bonds and van der Waals interactions, the Grimme dispersion with the original D3 damping function was used. Implicit solvation using a self-consistent reaction field (SCRF) with the Conductor-like Polarizable Continuum Model (CPCM) was employed with the dielectric constant of water (ε=78).[87,88] Fahmi Himo et al demonstrated that as cluster size get larger (more than 100 atoms), the variations of dielectric constant (ε) have very small effect (less than 1kcal.mol^{-1}) on reaction energetics.[35]

In all geometry optimizations, the search for the transition state starting from a structure similar to the reactant model. This was generally obtained with unidimensional scans along the particular reaction coordinate in which we were interested. Once a putative transition structure was located, and thus was fully optimized (except for the frozen atoms), the reactants and the products associated with it were determined after intrinsic reaction coordinate (IRC) calculations. In all cases, the geometry optimizations and the stationary points were obtained with standard Gaussian convergence criteria. The transition state structures were all verified by vibrational frequency calculations. The ZPE and thermal and entropic energy corrections were calculated using the same method and basis.

Final values of all the activation and reaction free energy differences with be calculated at the B3LYP/6-311++G** level detailed above, while the atomic charge distributions will be calculated employing a Mulliken population analysis, using the same level of theory. Overall this methodology is well-established and has been used in a large number of research studies.

2.3. Results and Discussion:

The calculated Gibbs free energy values using the QM cluster for all reaction intermediates and transition states for the currently established pathway (Figure) and the proposed pathway (Figure 2.7) are depicted in Figure 2.7 and listed in Table 2.1, respectively.
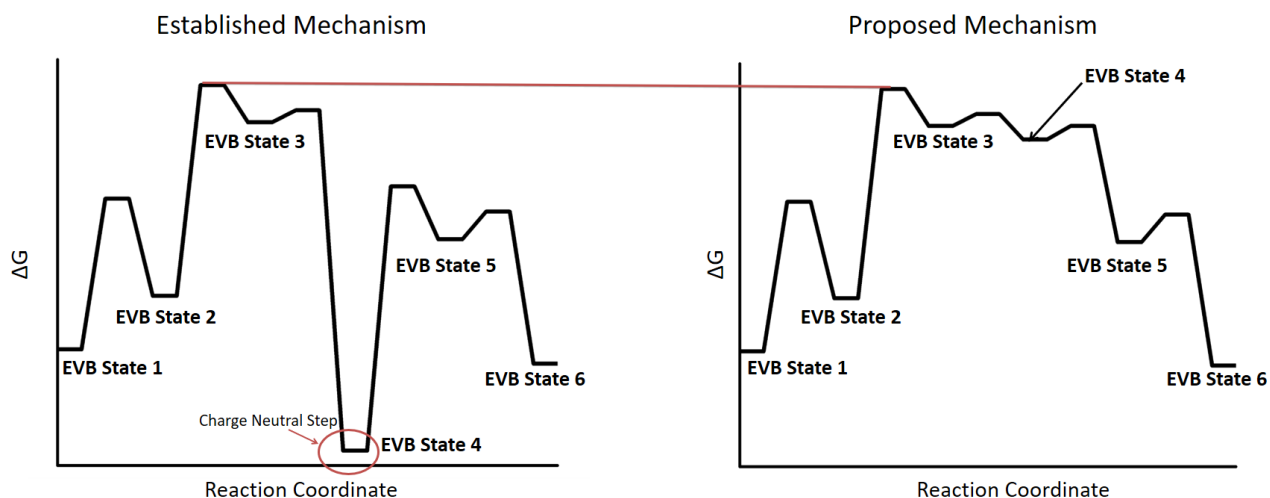
Figure 2.7: The Gibbs free energy (ΔG) diagram for the His-flip and the proposed pathways (Based on data from Table 2.1).

The very high value of the activation barrier (45.6 kcal mol^{-1}) is common to both pathways, and the overprediction from the QM cluster calculations is likely due to the absence of hydrogen bonds from the oxyanion hole. It should also be noted that DFT methods are historically known to overpredict activation barriers on average for a variety of reacting systems both in the gas and condensed phases.[89,90]

Table 2.1: The Gibbs free energy (ΔG) values of all states (reactants, reaction intermediates, transition states, and products) along the both established and proposed pathway

Currently accepted Pathway		Proposed Pathway	
State	ΔG in kcal mol^{-1}	State	ΔG in kcal mol^{-1}
Intermediate state 1 (Reactant)	0	Intermediate state 1 (Reactant)	0
Transition State 1	26.02	Transition State 1	26.02
Intermediate state 2	9.25	Intermediate state 2	9.25
Transition State 2	45.60	Transition State 2	45.60
Intermediate state 3 (Tetrahedral Formation)	39.19	Intermediate state 3 (Tetrahedral Formation)	39.19
Transition State 3	41.27	Transition State 3	41.27
Intermediate state 4 (No charge separation)	-17.45	Intermediate state 4	36.83
Transition State 4	28.10	Transition State 4	39.19
Intermediate state 5 (Product 2)	19.01	Intermediate state 5 (Product 2)	19.01
Transition State 5	23.78	Transition State 5	23.78
State 6 (Enzyme Recovery)	-2.46	State 6 (Enzyme Recovery)	-2.46

Previously, selected reaction pathway analysis calculations were performed with the BLYP functional and DNP numerical basis set with a smaller cluster model of the active site. The calculated results showed a similar relative ranking of key intermediates between His-flip and proposed pathways.

Thus, these results are convincing enough to suggest the viability of the proposed pathway. Moreover, the overall shape of the Gibbs' free energy surface of reaction is similar to previous studies in the literature, which suggests that our level of theory is sufficient enough to capture the relative ranking of energetics for the significant bond breaking and formation steps.[91]

Once the calculations provide the $\Delta g^{\ddagger}$ values in the acceptable ranges (≤ 26 kcal·mol^{-1}), the rate coefficients for all steps in both pathways can be determined. It should be mentioned that no experimental values are available for individual step rate coefficients. Instead, the overall Michaelis-Menten parameters (k_{cat} and K_M) are determined through experiments.

From the computationally determined rate coefficients for both pathways Michaelis-Menten parameters can be calculated and compared with the literature values.

These comparative studies of two pathways can give us a better insight into the reaction mechanism, allowing enhancements in applicability with chemical engineering insights (e.g., to model better inhibitors or mutating for targeted environmental conditions).[92]

2.4. Conclusion:

In this study, the reaction energetics of the peptide hydrolysis with serine protease has been carried out to shed light on novel insights. A new pathway has been proposed to resolve the long standing debates about the currently accepted His-flip pathway.

QM cluster with the DFT studies has been carried out for both pathways for an unbiased hypothesis test. Although it is a work in progress, the results so far indicate the viability of the proposed pathway. The presence of deep minima in the His-flip mechanism indicates an impediment for reaction to complete, whereas no such barrier is observed in the proposed mechanism. Moreover, in the proposed mechanism, the charge separation is maintained through all intermediates. In contrast, in His-flip mechanism charge separation is collapsed to the charge neutral state right after histidine flip occurs, but again separated in the next step, which considering other enzymes in literature seems highly unlikely.

Since the divergent point of these two pathway started with formation products, the clear insight is necessary to farther improve or rational modification for potential application. This study can help in this venture.

3. Electrocatalytic performance of MoTe$_2$/graphene Nanocomposite for Hydrogen Evolution Reaction

3.1. Introduction:

In the modern world, the utilization of hydrogen is playing one of the crucial roles with application in many essential industries and fields (e.g. NH$_3$ production with Haber-Bosch process, refining a wide range of petrochemicals, methanol production, fuel cell technology, aerospace technology, cryogenics, and many others.) The global demand of hydrogen in 2019 has been estimated around 120 billion dollars[93] with an increasing trend over time (Figure 3.1).

U.S. hydrogen generation market size, by technology, 2014 - 2025 (USD Billion)
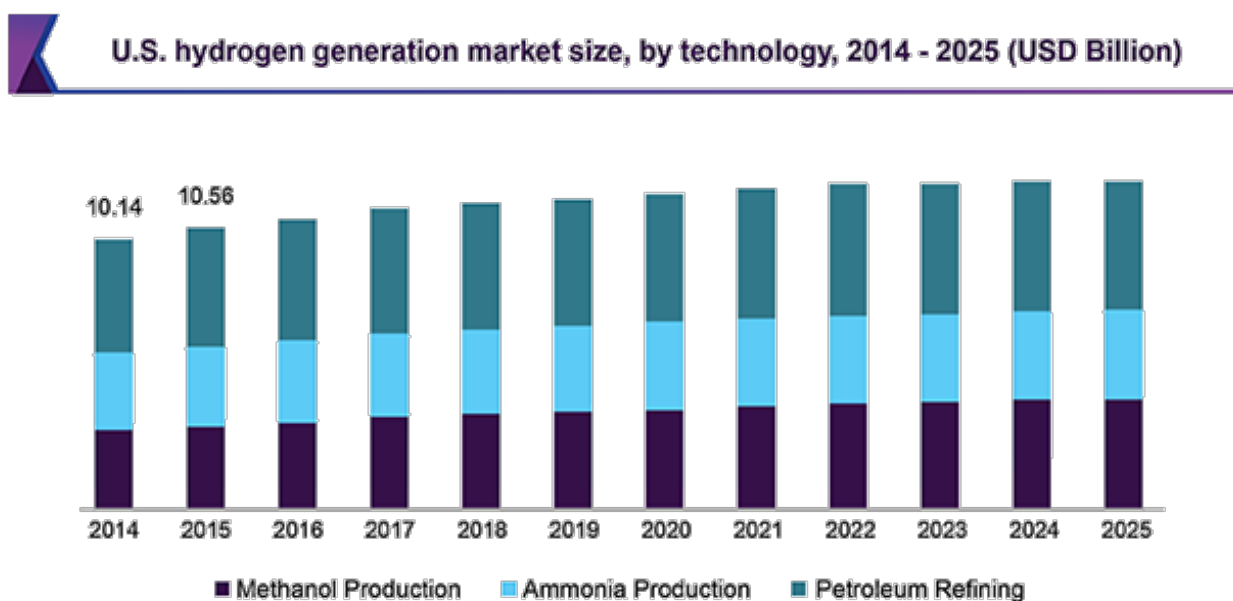
Figure 3.1. US hydrogen generation market size and the predicted future trend in three major sectors (NH$_3$ production with Haber-Bosch process, refining a wide range of petrochemicals, methanol production). Image credit: GrandViewResearch Inc.

The main source for producing more than 95% of hydrogen is based on depleting fossil fuel resources[94,95] (Figure 3.2), which also has an adverse effect on climate change. In this context, research on exploring renewable, sustainable, and more environment friendly processes to meet this ever increasing demand of hydrogen production has gained a large interest from both industrial and academic research communities.
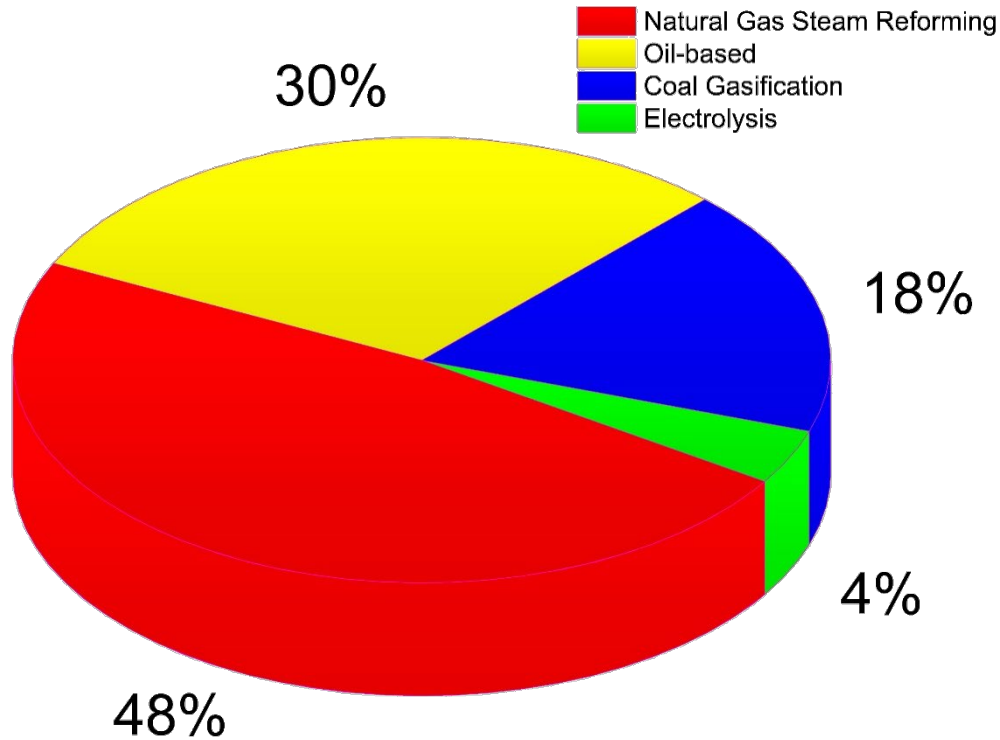
Figure 3.2: Share of production method for global hydrogen supply.

The most promising among the alternative methods is the hydrogen production through splitting of water following the dissociation reaction below.

$$H_2O_{(l)} \rightarrow H_{2\ (g)} + \frac{1}{2}O_{2\ (g)}$$
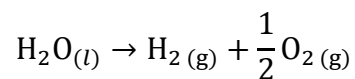
There are currently three approaches available for this clean production of hydrogen: photochemical, photoelectrochemical, and electrochemical methods. The most common among these three methods is the electrochemical method (Figure 3.2), which is also the focus of this project herein.

Under standard conditions (298 K temperature and 1 atm pressure), the related thermodynamic changes of the water splitting are +285.84 kJ mol^{-1} in enthalpy (ΔH^o), +237.22 kJ mol^{-1} in Gibbs free energy (ΔG^o), and +0.16315 kJ mol^{-1} K^{-1} in entropy (ΔS^o)[96,97]. The thermodynamic potential (E^o) of the electrolyzer is defined by the following reaction below.

$$E^0 = \frac{\Delta G^0}{zF}$$

Here, z denotes the number of exchanged electrons (i.e., in this reaction, it is two electrons) and F is the Faraday constant (96485.33 C mol^{-1}). Therefore, under standard conditions, the thermodynamic potential for the electrolysis of water is +1.23 V. In reality, to split a water molecule, extra electrical potential is needed, which is known as the overpotential (denoted as η)[98]. Overpotential (η) arises mainly due to the existence of activation barriers at the electrodes, and the resistance present in the system (e.g., solution resistance, contact resistance, etc.). The efficiency of the electrolytic cell is represented by the overpotential, and as mentioned earlier, overpotential, and thus the cell efficiency, is dependent on the structure and the material of the cell electrodes. Since water is a poor ionic conductor, and a conductive electrolyte is necessary to facilitate electrolysis at operating voltage and

current density. For electrolysis of water commonly used conductive mediums are either alkaline or acidic electrolytes.

The associated cathodic (reduction) half reaction in the electrocatalysis of water is called the hydrogen evolution reaction (HER)[99], which is shown below.

$$2H^+_{(aq.)} + 2e^- \xrightarrow{\text{electrocatalyst (cathode)}} H_{2\,(g)}, \qquad E^0 = 0.0V$$
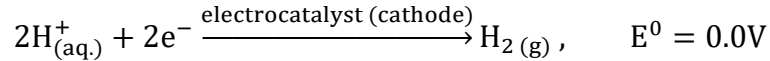
The anodic (oxidation) half reaction in the electrolytic water splitting is known as oxygen evolution reaction (OER). OER modeling is beyond the scope of this study.

$$4OH^-_{(aq.)} \xrightarrow{\text{electrocatalyst (anode)}} O_2 + 2H_2O_{(l)} + 4e^-, \ E^0 = -0.40V \quad \text{(alkaline medium)}$$

$$2H_2O_{(l)} \xrightarrow{\text{electrocatalyst (anode)}} O_2 + 4H^+_{(aq.)} + 4e^-, \ E^0 = -1.23V \quad \text{(acidic medium)}$$
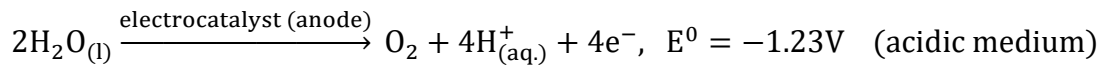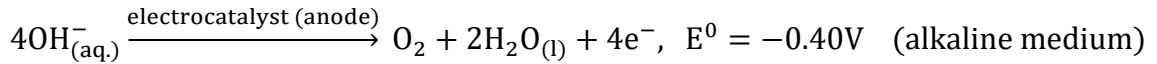
Both HER and OER require electrocatalyst materials, which will also act as a cathode and an anode respectively. The mechanism of HER involves three elementary reactions or steps[100]. The first step is called Volmer step. In this step H^+ ions go through electrochemically-driven adsorption and reduction.

$$H^+_{(aq.)} + e^- + * \rightleftharpoons H^* \quad \text{(acidic medium)}$$

$$H_2O_{(l)} + e^- + * \rightleftharpoons H^* + OH^-_{(aq.)} \quad \text{(alkaline medium)}$$
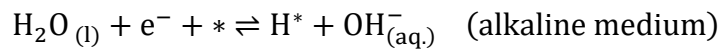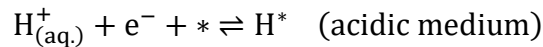
> Here * denotes the adsorption site on the electrocatalyst (cathode), and H* represents the surface adsorbed hydrogen atom.

Following the adsorption in Volmer step, desorption of hydrogen occurs in two possible ways known as the Heyrovsky step or the Tafel step. In the Heyrovsky step, the desorption occurs as an electrochemical phenomenon as shown below.

$$H^+_{(aq.)} + H^* + e^- \rightleftharpoons H_{2\ (g)} \quad \text{(acidic medium)}$$

$$H_2O_{(l)} + H^* + e^- \rightleftharpoons H_{2\ (g)} + OH^-_{(aq)} \quad \text{(alkaline medium)}$$
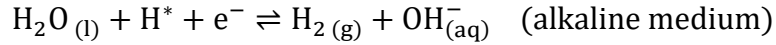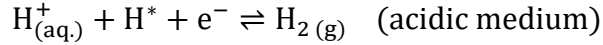
The Tafel step occurs due to the chemical desorption, and it remains the same in the both acid and alkaline medium as shown below. The Tafel step is commonly used as a key molecular description representing the rate determining step of HER in the literature by computational scientists.[101]

$$2H^* \rightleftharpoons H_{2\ (g)}$$
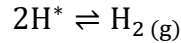
HER also exhibits the presence of an activation barrier at the cathode detected as a part of the overpotential. All of the above mentioned reactions are competing and the slowest one is normally the rate determining for HER. Free adsorption sites (denoted as *) is essential for HER to commence, and, for a constant set of process conditions, the electrode surface structure and composition is pivotal to influence the rate of HER. The reaction rate of HER (generally denoted as v) is usually measured through the experimental current density (i), which is proportional to v. The current density is normally expressed by the Butler-Volmer equation below[102,103].

$$i = i_0 \left[e^{(1-\alpha)\frac{zF\eta}{RT}} - e^{-\alpha\frac{zF\eta}{RT}} \right]$$

Here, i_0 is the exchange current density which reflects intrinsic rates of electron transfer between a chemical species and the electrode, α represents barrier symmetry factor which

is a charge transfer coefficient in the case of a single step reaction[104], F is the Faraday

constant, R is the universal gas constant, T is the temperature, and z denotes the number of

exchanged electrons. The exchange current density (i_0) is the hypothetical anodic and

cathodic current component in the dynamic equilibrium condition when the net current

density is zero.[5,98] The charge transfer coefficient is a dimensionless parameter with a value

ranging from zero to one.[105] It signifies the change in free energy barrier due to the change

of the electrode-electrolyte interfacial potential.

$$\text{VH: } i_0 = -2Fk_2^0 \left(\frac{e^{\frac{(1-\beta)\Delta G_b - \alpha FE_{SHE}}{RT}}}{1 + \frac{k_{-1}^0}{k_1^0[H^+]} e^{\frac{FE_{SHE} + \Delta G_b}{RT}} + \frac{k_2^0}{k_1^0} e^{\frac{\Delta G_b}{RT}}} \right)$$

$$\text{VT: } i_0 = -2Fk_3^0 \left(\frac{e^{\frac{(1-\beta)\Delta G_b}{RT}}}{1 + \frac{k_{-1}^0}{k_1^0[H^+]} e^{\frac{FE_{SHE} + \Delta G_b}{RT}}} \right)^2$$

With the presence of a large overpotential at the anode (or the cathode) the Butler-Volmer

equation can be simplified into Tafel equation below.

$$\eta = b \times \log_{10} \left(\frac{i}{i_0} \right)$$

$$\Rightarrow \eta = b \times \log_{10} i + a$$

Here 'b' is known as the Tafel slope, which represents the efficiency of an electrocatalyst

and can be determined experimentally, and 'a' ($= -b \times \log_{10} i_0$) is known as Tafel

constant.

The efficiency of an electrocatalyst is influenced by many factors, like adsorption & desorption energetics, crystallinity, the roughness and the interaction with supporting materials, conductivity, electronic and structural properties, adsorption site specificity on the electrode surface, etc. For some of these major quantities[12,106] (e.g. electronic and structural properties, adsorption energetics, adsorption site specificity inside the same material) to gauge the catalytic ability, experimental measurements are not very accessible or even possible without significantly perturbing the system. Computational chemistry can thus serve a very crucial role, not only to gain this microscopic information, but also to elucidate the true origin of catalytic power.

The importance of adsorption energetics is expressed clearly with Sabatier's principle. When hydrogen adsorption on catalyst sites is neither too strong nor too weak, this principle states that the HER exchange current density (representing the measured reaction rate) would be maximum. As previously stated with the introduction of the Tafel step, one of the most accepted quantitative descriptors of this principle is the adsorption free energy of hydrogen for which the ideal interaction (or adsorption energy) would be zero[106,107]. So far, platinum and other platinum-based alloys with other precious metals have exhibited the best electrocatalytic properties for the HER process[108]. Many detailed experimental and computational studies have been carried out for these HER electrocatalysts.[106,109] The free energy of hydrogen adsorption for Pt has been found almost thermoneutral or zero.[110,111] However, constraints on the availability and the high cost of these materials make their large-scale implementation very limited[95,112].

Nonprecious metal electrocatalysts, especially nonprecious transition metal alloys and their modification for catalytic improvement, have emerged as a major research focus. Non-noble metals exhibit poor catalytic performance for HER[113], but some alloys showed potential for HER electrocatalysis.[114] Among these nonprecious metal catalysts, the molybdenum dichalcogenides have shown significant potential as the HER electrocatalyst.[111,115,116] Molybdenum dichalcogenides have layered structures, where the 3D bulk material is comprised of many 2D monolayered molybdenum dichalcogenides structures. Each monolayer has a plane of molybdenum atoms which is sandwiched by 2 planes of chalcogenides ions. Among these molybdenum dichalcogenides, molybdenum ditelluride ($MoTe_2$) has the lowest band gap, and thus the highest electronic conductivity[117,118]. Many studies have demonstrated that molybdenum dichalcogenide nanoparticles and nanostructures have improved catalytic power than a bulk crystal with less exposed surface area[119–124].

To construct the cathode with these nanocatalysts, graphene shows remarkable promise as the supporting material due to its electronic and mechanical properties.[125–127] There are multiple studies that have been performed on MoS_2/graphene and $MoSe_2$/graphene nanocomposites for HER catalysis.[101,128–130] However, to the best of our knowledge, no similar work has been done with $MoTe_2$/graphene nanocomposite as the HER electrocatalyst. In this project, we have carried out collaborative investigations with Dr. Xinyu Zhang's research group at Auburn University to probe the catalytic properties of the $MoTe_2$/graphene nanocomposite for HER. Ms. Shatila Sarwar and Dr. Xinyu Zhang have developed a unique method to synthesize uniformly dispersed $MoTe_2$ nanoparticles on

graphene sheet networks, and the team experimentally measured the cathodic current density along with the overpotential. To illuminate the catalytic principles, the computational modeling of the $MoTe_2$/graphene nanocomposite as an electrocatalyst for HER at atomistic level has been carried out. It should be mentioned that for sustainable and efficient hydrogen production through electrolyzing water, along with HER electrocatalyst, OER catalyst at anode also plays a crucial role. OER is one of the significant sources of energy loss due to the more complex anodic surface reactions.

The main focus for the atomistic modeling is to illuminate whether the free energy of the hydrogen adsorption (more specifically chemisorption, also known as binding energy) on $MoTe_2$/graphene nanocomposite is near zero and to elucidate the most effective surface sites on this nanocomposite. Another target is to construct the most prominent graphical representation of Sabatier's Principle, also known as the volcano plot[131,132], where the experimentally measured exchange current density is plotted against the theoretically calculated hydrogen adsorption free energy for various catalytic electrodes.

The results from experimental measurement and the theoretical calculations have placed the $MoTe_2$/graphene nanocomposite near the peak of the volcano plot, almost with similar height of Pt, and considerably above MoS_2[110,111,133]. The combination of active $MoTe_2$ catalyst with extremely strong and conductive graphene support enhances the properties of individual components, and thereby exhibits a higher overall performance for HER. These results are pursued in our proposed research projects as the future commercialization of

MoTe2/graphene and closely related nanocomposites for practical HER applications is promising and warrants further investigation.

3.2. Method:

Computational modeling of a solid-state with periodic structure is normally performed with periodic plane-wave quantum chemical calculations (commonly, DFT method based). In the theory underlying this periodic plane-wave DFT method, in addition to the Schrödinger equation, the Bloch theorem also plays an important role. This theorem states that, the wave function inside a lattice must satisfy the following equation

$$\psi(\vec{r}) = e^{i\vec{k}\cdot\vec{r}}u(\vec{r})$$

Here ψ is the electronic wavefunction inside the periodic solid, $u(\vec{r}) = \sum_G C_G e^{i\vec{G}\cdot\vec{r}}$, $\vec{G}$ is the reciprocal lattice vector, and $\vec{k}$ is the wave vector (momentum, $\vec{p} = \hbar\vec{k}$).

The atomistic simulation of the nanocomposite is performed with periodic plane-wave DFT using the Cambridge Serial Total Energy Package (CASTEP)[134]. For the DFT, the spin polarized generalized gradient approximation (GGA)[85] with Perdew-Burke-Ernzerhof (PBE)[135] functional has been employed with an energy cutoff of 400 eV. The cutoff energy is determined by the equation, $E_{cutoff} \geq \frac{\hbar}{2m_e}|\vec{G}|^2$. In the model, the solid lattice can be regarded as comprised of the free valence electrons and nuclei containing ionic cores. Each ionic core has tightly bound core electrons along with its nucleus. To represent properly

these ionic cores, pseudopotential concepts are introduced, which approximate the interaction of the overall potential felt by the valence electrons, thus replacing the complicated effect of the nonvalence electrons in the ionic core. In this calculation, the effect of the core electrons has been expressed with the Vanderbilt Ultrasoft Pseudopotentialls (USPP) method.[136]

To provide hydrogen chemisorption energies and geometries for the $MoTe_2$/graphene composite in line with experimental observations, an improved description of the nonlocal nature of the electron correlation and in particular van der Waals interactions was accounted for using a semi-empirical dispersion energy correction by the method of Tkatchenko and Scheffler (TS).[23] All structures are geometry optimized using the two point steep gradient displacement (TPSD) algorithm.[137] For the dipole correction, a self-consistent scheme has been applied.[138] Relativistic treatment has been done with Koeling-Harmon Scalar method.[139]
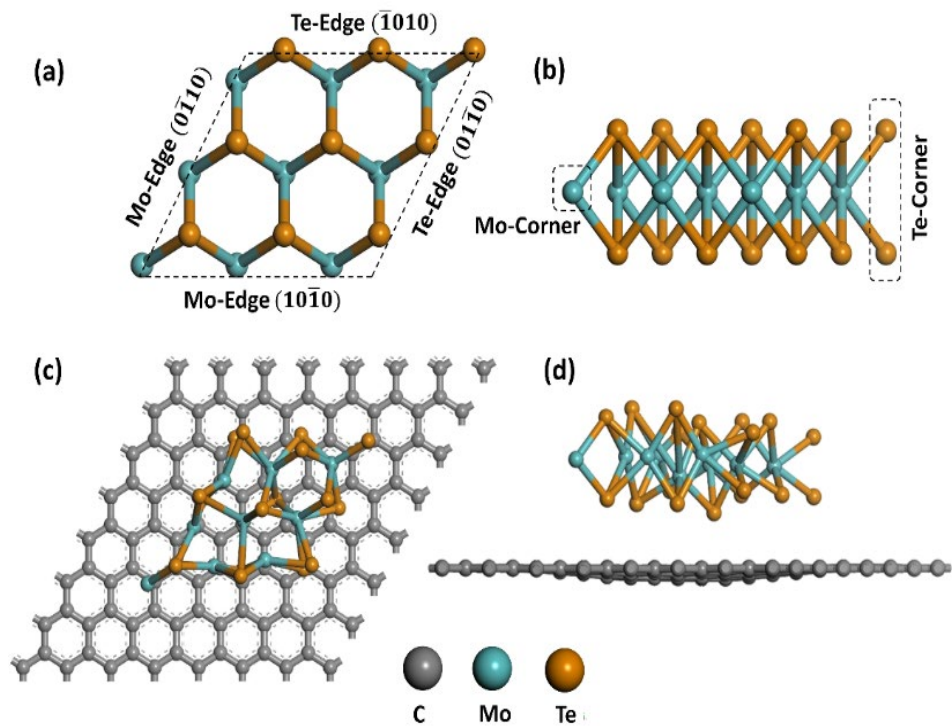
Figure 3.3: Molecular structure of MoTe$_2$/graphene composite from DFT calculation. (a) Top and (b) side views of the Mo$_9$Te$_{18}$ nanoparticle taken from a structurally optimized MoTe$_2$ crystal. (c) Top and (d) side views of the Mo$_9$Te$_{18}$ nanoparticle over 7×7×1 graphene supercell with optimized geometries. Dashed lines in (a) highlight the edge sites and dashed rectangles in (b) denote the corner sites.

As presented in Figure 3.3, the MoTe$_2$/graphene composite was created by constructing a supercell model of MoTe$_2$ with 3×3 in plane periodicity supported on a 7×7×1 graphene basal plane. The supported MoTe$_2$ nanoparticles have the molecular formula of Mo$_9$Te$_{18}$, where the Mo and Te atoms assume the most common metal di-chalcogenide layered structure. The Mo$_9$Te$_{18}$ nanoparticle used in the composite was previously geometry optimized in the solid state hexagonal MoTe$_2$ lattice. For the cleaved Mo$_9$Te$_{18}$ nanoparticle, the $(01\bar{1}0)$ plane best represents the exposed Te edge, and similarly the $(10\bar{1}0)$ plane best

represents the exposed Mo edge. A vacuum space of 20 Å has been used between vertically

repeated composite models. The Brillouin zone has been sampled by a 2×2×1 k-point grid

generated using Monkhorst-Pack scheme.[140] The convergence criteria for energy were set

to 2×10^{-5} eV per atom and for displacement this tolerance was set to 0.002 Å.

3.3. Results and Discussion:

For the computational study, multiple hydrogen adsorption sites on the Mo$_9$Te$_{18}$ nanoparticle were investigated for the hydrogen adsorption processes. For each of these sites, adsorption energy has been calculated for the Tafel reaction, $2H^* \leftrightharpoons H_{2(g)} + 2*$ (here * denotes the adsorption site on cathode, and H* is the adsorped hydrogen atom on cathode surface), along with band structures and density of states. The band structures and density of states have not been presented here, but this data is available upon request. The adsorption energy of a single H atom on was calculated using the equation:

$$\Delta E_{adsorption} = \frac{1}{2}(E_{2H^*+MoTe_2/graphene} - E_{MoTe_2/graphene} - E_{H_2}).$$

Here, $E_{2H^*+MoTe_2/graphene}$ is the total electronic energy of the two hydrogen atoms bound to the Mo$_9$Te$_{18}$ nanoparticle-graphene composite, $E_{MoTe_2/graphene}$ is the total electronic energy of Mo$_9$Te$_{18}$ nanoparticle-graphene composite, and E_{H_2} is the electronic energy of hydrogen molecule placed in a 17.2 Å×17.2 Å×20.0 Å vacuum hexagonal unit cell. These adsorption energies were calculated to determine the optimal active catalytic sites on the MoTe$_2$/graphene nanocomposite catalyst responsible for HER activity.

To illustrate the Sabatier's principle as applied to HER activity, a more suitable descriptor to represent activity on a volcano plot for the Tafel reaction is the binding free energy ($\Delta G_{adsorption}$) instead of binding electronic energy alone ($\Delta E_{adsorption}$). Binding free energy

has been calculated using the generalized expression for HER catalysis developed by Nørskov and co-workers[110] with the following equation:

$$\Delta G_{adsorption} = \Delta E_{adsorption} + 0.24 \; eV.$$

The results are shown in the table and figure below.

Table 3.1: Electronic and Free Energy of adsorption of hydrogen on the different sites of MoTe$_2$/graphene nanocomposite

	Adsorption sites	$\Delta E_{adsorption}$ (eV)	$\Delta G_{adsorption}$ (eV)
1	Mo corner	−0.507	−0.267
2	Mo edge	0.186	0.426
3	Te top surface	1.083	1.323
4	Te corner	0.818	1.058
5	Te edge	0.583	0.823
6	Mo edge-Te edge	−0.143	0.097
7	Mo corner-Te edge	0.140	0.380

As shown in Figure 3.4 and Table 3.1, among the hydrogen adsorption sites considered, the exposed Mo corner (site 1) and the Mo edge adjacent to Te edge (site 6) on Mo$_9$Te$_{18}$ nanoparticle exhibited the lowest $\Delta E_{adsorption}$ values, −0.507 and −0.142 eV, respectively. These results suggest the sites on the representative Mo edge (10$\bar{1}$0) likely contribute to the high reaction rates observed for HER catalysis.

The absolute free energy values, $|\Delta G_{adsorption}|$ of 0.267 and 0.097 eV also indicate the same conclusion. Thus, the optimal catalytic active site for hydrogen evolution is the bridge site

between the Mo and Te atoms on the representative Mo edge ($10\bar{1}0$). After finding the two most effective sites using the free energy equation developed by Nørskov et al., the Gibbs free energy for hydrogen adsorption were determined for these two sites computationally utilizing the computationally-demanding phonon calculation on the true nanocomposite structure. This more specific calculation showed similar near thermoneutral values for the best two points, underlying the fact that the representative equation from Norskov and co-workers was effective in capturing the entropic effects for hydrogen adsorption. As is common within a reactive class, the entropic change due to the adsorption step across different material types is similar and conserved.
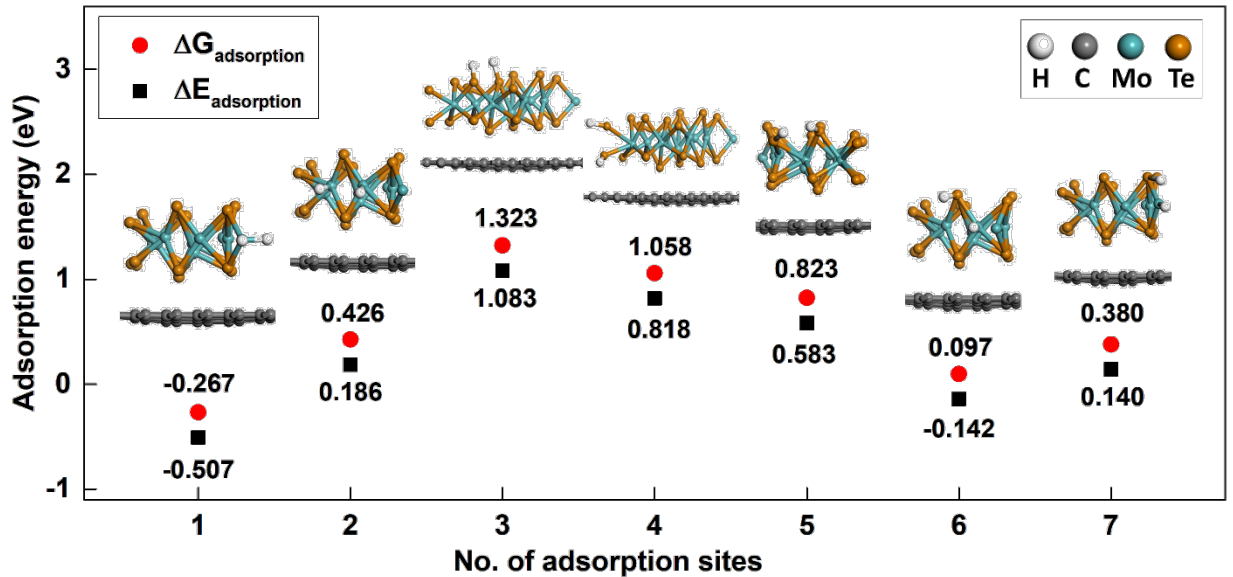
Figure 3.4: Adsorption energies of different Mo_9Te_{18} nanoparticle sites. The calculated binding free energy ($\Delta G_{adsorption}$) and binding electronic energy ($\Delta E_{adsorption}$) values at different adsorption sites of $MoTe_2$/graphene composite. The adsorption site indexing is as follows: (1) Mo corner, (2) Mo edge, (3) Te top surface, (4) Te corner, (5) Te edge, (6) Mo edge-Te edge, and (7) Mo corner-Te edge

To make these result more perceptible, the free energy diagram of adsorption and the desorption has been demonstrated in Figure 3.5. Moreover, using the calculated hydrogen binding free energy ($\Delta G_{adsorption}$) for these sites and the experimental value of exchange current density (i_0), the points for the MoTe$_2$/graphene nanocomposite on the volcano plot (Figure 3.5) were found nearly thermoneutral, approaching towards the high-performing metals such as Pt.
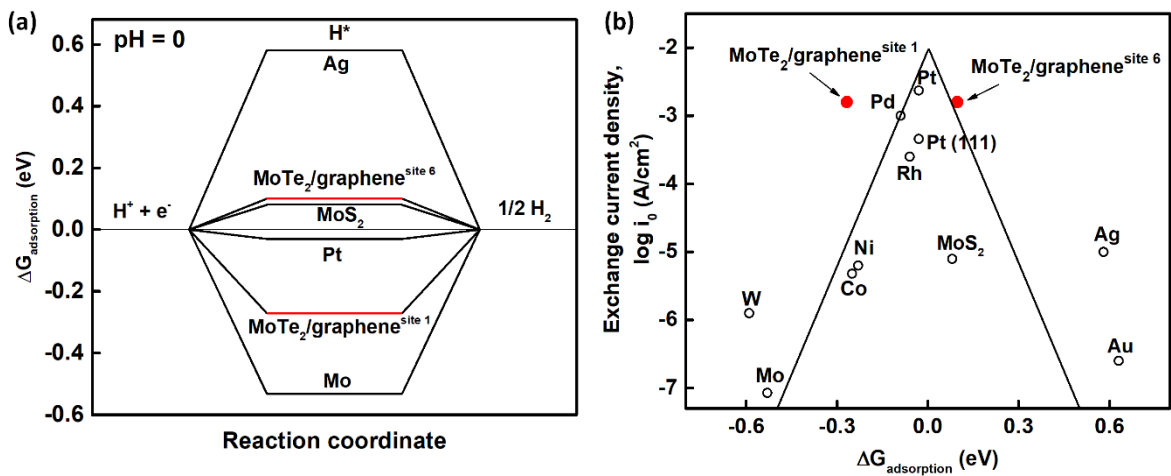
Figure 3.5: (a) Hydrogen adsorption free energy ($\Delta G_{adsorption}$) diagrams at equilibrium (U = 0 V). (b) Volcano plot of experimentally measured exchange current density (i_0) as a function of the DFT-calculated Gibbs free energy of adsorbed atomic hydrogen ($\Delta G_{adsorption}$). Data for different metals and MoS$_2$-catalyst have been adapted from ref. 48 and ref. 49, respectively.[110,145] MoTe$_2$/graphene[site 1] and MoTe$_2$/graphene[site 6] represent Mo corner and Mo edge-Te edge adsorption sites, respectively.

3.4. Conclusion:

In summary, computational results demonstrated the correlation between the hydrogen chemisorption free energies and the exchange current densities for HER, identifying the most active sites on catalyst structures. Mo corner and bridge sites of Mo and S in the nanocomposites are the most catalytically active sites. Modifying $MoTe_2$/Gr to increase such sites holds high potential for real-life application.

Moreover, the volcano plot (combined with both experimental and computational results) indicated that graphene supported $MoTe_2$ is a promising electrocatalyst compared to other metals because the hydrogen evolution reaction is near thermoneutral on $MoTe_2$/graphene, similar to Pt at the equilibrium potential.

4. Systematic study of hybrid and non-hybrid Molybdenum dichalocogenides over graphene nanocomposites as electrocatalysts for HER

4.1. Introduction:

Finding a renewable method for hydrogen production to meet the current industrial demand and to make an alternative energy carrier has become imperative for a sustainable future.[141–143] The primary source for renewable hydrogen generation is water splitting by electrocatalysis.[144] At present, the generation of hydrogen through electrolysis of water, also known as the hydrogen evolution reaction (HER), is limited by the high cost and availability of precious metals (Pt, Pd, Ru, Ir) and respective alloys, which have been shown the best performers as electrocatalysts.[110,145–152] Among the precious metals, Pt exhibits the best values for most of the descriptors necessary for effective catalysis.[146] In this scenario, the search for alternatives to precious metal electrocatalysts, especially nonprecious transition metal alloys and modification for catalytic improvement, has emerged as a significant research direction. Non-noble metals exhibit poor catalytic performance for the HER, but some transition metal compounds and their alloys showed potential for HER electrocatalysis.[113,114]

Among these nonprecious metal based catalysts, the molybdenum dichalcogenides ($MoCh_2$) have shown significant potential as HER electrocatalysts both experimentally and theoretically.[111,115,116] Molybdenum dichalcogenides have layered structures, where the 3D bulk material is comprised of multiple 2D monolayered molybdenum dichalcogenides structures with polytype 2H or 3R. Each monolayer has a plane of molybdenum atoms which is sandwiched by 2 planes of chalcogenide ions. Many theoretical and experimental

studies have demonstrated that nanoscale engineering of molybdenum dichalcogenide has improved catalytic power more than a bulk crystal with less exposed surface area. Phase conversion of $MoCh_2$ from 2H to 1T phase has shown an increase in catalytic performance.[116,120,153–155] Engineering porosity along with defects in the nanostructures and creating quantum dots with $MoCh_2$ have also shown improved performance for HER catalysis.[123,124,156–158] To construct the cathode with these nanocatalysts, graphene shows remarkable promise as the supporting material due to its electronic and mechanical properties.[125–127] Multiple studies that have been performed on MoS_2/graphene, $MoSe_2$/graphene, and $MoTe_2$/graphene nanocomposites for HER catalysis.[101,128–130,159] The HER activity of these nanostructures and nanocomposites can be tuned with doping or hybridization, specifically Mo with other transition metals, one type of chalcogen with another, and doping of the carbon in graphene structure.[160–167] Multiple studies in literature, both experimental and theoretical showed promising prospects of hybrid molybdenum chalcogenides (e.g., MoS_xMoSe_{2-x}, $MoSe_xTe_y$, MoS_xSe_y/Gr, MoS_xTe_y/Gr) for HER catalysis.[168–173] To the best of our knowledge no systematic investigation of various types of molybdenum dichalcogenides (hybrid or non-hybrid) with graphene nanocomposites for HER catalysis has been reported in the literature.

In the computational section of this work, atomistic modeling studies have been performed with periodic plane-wave density functional theory (DFT) to delve into the surface-electrochemistry of hydrogen binding (also known as chemisorption or adsorption). Binding energetics, which are considered major descriptors for catalytic performance but difficult to attain with experimental measurement, have been calculated with DFT. The critical role of binding energy is stated by the Sabatier principle, that is, for ideal catalysis,

the binding energy of key intermediates should neither be too strong nor too weak to ensure optimal catalysis.[174–177] In the case of HER, the well-established interpretation of the Sabatier principle is that for optimum reaction rate, the binding free energy of hydrogen to the electrocatalyst surface should be zero.[110,131,132] In the computational part of this study, the conventional criterion of $\Delta G_b \approx 0$ has been considered as the measure to establish the most suitable binding sites for HER catalysis. However, a most recent study has suggested that the binding free energy may not be near zero for a catalytically active site.[178] As per the established norm, binding free energy calculations have been performed with zero applied overpotential ($\eta = 0$). In recent literature, an augmented approach to Sabatier's principle has surfaced, which states that for very active electrocatalysts the near zero binding free energy should be determined at an applied overpotential.[179] Upon computational analysis, all hybrid and non-hybrid $MoCh_2$/Gr nanocomposites were compared and structure-activity relationships were established to identify best performing active sites.

In the experimental section of this work carried out with by professor Xinyu Zhang lab, a direct growth strategy is applied to synthesize $MoCh_2$ compounds (MoS_2, $MoSe_2$ and $MoTe_2$) and several hybrid heterostructures (MoSSe, MoSeTe, MoSTe, and $MoS_{0.67}Se_{0.67}Te_{0.67}$) on graphene supports through a simple microwave-assisted heating approach. Benefiting catalysis, nanocomposites can provide synergetic interactions between transition metal dichalcogenides (TMD) and graphene nanosheets by way of the HER kinetic process and electronic structure modulations. The as-prepared compounds showed great potential as low-cost electrocatalysts for (HER). One established representation of catalytic efficacy is the volcano plot, where extrapolated exchange

current density (i_0) and theoretically calculated binding free energy of hydrogen (ΔG_b) are presented together in a semi-logarithmic graph.[180,181] Placing data from this study into the volcano plot showed that for MoCh$_2$/Gr nanocomposites, the volcano relationship does not hold for all scenarios. Similar findings were reported in the recent literature and are compared herein.[107,182,183]

4.2 Computational Methodology

The theoretical study has been performed utilizing periodic plane-wave density functional theory (DFT) calculations as implemented in the Cambridge Serial Total Energy Packages (CASTEP).[134,184–186] The spin polarized generalized gradient approximation (GGA) with Perdew-Burke-Ernzerhof (PBE) functional has been used with Kohn-Sham orbitals with an energy cutoff of 400 eV.[85,135] The effect of the core electrons has been expressed with the Vanderbilt Ultrasoft Pseudopotentials (USPP) method.[136] To provide hydrogen chemisorption energies and geometries for the $MoCh_2$/Gr nanocomposite in line with experimental observations, an improved description of the nonlocal nature of the electron correlation, in particular van der Waals interactions, was accounted for using a semi-empirical dispersion energy correction by the method of Tkatchenko and Scheffler.[23] All structures are geometry optimized using the two point steep gradient displacement (TPSD) algorithm.[137] For the dipole correction, a self-consistent scheme has been applied.[138] Relativistic treatment has been done with the Koeling-Harmon Scalar method.[139]

As presented in Figure 4.1, the $MoCh_2$/Gr composite was created by constructing a supercell model of $MoCh_2$ with 3×3 in-plane periodicity supported on a 7×7×1 graphene basal plane. The Mo_9S_{18}, Mo_9Se_{18}, and Mo_9Te_{18} nanoparticles were created using a geometrically optimized respective solid state hexagonal molybdenum dichalcogenide lattice. All of these structure are shown in Tables below. The $Mo_9Se_9Te_9$ and $Mo_9S_9Te_9$ nanoparticles was created by randomly replacing nine tellurium atoms from the Mo_9Te_{18} nanoparticle with sulfur or selenium atoms, respectively. The $Mo_9S_9Se_9$ nanoparticle was created by randomly replacing nine sulfur atoms from Mo_9S_{18} nanoparticle with selenium

atoms. The $Mo_9S_6Se_6Te_6$ nanoparticle was also generated by replacing twelve tellurium atoms from the Mo_9Te_{18} nanoparticle with six sulfur and six selenium atoms, respectively.
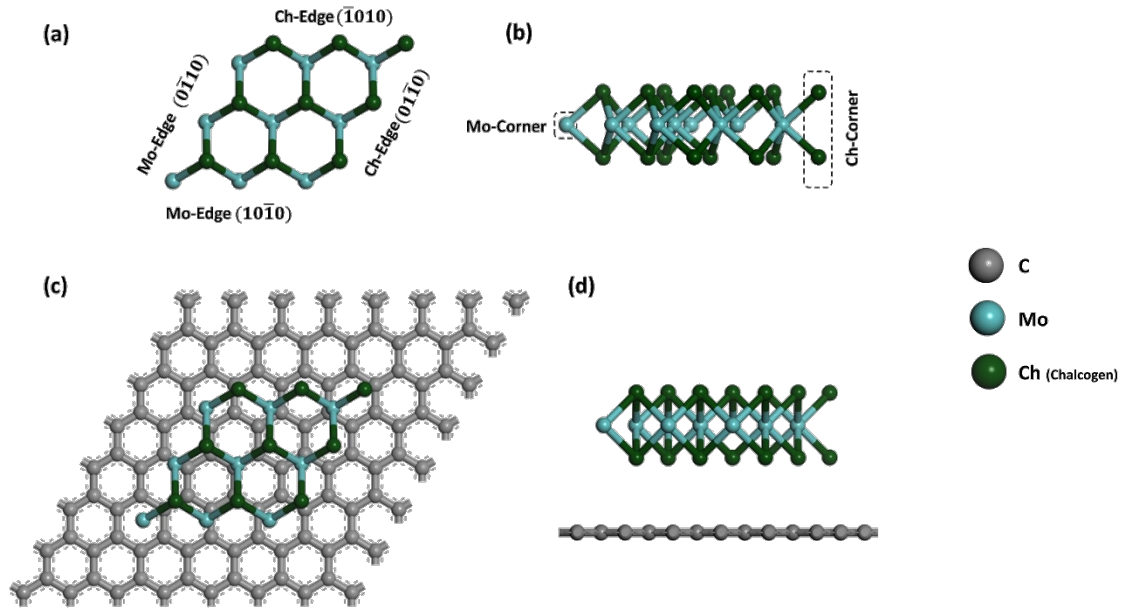
Figure 4.1: Generalized molecular structure of Mo_9Ch_{18}/graphene: (a) Top and (b) side views of a generalized Mo_9Ch_{18} nanoparticle. (c) Top and (d) side views of the Mo_9Ch_{18} nanoparticle over 7×7×1 graphene supercell with optimized geometries. *Dashed rectangles in (b) denote the corner catalytic active sites.*

Nanocomposites MoS$_2$/Gr, MoSe$_2$/Gr, MoTe$_2$/Gr, MoSSe/Gr, MoSeTe/Gr, MoSTe/Gr, and $MoS_{0.67}Se_{0.67}Te_{0.67}$/Gr are represented with Mo_9S_{18}/Gr, Mo_9Se_{18}/Gr, Mo_9Te_{18}/Gr, $Mo_9S_9Se_9$/Gr, $Mo_9S_9Te_9$/Gr, $Mo_9Se_9Te_9$/Gr, and $Mo_9S_6Se_6Te_6$/Gr respectively in the computational study.

Table 4.1. Optimized geometries of non-hybrid molybdenum dichalcogenide/graphene nanocomposite structures from periodic plane-wave DFT calculations.
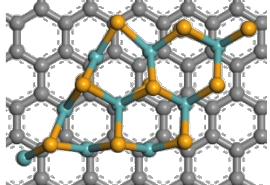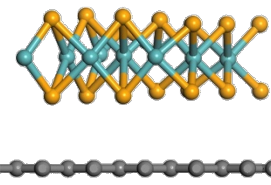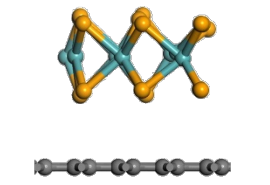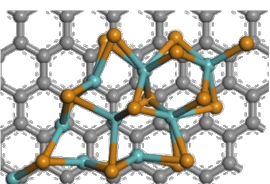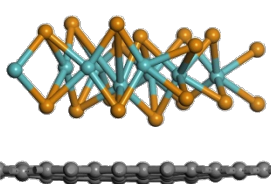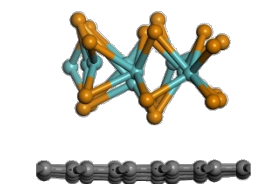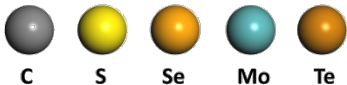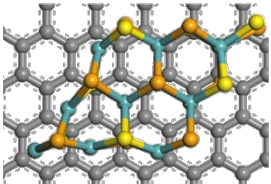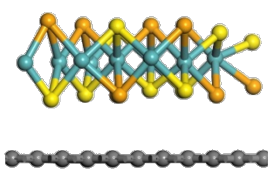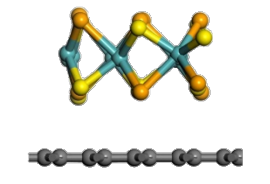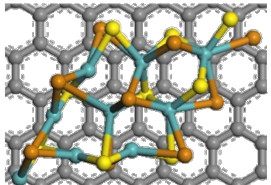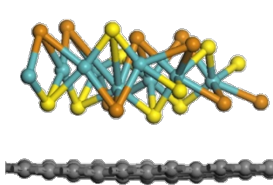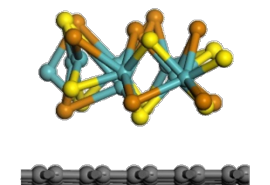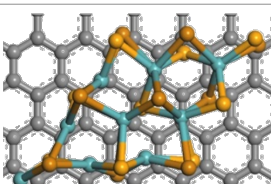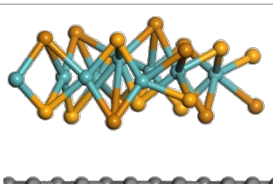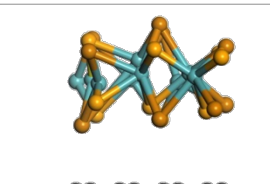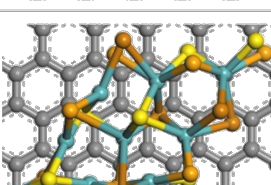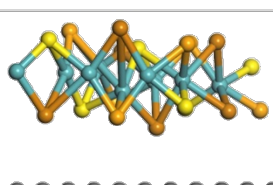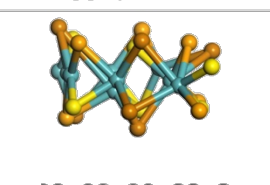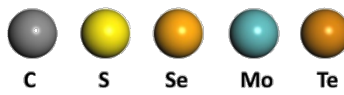
Non-hybrid Nanocomposite	Top View (Along Z axix)	Side vies (along X axis)	Side View (Along Y axis)
Mo_9S_{18}/Gr			
Mo_9Se_{18}/Gr			
Mo_9Te_{18}/Gr			

C   S   Se   Mo   Te

Table. Optimized geometries of hybrid molybdenum dichalcogenide/graphene nanocomposite structures from periodic plane-wave DFT calculat

Non-hybrid Nanocomposite	Top View (Along Z axix)	Side vies (along X axis)	Side View (Along Y axis)
$Mo_9S_9Se_9$/Gr			
$Mo_9S_9Te_9$/Gr			
$Mo_9Se_9Te_9$/Gr			
$Mo_9S_6Se_6Te_6$/Gr			
	C S Se Mo Te		

Ideally, a larger model of nanoparticles would be more representative as these structures would be similar to the nanoparticle dispersion on graphene supports observed in experimental literature. However, the computational costs and combinatorial explosion of possible configurations are beyond the scope of this current work, but it would be a promising prospect for future investigations.
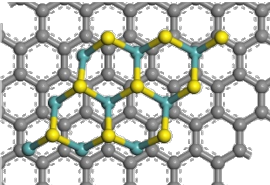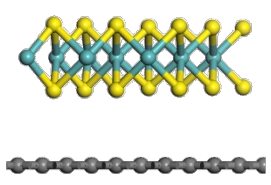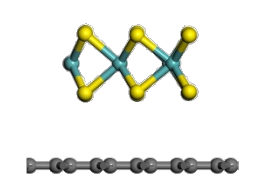
For the cleaved Mo_9Ch_{18} nanoparticle, the $10\bar{1}0$ plane best represents the exposed Ch edge, and similarly the $01\bar{1}0$ plane best represents the exposed Mo edge. A vacuum space of 20 Å has been used between vertically repeating composite models. The Brillouin zone has been sampled by a 2×2×1 k-point grid generated using Monkhorst-Pack scheme.[140] The convergence criteria for energy was $2×10^{-5}$ eV per atom and 0.002 Å for displacement, respectively.

Nine binding sites are considered for the Mo_9S_{18}/Gr, Mo_9Se_{18}/Gr, and Mo_9Te_{18}/Gr nanocomposite structures. For the $Mo_9S_9Se_9$/Gr, $Mo_9S_9Te_9$/Gr, $Mo_9Se_9Te_9$/Gr, and $Mo_9S_6Se_6Te_6$/Gr structures, adsorption energetics for fourteen binding sites are calculated. The binding sites are side-by-side chalcogen edge (site no. 1 & 2), Mo corner (site no. 3), chalcogen top (site no. 4 & 5), Mo and chalcogen edge (site 6 & 7), chalcogen edge and Mo corner (site no. 8), chalcogen corner (site 9), up-and-down chalcogen edge (site 10 & 11), Mo edge (site no. 12 & 13), and Mo corner-edge (site no. 14). The five extra sites in these nanocomposites (sites no 2, 5, 7, 11, & 13) are due to the structural asymmetry in the hybrid molybdenum dichalcogenide nanoparticles, and these five sites are not considered in the non-hybrid molybdenum dichalcogenide/graphene systems. The generalized orthographic multiviews of all these adsorption sites can be found in the following 14 figures below.

Top View (Along Z axis)   Side View (Along X axis)   Side View (Along Y axis)

H   C   Mo   Ch (Chalcogen)
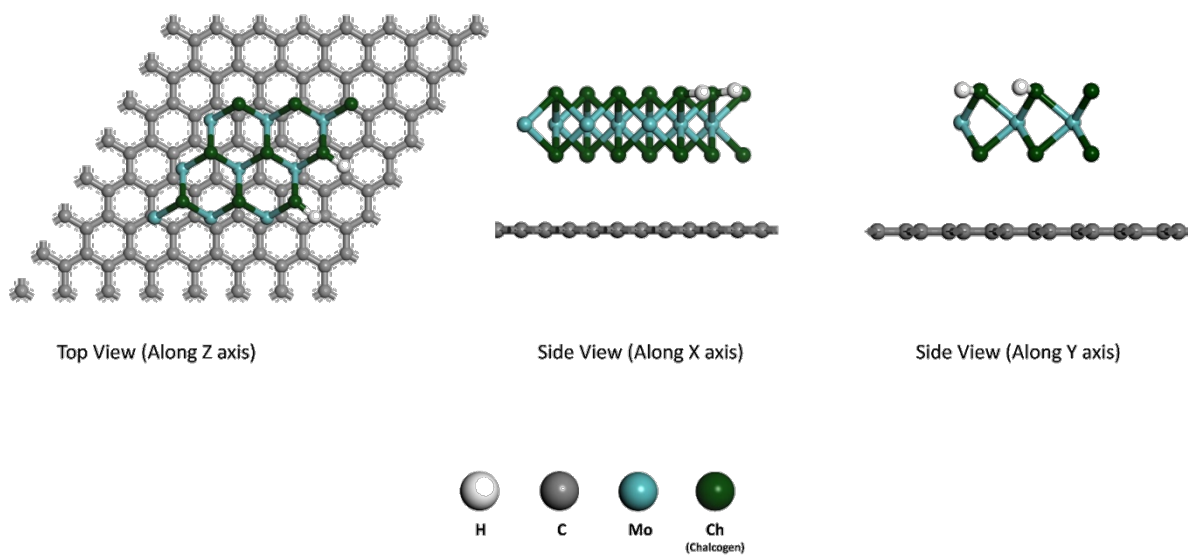
Figure 4.2: Multiview orthographic projection of adsorption site: side-by-side chalcogen edge 1 (site index no. 1).

Top View (Along Z axis)   Side View (Along X axis)   Side View (Along Y axis)

H   C   Mo   Ch (Chalcogen)
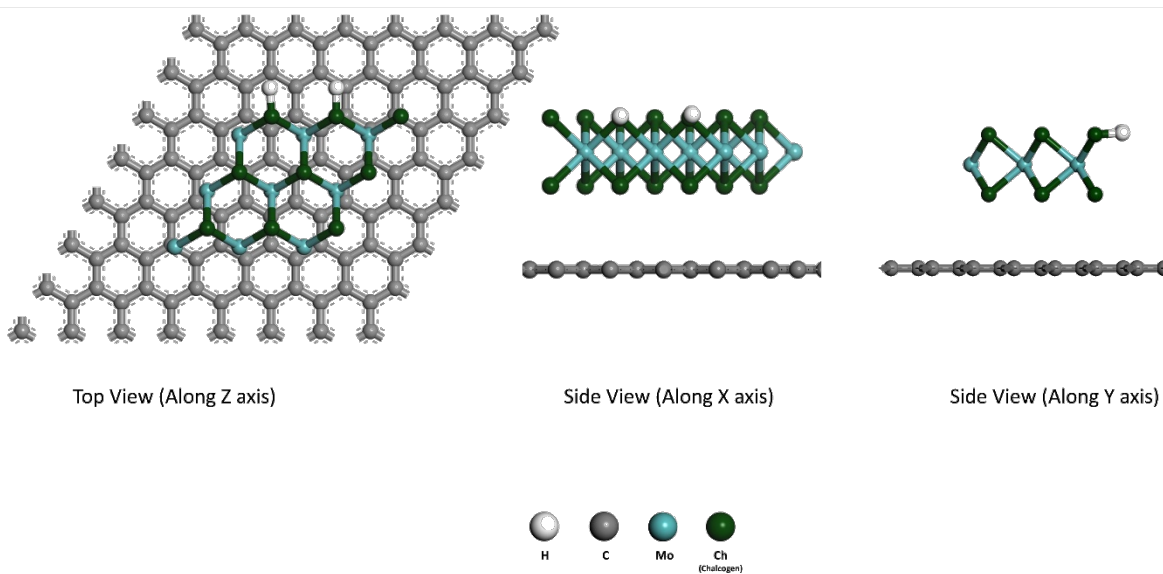
Figure 4.3: Multiview orthographic projection of adsorption site: side-by-side chalcogen edge 2 (site index no. 2).
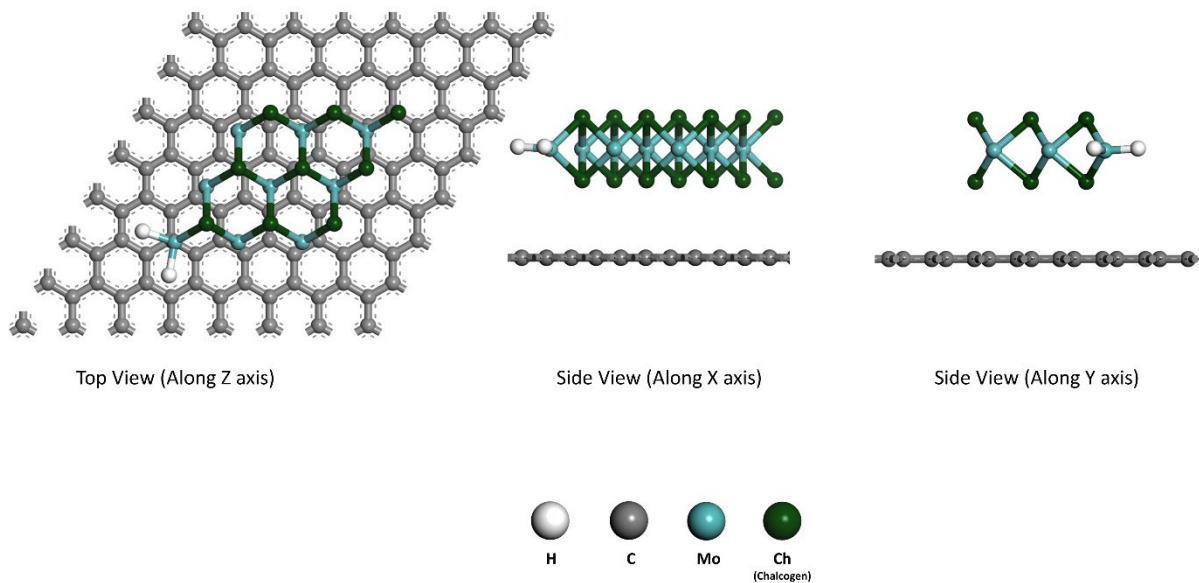
Figure 4.4: Multiview orthographic projection of adsorption site: Mo corner (site index no. 3).
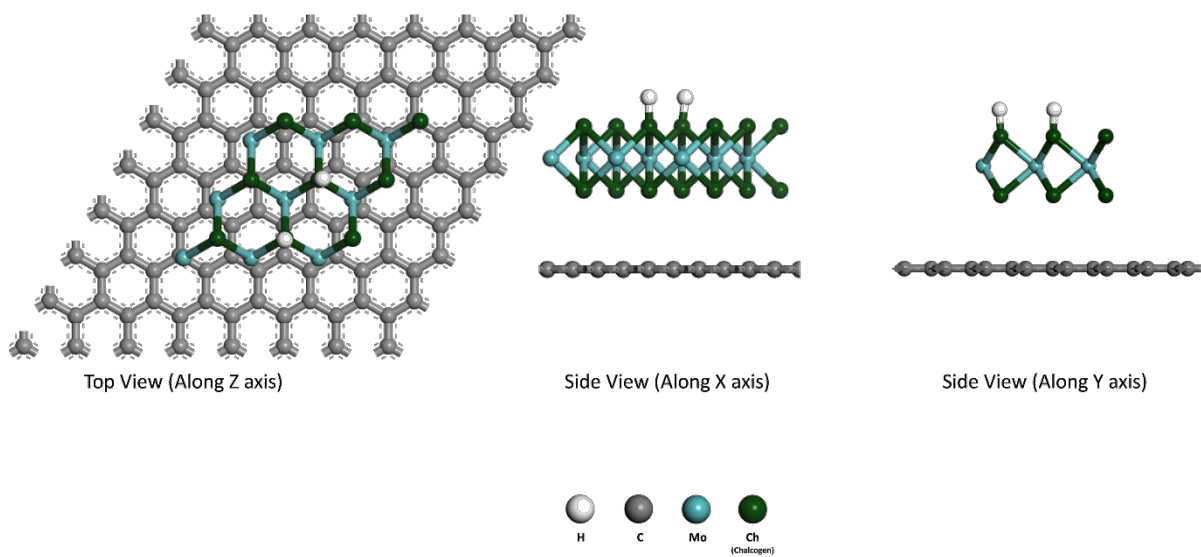
Figure 4.5: Multiview orthographic projection of adsorption site: chalcogen top 1 (site index no. 4).
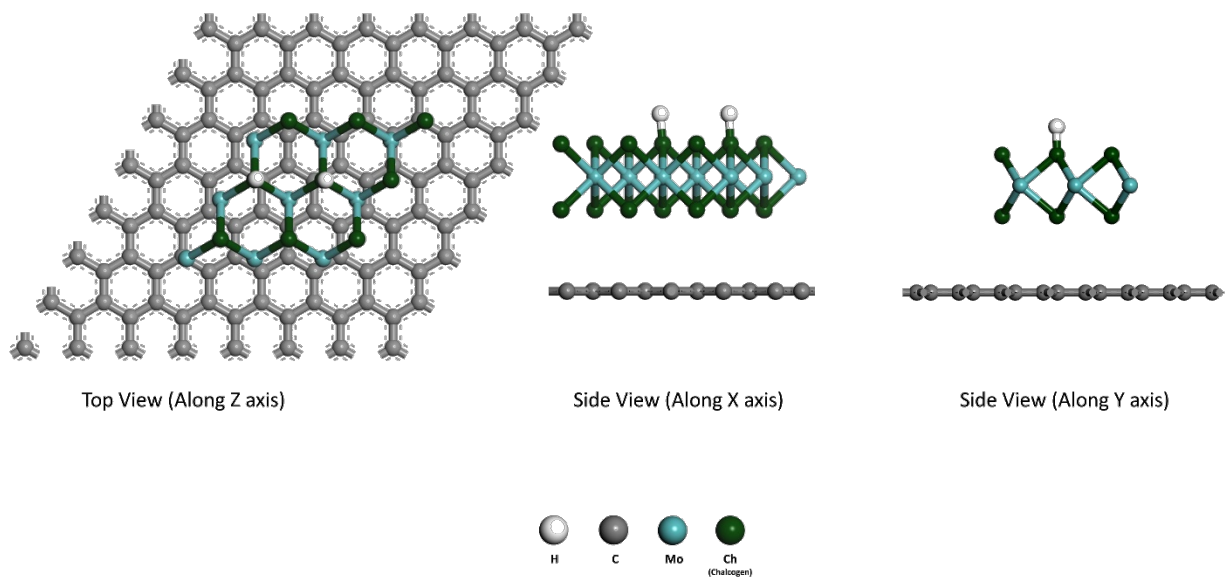
Figure 4.6: Multiview orthographic projection of adsorption site: chalcogen top 2 (site index no. 5).
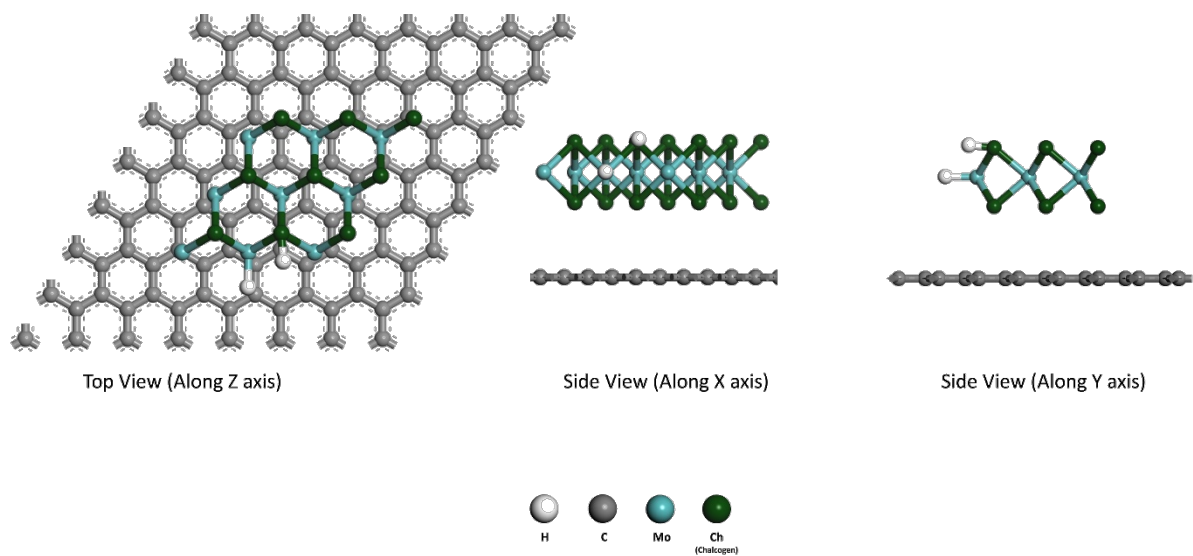
Figure 4.7: Multiview orthographic projection of adsorption site: Mo-chalcogen edge 1 (site index no. 6).
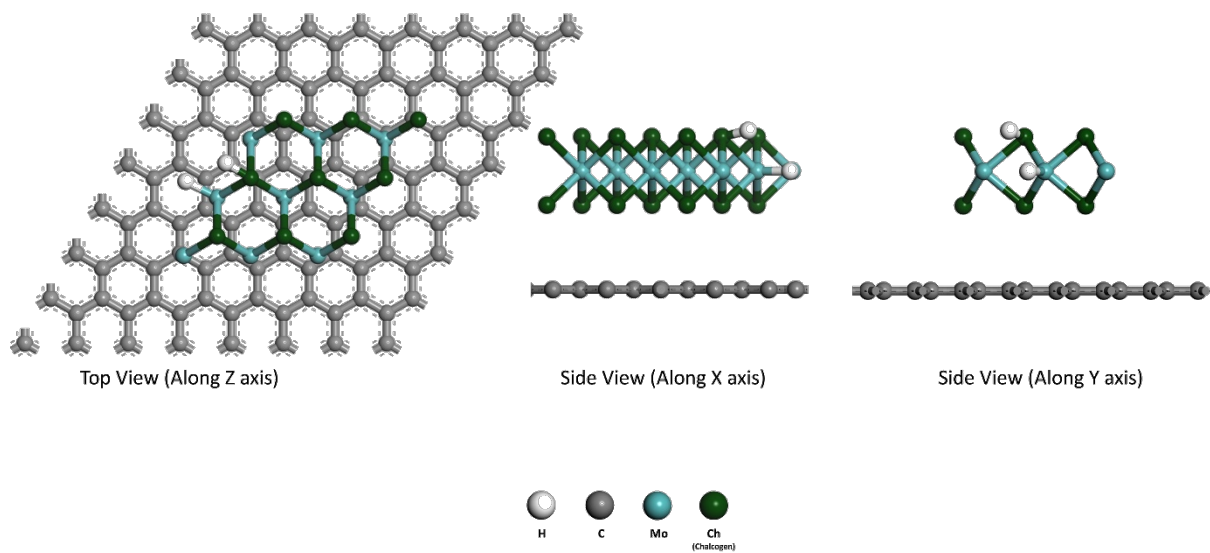
Figure 4.8: Multiview orthographic projection of adsorption site: Mo-chalcogen edge 2 (site index no. 7).
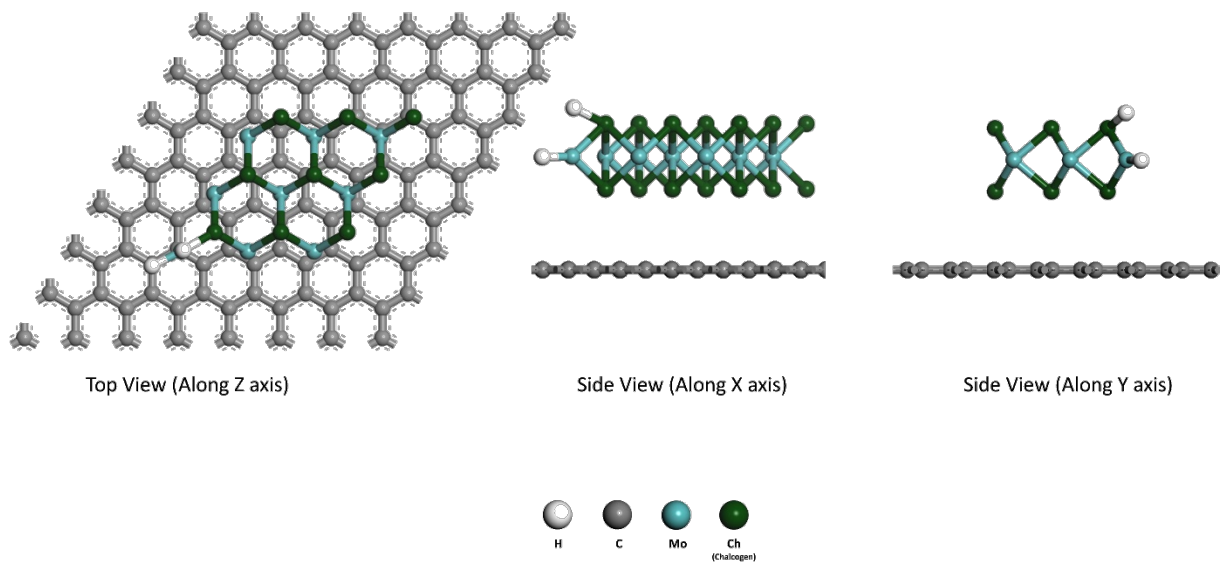
Figure 4.9: Multiview orthographic projection of adsorption site: Mo corner & chalcogen edge (site index no. 8).
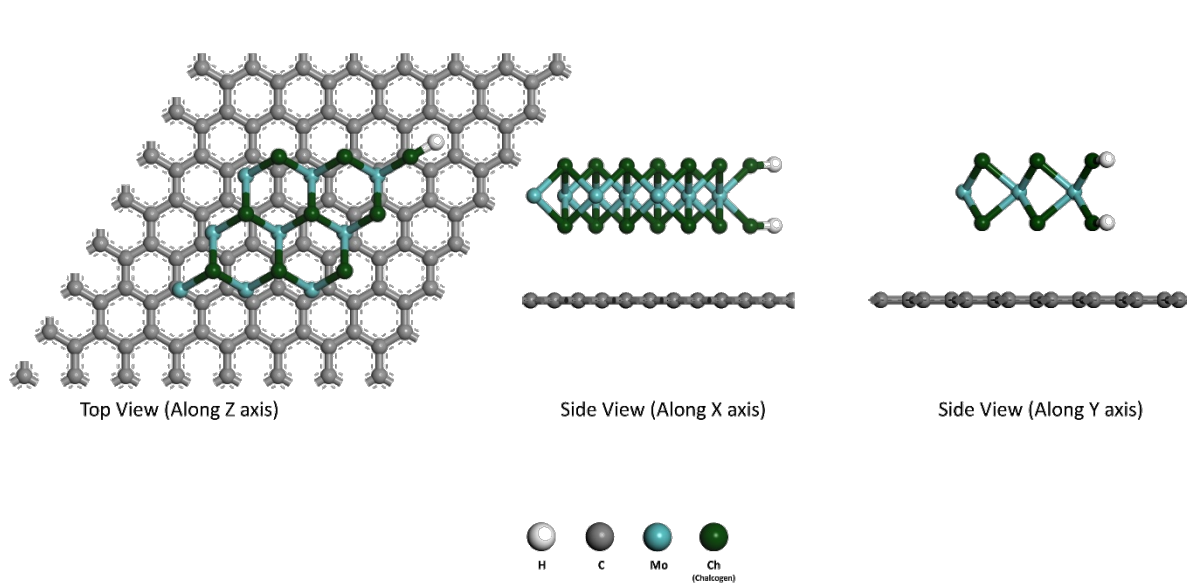
Figure 4.10: Multiview orthographic projection of adsorption site: chalcogen corner (site index no. 9).
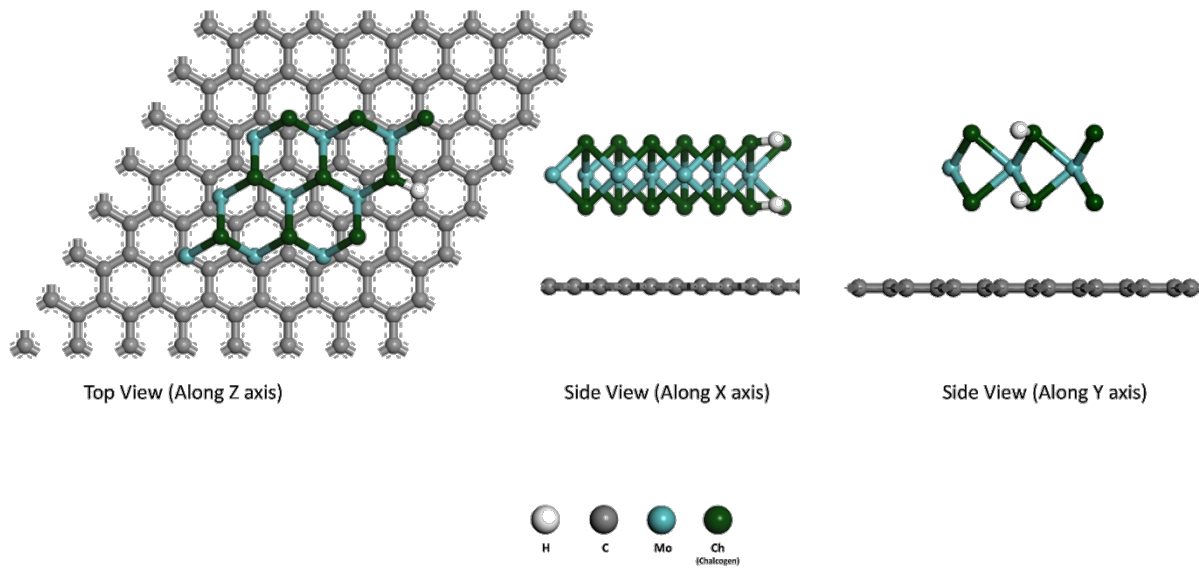
Figure 4.11: Multiview orthographic projection of adsorption site: up-and-down chalcogen edge 1 (site index no. 10).
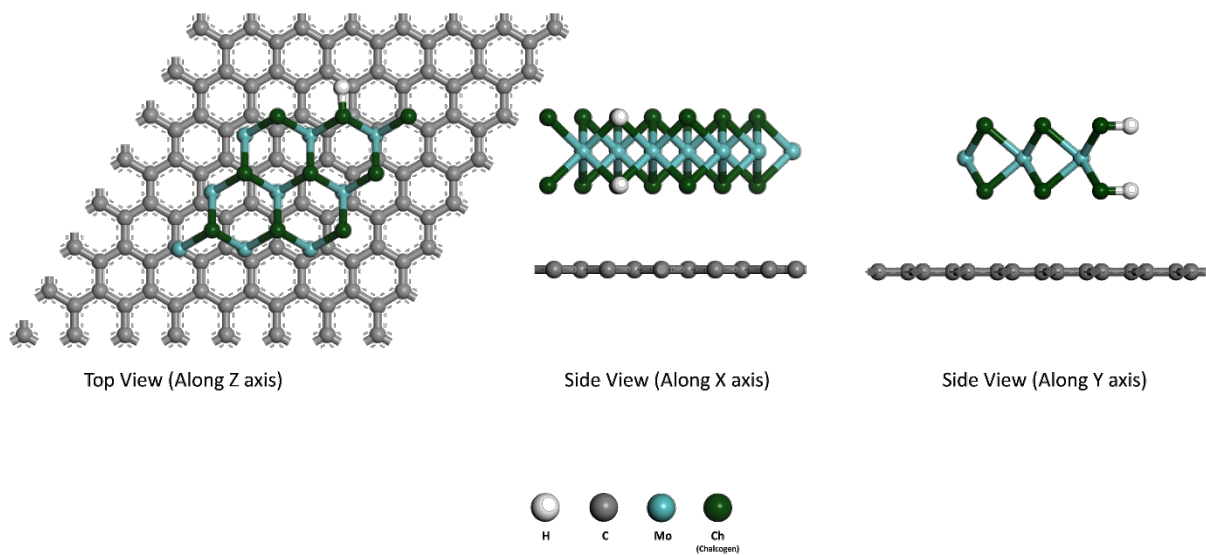
Figure 4.12: Multiview orthographic projection of adsorption site: up-and-down chalcogen edge 2 (site index no. 11).
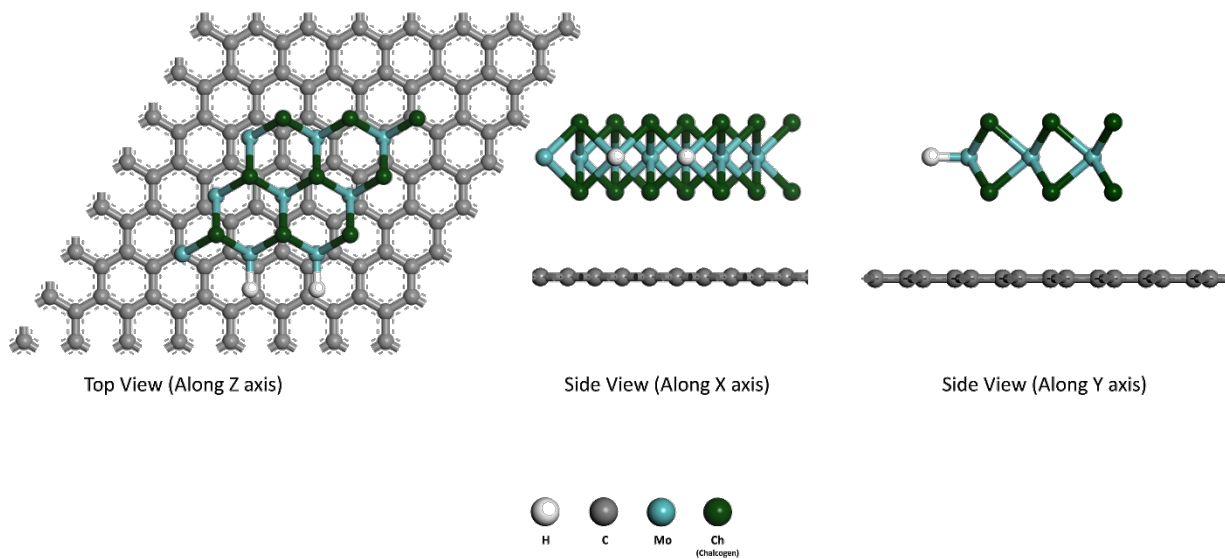
Figure 4.13: Multiview orthographic projection of adsorption site: Mo edge 1 (site index no. 12).

Top View (Along Z axis)   Side View (Along X axis)   Side View (Along Y axis)

H   C   Mo   Ch
(Chalcogen)
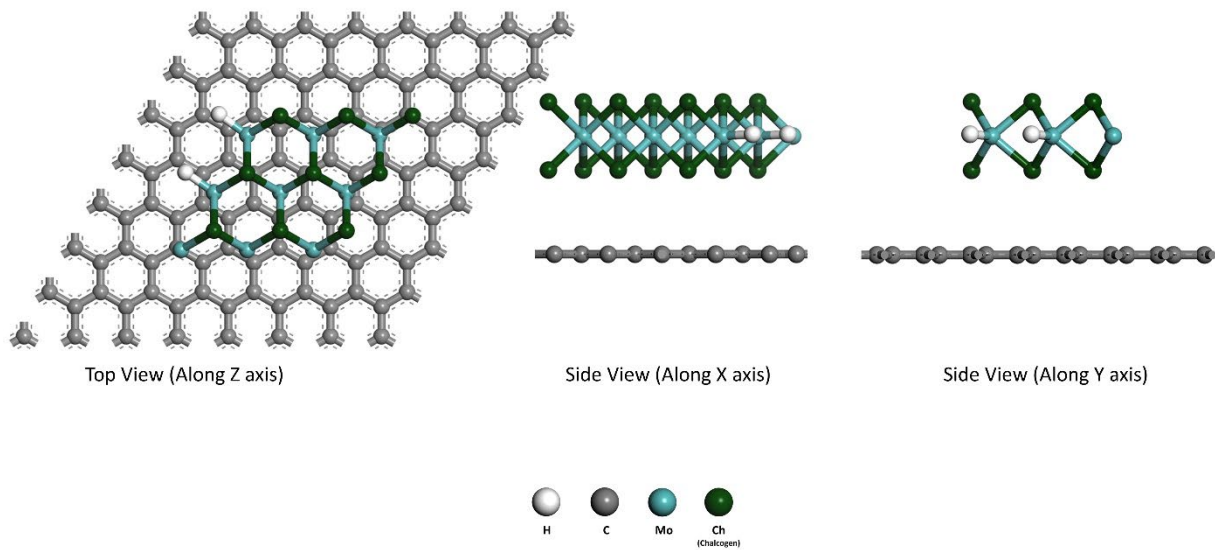
Figure 4.14: Multiview orthographic projection of adsorption site: Mo edge 2 (site index no. 13).

Top View (Along Z axis)   Side View (Along X axis)   Side View (Along Y axis)

H   C   Mo   Ch
(Chalcogen)
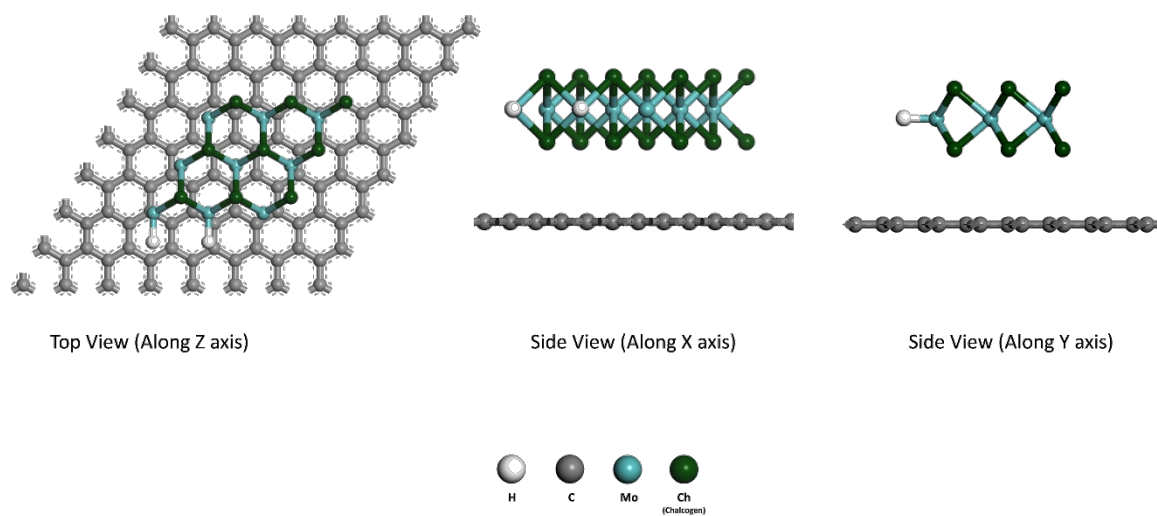
Figure 4.15: Multiview orthographic projection of adsorption site: Mo corner & Mo edge (site index no. 14).

For the computational study, multiple hydrogen adsorption sites on each of the molybdenum dichalcogenide/graphene nanocomposites were investigated for binding energetics. For each of these sites, the effective binding electronic energy for a single hydrogen atom on the nanoparticle supported by the graphene, has been calculated using the following equation:

$$\Delta E_b = \frac{1}{2}(E_{2H^*+Nanocomposite} - E_{Nanocomposite} - E_{H_2}) \qquad \text{………………...……} (1)$$

Here $E_{2H^*+Nanocomposite}$ is the total electronic energy of the two hydrogen atoms bound to the nanoparticle-graphene composite, $E_{Nanocomposite}$ is the total electronic energy of only the nanoparticle-graphene composite, and E_{H_2} is the electronic energy of a hydrogen molecule placed in a 17.2Å×17.2Å×20Å vacuum hexagonal unit cell. Binding free energy (ΔG_b), which is a more appropriate descriptor for the catalytic activity than electronic energy alone, has been calculated using the generalized expression for HER catalysis developed by Nørskov and coworkers in the following equation[110]:

$$\Delta G_b = \Delta E_b + 0.24 \ eV \qquad \text{………………………………………...……………} (2)$$

4.3. Results and Discussion:

For the computational study, multiple hydrogen adsorption sites on each molybdenum dichalcogenide/graphene (MoCh$_2$/Gr) nanocomposite were investigated for binding energetics for hydrogen adsorption. Adsorbed hydrogen (H*) is the common intermediate state in all three steps of HER: Volmer, Heyrovsky, and Tafel.[187] The binding energetics of H* is considered as one of the most important descriptors of potential hydrogen evolution catalysts with the assumption of Brønsted-Evans-Polanyi (BEP) linear correlations between reaction energy and the activation energy of an elementary reaction.[188–190]

Table 4.3. Theoretically calculated binding energies (ΔE_b and ΔG_b) of hydrogen atoms on various adsorption sites of non-hybrid molybdenum dichalcogenide/graphene nanocomposite.

Binding Sites Index	Binding Sites	Ch=S		Ch=Se		Ch=Te	
		ΔE_b (eV)	ΔG_b (eV)	ΔE_b (eV)	ΔG_b (eV)	ΔE_b (eV)	ΔG_b (eV)
1	Ch Edge (Side-by-side)	-0.902	-0.662	0.376	0.616	1.248	1.488
2	Mo Corner	-0.623	-0.383	-0.576	-0.336	-0.488	-0.248
3	Ch Top	-2.060	-1.820	0.658	0.898	1.083	1.323
4	Ch-Mo Edge (Bridge)	0.429	0.669	-0.269	-0.029	-0.153	0.087
5	Ch Edge-Mo Corner	-0.221	0.019	0.281	0.521	0.140	0.380
6	Ch Corner	-1.770	-1.530	0.011	0.251	0.818	1.058
7	Ch Edge (Up-and-down)	-1.468	-1.228	0.284	0.524	0.584	0.824
8	Mo Edge	-0.487	-0.247	-0.550	-0.310	0.186	0.426
9	Mo corner-Mo Edge	-0.469	-0.229	-0.825	-0.585	0.034	0.274

Table 4.4. Theoretically calculated binding energies (ΔE_b and ΔG_b) of hydrogen atoms on various adsorption sites of hybrid molybdenum dichalcogenide/graphene nanocomposite.

Binding Site Index	Binding Sites	Mo$_9$S$_9$Se$_9$/Gr		Mo$_9$S$_9$Te$_9$/Gr		Mo$_9$Se$_9$Te$_9$/Gr		Mo$_9$S$_6$Se$_6$Te$_6$/Gr	
		ΔE_b (eV)	ΔG_b (eV)	ΔE_b (eV)	ΔG_b (eV)	ΔE_b (eV)	ΔG_b (eV)	ΔE_b (eV)	ΔG_b (eV)
1	Chalcogen Edge (Side-by-side 1)	-1.515 (S & Se)	-1.275	0.374 (Te & S)	0.614	0.528 (Te & Se)	0.768	0.420 (Se & Te)	0.660
2	Chalcogen Edge (Side-by-side 2)	-1.845 (Se & S)	-1.605	0.367 (S & Te)	0.607	0.394 (Se & Te)	0.634	0.430 (Te & Se)	0.670
3	Mo Corner	-0.909	-0.669	-0.567	-0.327	-0.454	-0.214	-0.613	-0.373
4	Chalcogen Top 1	-0.141 (Only Se)	0.099	0.849	1.089	0.793	1.033	0.395	0.635
5	Chalcogen Top 2	0.368 (S & Se)	0.608	0.645	0.885	1.138	1.378	0.504	0.744
6	Ch-Mo Edge (Bridge 1)	-2.605 (Ch = S)	-2.365	-0.280 (Ch = S)	-0.040	0.307 (Ch = Se)	0.547	-0.384 (Ch = Te)	-0.144
7	Ch-Mo Edge (Bridge 2)	1.472 (Ch = Se)	1.712	0.188 (Ch = Te)	0.428	0.150 (Ch = Te)	0.390	-0.435 (Ch = Se)	-0.195
8	Mo Corner-Ch Edge	0.266	0.506	0.439	0.679	0.178	0.418	-0.009	0.231
9	Chalcogen Corner	-0.835 (S & Se)	-0.595	0.179	0.419	0.188	0.428	-0.070 (S & Se)	0.170
10	Chalcogen Edge (Up-and-down 1)	-1.321 (S & Se)	-1.081	0.158 (S & Te)	0.398	0.560 (Se & Te)	0.800	0.395 (Te & Se)	0.635
11	Chalcogen Edge (Up-and-down 2)	-1.439 (Se & S)	-1.199	0.183 (Te & S)	0.423	0.421 (Te & Se)	0.661	0.414 (Se & S)	0.654
12	Mo Edge 1	-1.265	-1.025	-0.470	-0.230	-0.443	-0.203	0.232	0.472
13	Mo Edge 2	-2.548	-2.308	-0.084	0.156	-0.395	-0.155	-0.414	-0.174
14	Mo Corner & Edge	-0.824	-0.584	-0.853	-0.613	-0.770	-0.530	-0.919	-0.679

The overall binding electronic energy values for all of the nanocomposites varies from -2.605 eV to 1.472 eV with a standard deviation of 0.814 eV, and the binding free energy values vary from -2.365 eV to 1.712 eV with a standard deviation of 0.814 eV. There are eleven binding sites among these seven studied nanocomposites found between the free energy of binding range of -0.02 eV and 0.02 eV. The two structures that contain the highest standard deviations among its binding energies are Mo_9S_{18}/Gr and $Mo_9S_9Se_9/Gr$ (0.849 eV and 1.166 eV, respectively). Among all of the other structures binding free energies have standard deviation of approximately 0.5 eV.

For the Mo_9S_{18}/Gr nanocomposite structure, the binding electronic energy values range from -2.060 eV to 0.429 eV, and the binding free energy values range from the -1.820 eV to 0.669 eV (Figure 4.16 and Table 4.3, respectively). The site consisting of a Mo corner and S edge (Figure 4.16) exhibits the most thermoneutral free energy change (-0.018 eV), i.e., the lowest absolute value of binding free energy ($|\Delta G_{Binding}|$).
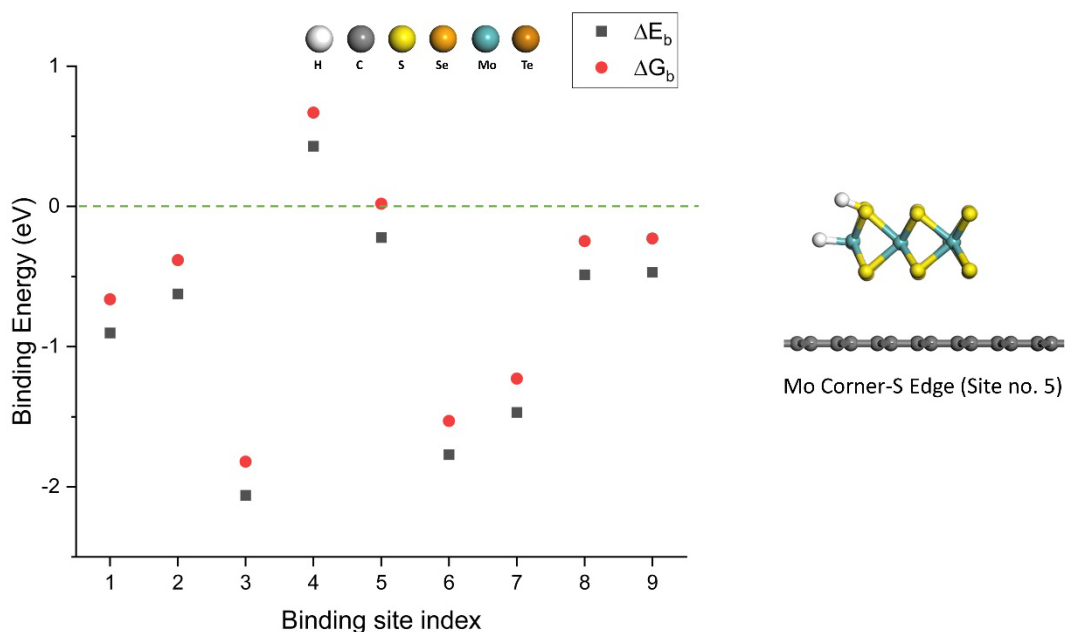
Figure 4.16: Calculated free energy of binding (ΔG_b: denoted with red circles) and binding electronic energy (ΔE_b: denoted with black squares) values at different binding sites of the Mo_9S_{18}/Gr nanocomposite structure. The binding site indexing is as follows: (1) Sulfur edge (side-by-side), (2) Mo corner, (3) S top, (4) Mo edge-S edge, (5) Mo Corner-S Edge, (6) S corner, and (7) S edge (up-and-down), (8) Mo edge, and (9) Mo corner and edge.

For the nanocomposite Mo_9Se_{18}/Gr, the resultant binding electronic energy values range from -0.825 eV to 0.658 eV, and the range of binding free energy values is from -0.585 eV to 0.898 eV (Figure 4.17 and Table 4.3). For the Mo_9Se_{18}/Gr structure, the adsorption site having the near zero binding free energy value ($\Delta G_b \approx 0$) is the Mo edge and Se edge (ΔG_b = -0.029 eV).
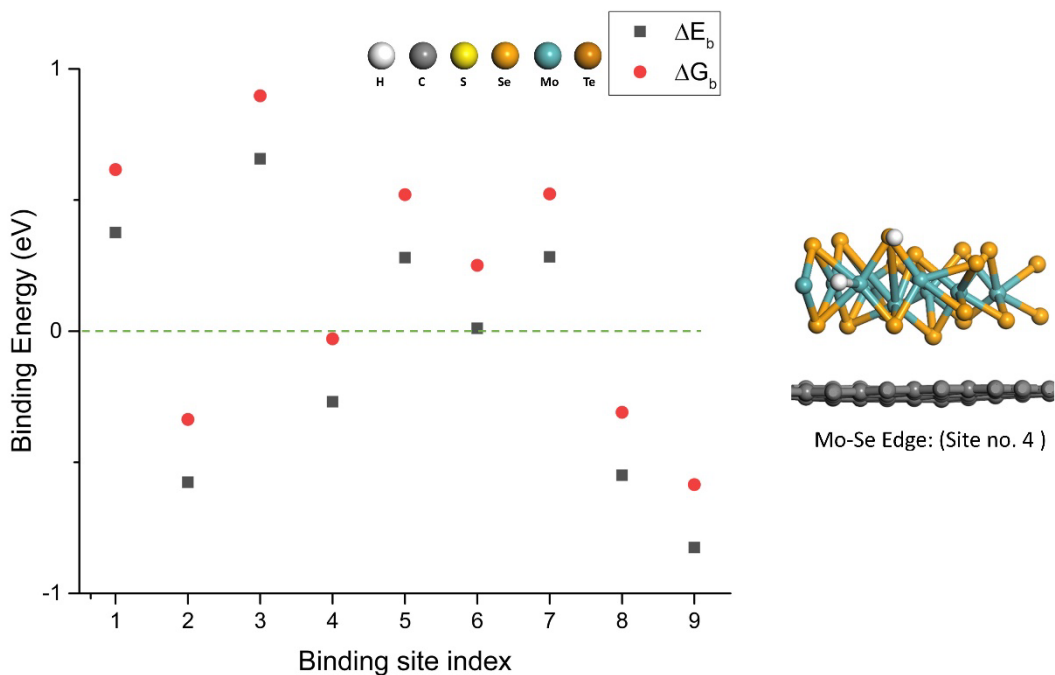
Figure 4.17: Calculated free energy of binding (ΔG_b: denoted with red circles) and binding electronic energy (ΔE_b: denoted with black squares) values at different binding sites of the Mo_9Se_{18}/Gr nanocomposite structure. The binding site indexing is as follows: (1) Se edge (side-by-side), (2) Mo corner, (3) Se top, (4) Mo edge-Se edge, (5) Mo Corner-Se Edge, (6) S corner, and (7) Se edge (up-and-down), (8) Mo edge, and (9) Mo corner and edge.

In the case of Mo_9Te_{18}/Gr nanocomposite structures, one site comprised of a Mo edge and Te edge shows a binding free energy value in close proximity to zero ($\Delta G_b = 0.087$ eV). The overall electronic binding energy values varies from -0.527 eV to 1.247 eV, and binding free energy range is from -0.287 eV to 1.487 eV (Figure 4.18 and Table 4.3).

Mo-Te Edge (Site no. 4)
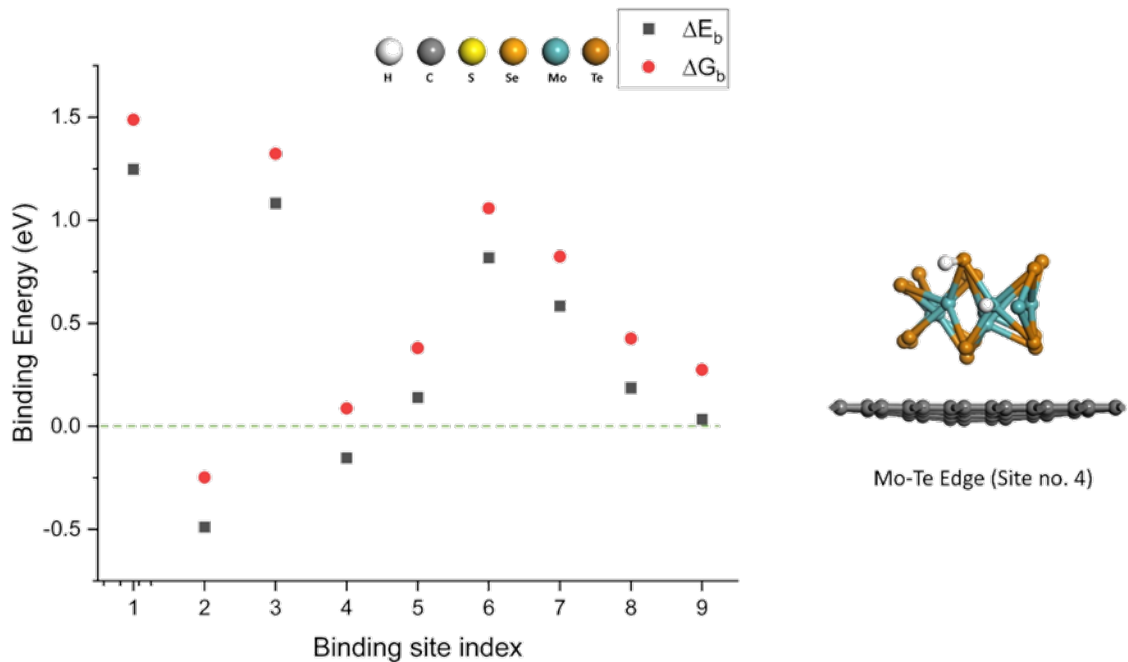
Figure 4.18: Calculated free energy of binding (ΔG_b: denoted with red circles) and binding electronic energy (ΔE_b: denoted with black squares) values at different binding sites of the Mo_9Te_{18}/Gr nanocomposite structure. The binding site indexing is as follows: (1) Te edge (side-by-side), (2) Mo corner, (3) Te top, (4) Mo edge-Te edge, (5) Mo Corner-Te Edge, (6) S corner, and (7) Te edge (up-and-down), (8) Mo edge, and (9) Mo corner and edge.

For the hybrid nanocomposite Mo₉S₉Se₉/Gr, the binding free energy values vary from -2.365 eV to 1.712 eV, with the chalcogen top surface sites comprised of only Se, exhibiting the best value for catalysis (ΔG_b = 0.099 eV) (Figure 4.19 and Table 4.4).

Chalcogen Top: only Se (Site no. 4)
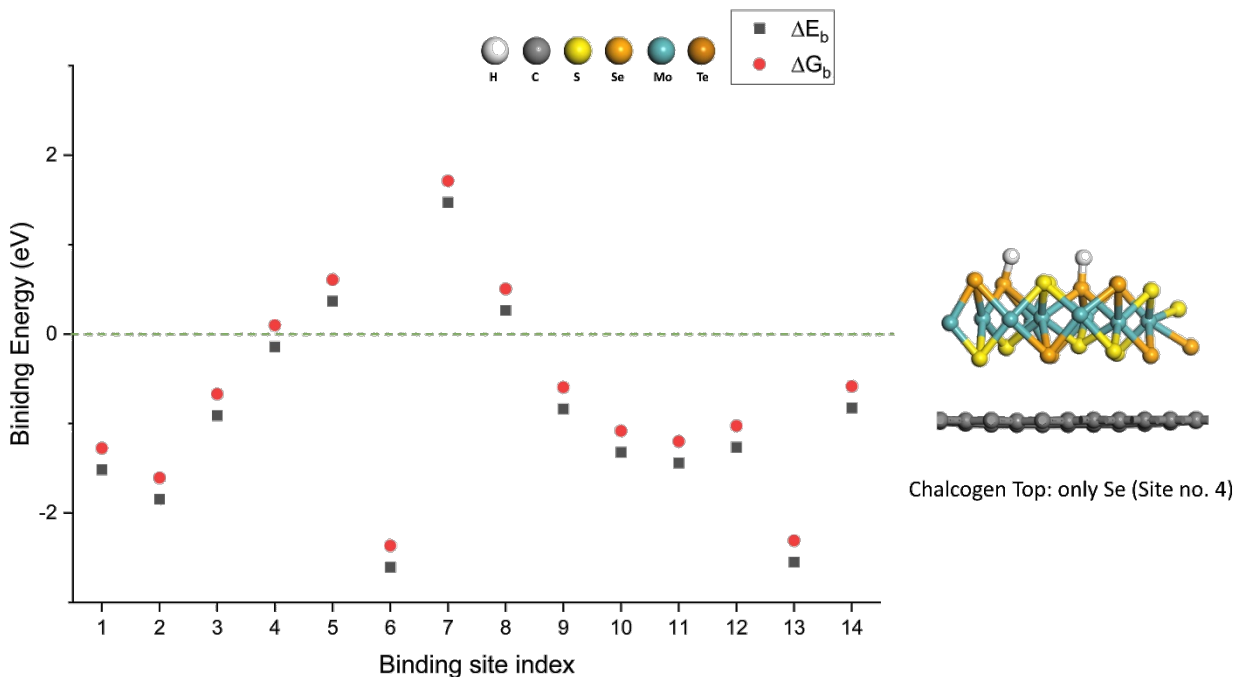
Figure 4.19: Calculated free energy of binding (ΔG_b: denoted with red circles) and binding electronic energy (ΔE_b: denoted with black squares) values at different binding sites of the Mo₉S₉Se₉/Gr nanocomposite structure. The binding site indexing is as follows: (1) chalcogen edge (side-by-side 1), (2) chalcogen edge (side-by-side 2), (3) Mo corner, (4) chalcogen top 1 (only Se), (5) chalcogen top 2 (S & Se), (6) Mo edge-Se edge, (7) Mo edge-S edge, (8) Mo Corner-T Edge, (9) chalcogen corner, and (10) chalcogen edge (up-and-down 1), (11) chalcogen edge (up-and-down 2), (12) Mo edge 1, (13) Mo edge 2, and (14) Mo corner and edge.

For the nanocomposite $Mo_9S_9Te_9$/Gr, the resultant binding electronic energy values range from -0.853 eV to 0.849 eV, and the range of binding free energy values is from -0.613 eV to 1.089 eV (Figure 4.20 and Table 4.4). Two adsorption sites are found to have thermoneutral energetics, the bridge site between S edge and Mo edge (ΔG_b = -0.040 eV) and the Mo edge 2 site (ΔG_b = 0.156).
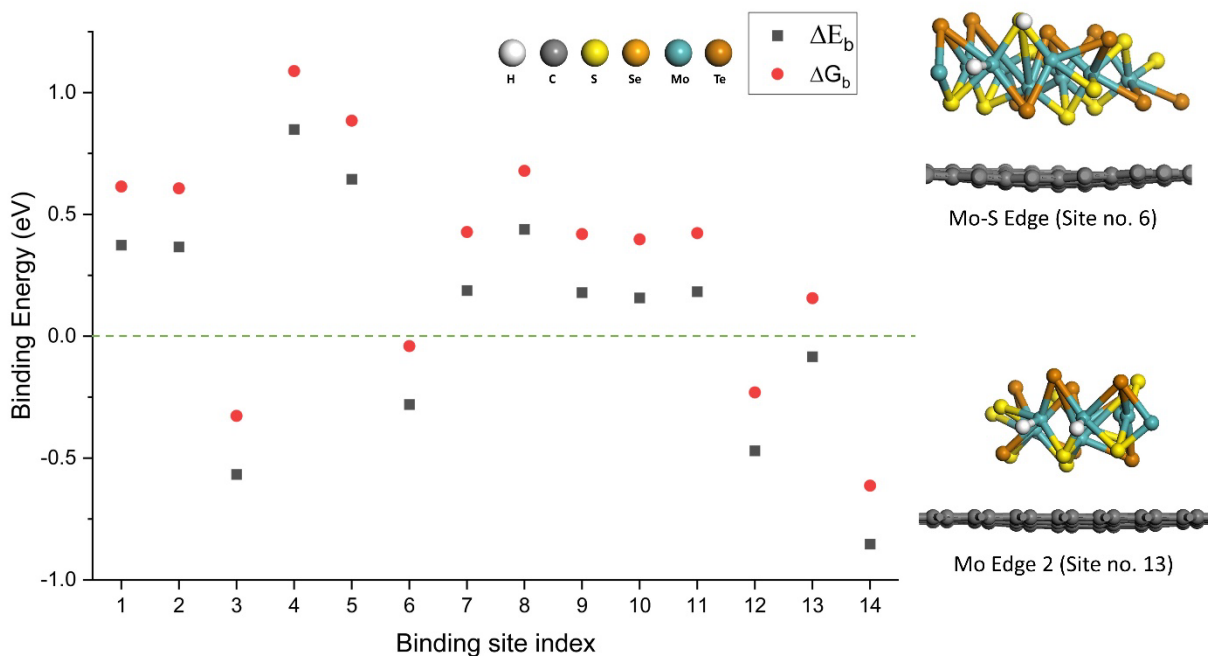
Figure 4.20: Calculated free energy of binding (ΔG_b: denoted with red circles) and binding electronic energy (ΔE_b: denoted with black squares) values at different binding sites of the $Mo_9S_9Te_9$/Gr nanocomposite structure. The binding site indexing is as follows: (1) chalcogen edge (side-by-side 1), (2) chalcogen edge (side-by-side 2), (3) Mo corner, (4) chalcogen top 1 (only Te), (5) chalcogen top 2 (S & Te), (6) Mo edge-S edge, (7) Mo edge-Te edge, (8) Mo Corner-Te Edge, (9) chalcogen corner, and (10) chalcogen edge (up-and-down 1), (11) chalcogen edge (up-and-down 2), (12) Mo edge 1, (13) Mo edge 2, and (14) Mo corner and edge.

For the hybrid nanocomposite $Mo_9Se_9Te_9/Gr$, the binding free energy values vary from -0.530 eV to 1.378 eV (Figure 4.21 and Table 4.4). The Mo edge 2 site (site no. 13) exhibits the nearest to zero value (ΔG_b = -0.155 eV), but no site in this structure is within the range of [-0.1 eV, 0.1 eV].
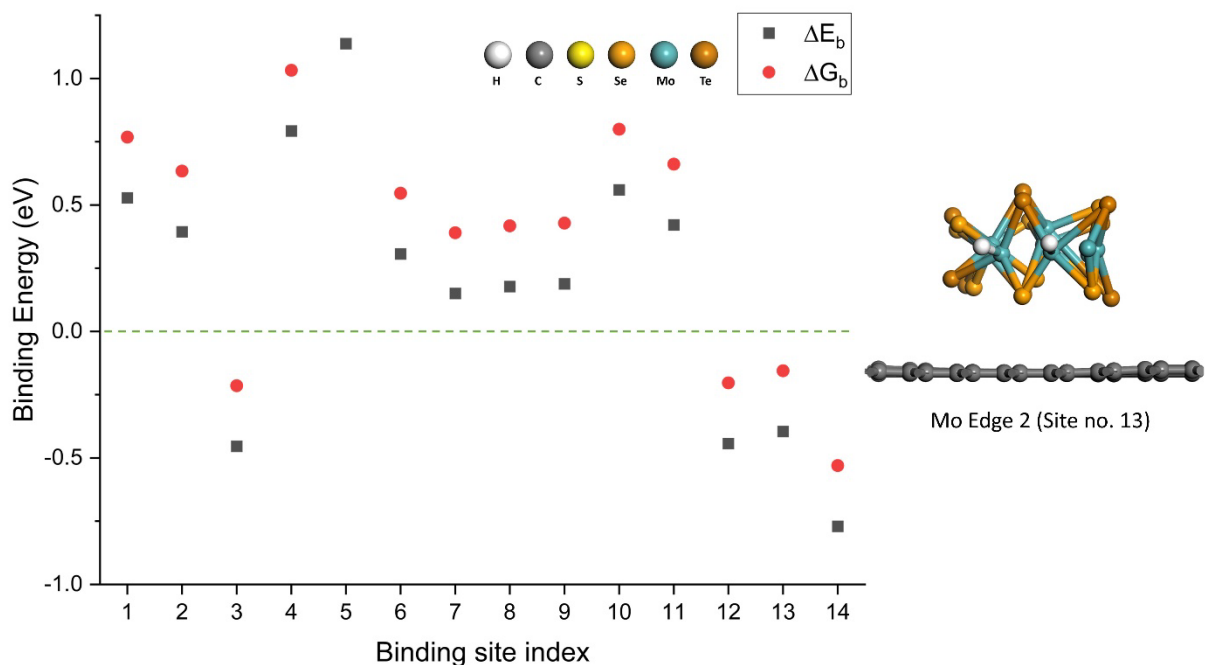
Figure 4.21: Calculated free energy of binding (ΔG_b: denoted with red circles) and binding electronic energy (ΔE_b: denoted with black squares) values at different binding sites of the $Mo_9Se_9Te_9/Gr$ nanocomposite structure. The binding site indexing is as follows: (1) chalcogen edge (side-by-side 1), (2) chalcogen edge (side-by-side 2), (3) Mo corner, (4) chalcogen top 1 (only Te), (5) chalcogen top 2 (Se & Te), (6) Mo edge-Se edge, (7) Mo edge-Te edge, (8) Mo Corner-Te Edge, (9) chalcogen corner, and (10) chalcogen edge (up-and-down 1), (11) chalcogen edge (up-and-down 2), (12) Mo edge 1, (13) Mo edge 2, and (14) Mo corner and edge.

Results for $Mo_9S_6Se_6Te_6$/Gr nanocomposite shows four sites having binding free energy within the range of [-0.2 eV, 0.2 eV] but none within the range of [-0.1 eV, 0.1 eV] (Figure 4.22 and Table 4.4). Binding free energy values vary from -0.679 eV to 0.744 eV. The four most active sites in this structure are, Mo-Te bridge site (ΔG_b= -0.144 eV), Mo-Se bridge site (ΔG_b= -0.195 eV), S-Se corner site (ΔG_b= 0.170 eV), and Mo edge 2 site (ΔG_b= -0.174 eV).
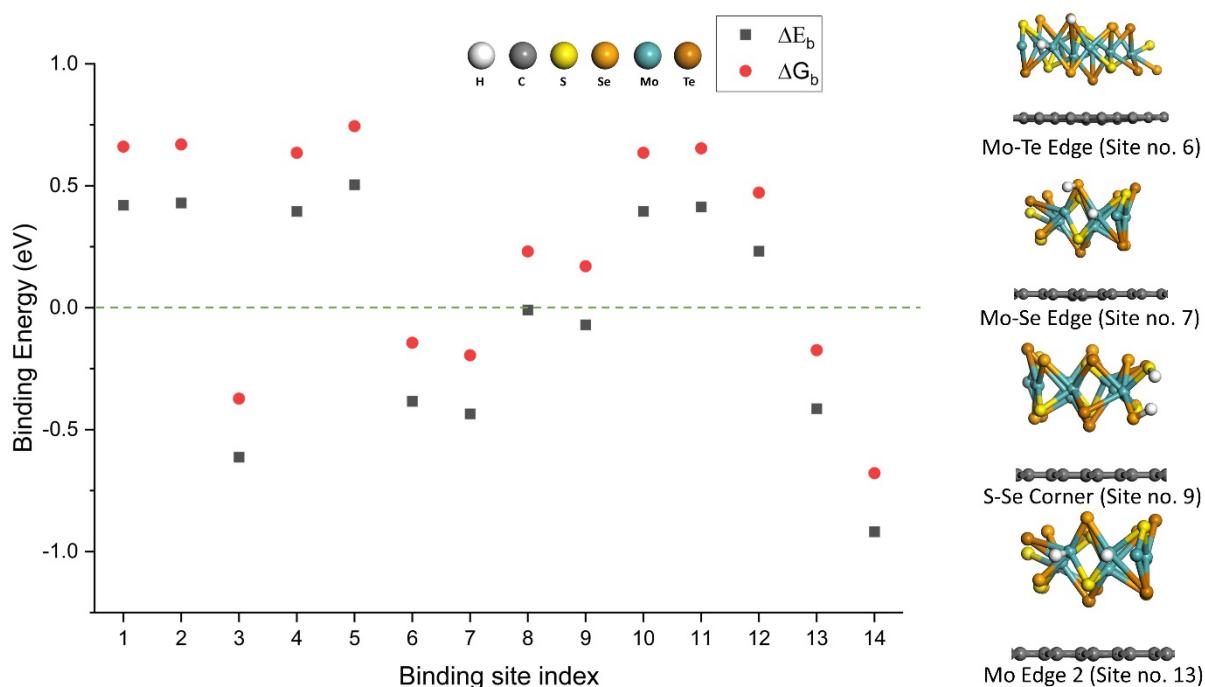
Figure 4.22: Calculated free energy of binding (ΔG_b: denoted with red circles) and binding electronic energy (ΔE_b: denoted with black squares) values at different binding sites of the $Mo_9S_6Se_6Te_6$/Gr nanocomposite structure. The binding site indexing is as follows: (1) chalcogen edge (side-by-side 1: Se & Te), (2) chalcogen edge (side-by-side 2: Te & Se), (3) Mo corner, (4) chalcogen top 1 (S & Te), (5) chalcogen top 2 (S & Se), (6) Mo edge-Te edge, (7) Mo edge-Se edge, (8) Mo Corner-S Edge, (9) chalcogen corner (S & Se), and

(10) chalcogen edge (up-and-down 1: Te & Se), (11) chalcogen edge (up-and-down 2: Se & S), (12) Mo edge 1, (13) Mo edge 2, and (14) Mo corner and edge.

Conventionally, the binding free energies for high-performing catalytically active sites are considered within the range of -0.2 eV and 0.2 eV. Each of the composite systems which have been considered in this computational investigation possess binding sites within this range (Figure 4.23 a). However, the $Mo_9Se_9Te_9/Gr$ and $Mo_9S_6Se_6Te_6/Gr$ nanocomposites do not have any sites within the narrower thermoneutral range of [-0.1 eV, 0.1 eV] (Table 4.4).
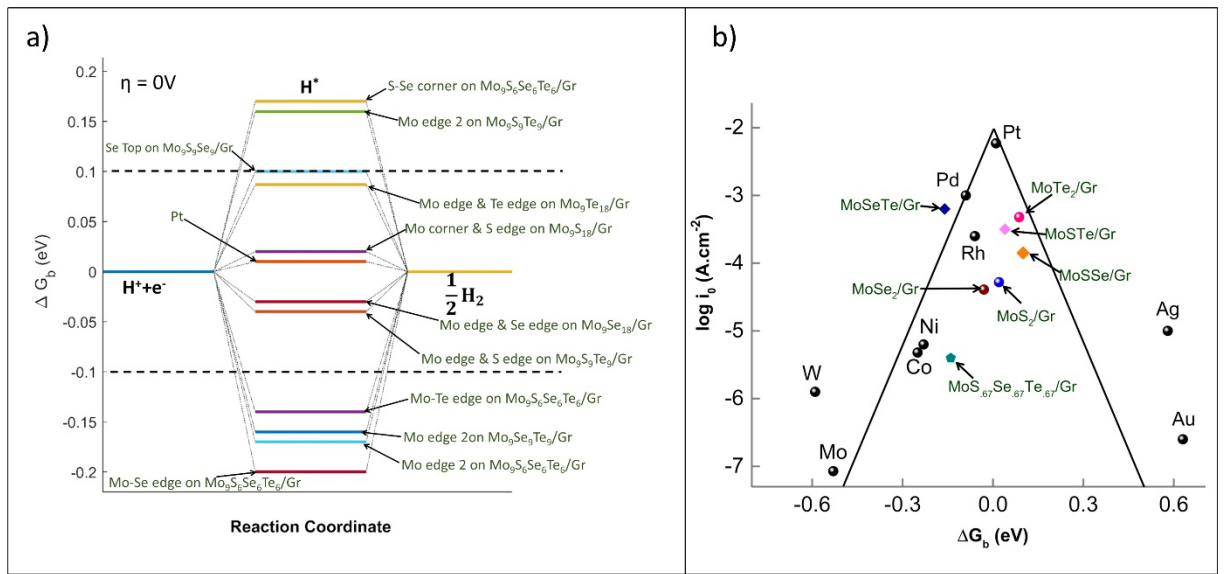
Figure 4.23: **(a)** Free energy diagram for effective hydrogen atom binding at equilibrium (η = 0 V). Value of the binding free energy of Pt is taken from literature.[146] **(b)** Volcano plot of experimentally measured current density (i_0) vs. DFT-calculated Gibbs free energy of hydrogen binding (ΔG_b). With the exception of the $MoCh_2/Gr$ systems, all presented data values are from literature sources.[110,145,146]

Notably, among all the sites within the range of [-0.2 eV, 0.2 eV], most of the sites are comprised of at least one Mo atom (i.e., nine among eleven binding sites in Figure 4.23 a). Both of these Mo-excluding sites contain Se. The nanocomposite that exhibits binding free energy values in the closest proximity to zero ($|\Delta G_b| \leq 0.05$ eV) are MoS_2/Gr, $MoSe_2$/Gr, and MoSTe/Gr. The band gap difference of monolayer $MoTe_2$ (2.1 eV) from MoS_2 and $MoSe_2$ (2.58 eV & 2.55 eV, respectively) indicates that the presence of Te in the $MoCh_2$/Gr nanocomposite can increase the conductivity, thus accommodating better electrocatalytic activity.[118,191] Moreover, the lower value of electronegativity of Te (2.10) compared to S, Se and even Mo (2.58, 2.55, and 2.16, respectively), suggests a shift in electron density in the nanoparticle from Te to the other adjacent atoms in the nanocomposite which facilitates optimal hydrogen binding.[192]

With regard to the concept of optimal binding, our studies further investigated the role of partial atomic charge through Mulliken population analysis. The partial charge analysis revealed that the optimal hydrogen binding sites in the range of -0.1 eV to +0.1 eV were a result of heterolytic associative desorption, whereas the next nearest optimal hydrogen binding sites in the range of -0.2 eV to +0.2 eV were a result of homolytic associative desorption. The heterolytic sites, for instance sites comprised of Mo and S, possessed two dissociated hydrogen atoms with opposing partial charge, one positively charged and one negatively charged. The charge separation between neighboring hydrogens ultimately proves to be beneficial for near thermoneutral binding free energy of molecular hydrogen. The homolytic sites, for instance Mo and Mo, possessed two dissociated hydrogen atoms with partial negative charges on average, which ultimately leads to a higher free energy

barrier to associative desorption of molecular hydrogen for cathodic hydrogen generation processes than for heterolytic sites. Both Se and S when coupled to Mo on a binary active site will exhibit a heterolytic associative desorption mechanism, whereas Te when coupled to Mo on a binary active site will exhibit a homolytic associative desorption mechanism on average similar to sites comprised of only Mo atoms.

The experimental electrocatalytic HER activities of the synthesized catalyst samples were investigated by Linear Sweep Voltammetry (LSV) measurements in a 0.5 M H_2SO_4 electrolyte. For nanocomposites of non-hybrid molybdenum dichalcogenide nanoparticles and graphene, the order of HER activity based on η (overpotential at -10 mA.cm^{-2}) is found to be MoTe$_2$/Gr > MoS$_2$/Gr > MoSe$_2$/Gr (Figure 4.24). It clearly indicates that the higher electrical conductivity of MoTe$_2$ facilitates a faster electron transfer process.[118,193,194] Furthermore, the Tafel diagrams were derived from LSVs by fitting the linear sections to the Tafel equation (η = b×log i + a), where η is overpotential, b is Tafel slope, i represents the cathodic current density, and a is the Tafel constant.[187] In general, the HER takes place through two consecutive steps: an adsorption step (Volmer, $H^+ + e^- \rightarrow H_{ads}$, 120 mV dec^{-1}), followed by a reduction step (Heyrovsky, $H^+ + H_{ads} + e^- \rightarrow H_2$, 40 mV dec^{-1} or Tafel, $2H_{ads} \rightarrow H_2$, 30 mV dec^{-1}).[187] The Tafel slope identifies the required overpotential to increase the reaction rate by a factor of ten; therefore, it is noticeable that the smaller Tafel slope favors HER activities. From Figure 4.24, although MoTe$_2$/Gr shows the smallest overpotential, a higher Tafel slope of 49.8 mV dec^{-1} is shown in comparison with other non-hybrid samples (38.5 mV dec^{-1} for MoS$_2$/Gr and 44.3 mV dec^{-1} for MoSe$_2$/Gr).

The HER activities of hybrid nanocomposites of MoXY/Gr (X, Y = S and/or Se and/or Te) and $MoS_{0.67}Se_{0.67}Te_{0.67}$/Gr were further compared. Based on the overpotential values, the order of HER performance is revealed as MoSTe/Gr > MoSeTe/Gr > MoSSe/Gr > $MoS_{0.67}Se_{0.67}Te_{0.67}$/Gr, which clearly indicates the presence of Te improves the electron transfer rate due to its higher electrical conductivity. It is worth noting that, despite the presence of Te in $MoTe_2$/Gr, the HER performance of MoSTe/Gr is much better than $MoTe_2$/Gr. This improved performance of MoSTe/Gr can result from synergistic effects of sulfide and telluride. In addition, by doping S into the $MoTe_2$/Gr structure, more of the inactive oxides can be replaced by sulfides, which can be observed in the XPS results. The data from XPS result show that the MoSTe/Gr contains much less O (at.% 3.10) compared to the O content (at.% 9.82) of $MoTe_2$/Gr. For $MoS_{0.67}Se_{0.67}Te_{0.67}$/Gr, although it consists of all the chalcogen atoms (S, Se, and Te), the HER performance is poor. Further studies are required to understand the reason behind this poor electrocatalytic performance of the highest entropy alloy. However, it generally has been shown that high entropy alloys in catalysis exhibit sluggish surface diffusion rates, which could be the root cause of this observed poor HER performance.[195] Based on the LSV curves, the Tafel analysis was performed. As shown in Figure 4.24, MoSTe/Gr exhibited the lowest Tafel slope of 39.2 mV dec^{-1}, which is also very close to the value of commercial 10 wt.% Pt/C catalyst (30.0 mV dec^{-1}).

Figure 4.24: Bar graphs displaying the three major parameters (overpotential, Tafel slope, and exchange current density) of molybdenum dichalcogenide HER catalysts.

Moreover, all these hybrid and non-hybrid catalysts revealed very good stability performance for 96 h of constant potential test at an overpotential of 250 mV without any significant structural failure. Among non-hybrid nanocomposites, MoTe₂/Gr shows the best stability results maintaining the highest current density of around -90 mA cm^{-2}, all the hybrid catalysts showed stable behaviors with slight decrease in HER activities, where the MoSTe/Gr catalyst displayed the highest current density of around -160 mAcm^{-2} which gradually decreased to around -100 mA cm^{-2} after 96 h test. Among the hybrid MoXY/Gr catalysts, MoSTe/Gr exhibited the best stability performance in terms of retaining the highest current density. These remarkable stability results can be attributed to the compositional and structural stabilities of nanosheet structures of molybdenum dichalcogenides supported by strong graphene network. However, it is worth noting that

the stability performance of non-hybrid MoCh$_2$/Gr samples are inferior to the hybrid MoXY/Gr samples. This clearly indicates the doping and hybridization of metal dichalcogenides help to improve the structural integrity during the long-term HER performance.[169,170]

Furthermore, all the significant parameters (overpotential, Tafel slope, and exchange current density) for the electrocatalytic performance of synthesized nanocomposites for HER are summarized in Figure 4.24. Although the chemical formula appears to be similar for all the molybdenum dichalcogenides, each sample is slightly different structurally from each other. These structural differences give rise to variations in their electrical transport properties.[196] An important feature of tellurides that distinguishes the structure from sulfides and selenides is the large atomic number of Te and low electronegativity (2.10), allowing for a distinguished crystal structure, electronic configuration, and physicochemical properties.[196] Therefore, the catalyst samples containing Te, except for the highest-entropy alloy MoS$_{0.67}$Se$_{0.67}$Te$_{0.67}$/Gr, showed very promising HER activities to generate hydrogen from water splitting.

The electrocatalytic HER activities of the synthesized catalyst samples were investigated by Linear Sweep Voltammetry (LSV) measurements in a 0.5 M H$_2$SO$_4$ electrolyte. For nanocomposites of non-hybrid molybdenum dichalcogenide nanoparticles and graphene, the order of HER activity based on η (overpotential at -10 mA.cm^{-2}) is found to be MoTe$_2$/Gr > MoS$_2$/Gr > MoSe$_2$/Gr (Figure 4.24). It clearly indicates that the higher electrical conductivity of MoTe$_2$ facilitates a faster electron transfer process.[118,193,194] Furthermore, the Tafel diagrams were derived from LSVs by fitting the linear sections to the Tafel equation (η = b×log i + a), where η is overpotential, b is Tafel slope, i represents

the cathodic current density, and a is the Tafel constant.[187] In general, the HER takes place

through two consecutive steps: an adsorption step (Volmer, $H^+ + e^- \rightarrow H_{ads}$, 120 mV

dec^{-1}), followed by a reduction step (Heyrovsky, $H^+ + H_{ads} + e^- \rightarrow H_2$, 40 mV dec^{-1} or

Tafel, $2H_{ads} \rightarrow H_2$, 30 mV dec^{-1}).[187] The Tafel slope identifies the required overpotential

to increase the reaction rate by a factor of ten; therefore, it is noticeable that the smaller

Tafel slope favors HER activities. Although MoTe$_2$/Gr shows the smallest overpotential, a

higher Tafel slope of 49.8 mV dec^{-1} is shown in comparison with other non-hybrid samples

(38.5 mV dec^{-1} for MoS$_2$/Gr and 44.3 mV dec^{-1} for MoSe$_2$/Gr).

The HER activities of hybrid nanocomposites of MoXY/Gr (X, Y = S and/or Se and/or Te)

and MoS$_{0.67}$Se$_{0.67}$Te$_{0.67}$/Gr were further compared. Based on the overpotential values, the

order of HER performance is revealed as MoSTe/Gr > MoSeTe/Gr > MoSSe/Gr >

MoS$_{0.67}$Se$_{0.67}$Te$_{0.67}$/Gr, which clearly indicates the presence of Te improves the electron

transfer rate due to its higher electrical conductivity. It is worth noting that, despite the

presence of Te in MoTe$_2$/Gr, the HER performance of MoSTe/Gr is much better than

MoTe$_2$/Gr. This improved performance of MoSTe/Gr can result from synergistic effects of

sulfide and telluride. In addition, by doping S into the MoTe$_2$/Gr structure, more of the

inactive oxides can be replaced by sulfides, which can be observed in the XPS results. The

data from XPS characterization clearly show that the MoSTe/Gr contains much less O

(at.% 3.10) compared to the O content (at.% 9.82) of MoTe$_2$/Gr. For MoS$_{0.67}$Se$_{0.67}$Te$_{0.67}$/Gr,

although it consists of all the chalcogen atoms (S, Se, and Te), the HER performance is

poor. Further studies are required to understand the reason behind this poor electrocatalytic

performance of the highest entropy alloy. However, it generally has been shown that high

entropy alloys in catalysis exhibit sluggish surface diffusion rates, which could be the root

cause of this observed poor HER performance.[195] Based on the LSV curves, the Tafel analysis was performed. As shown in, MoSTe/Gr exhibited the lowest Tafel slope of 39.2 mV dec^{-1}, which is also very close to the value of commercial 10 wt.% Pt/C catalyst (30.0 mV dec^{-1}).
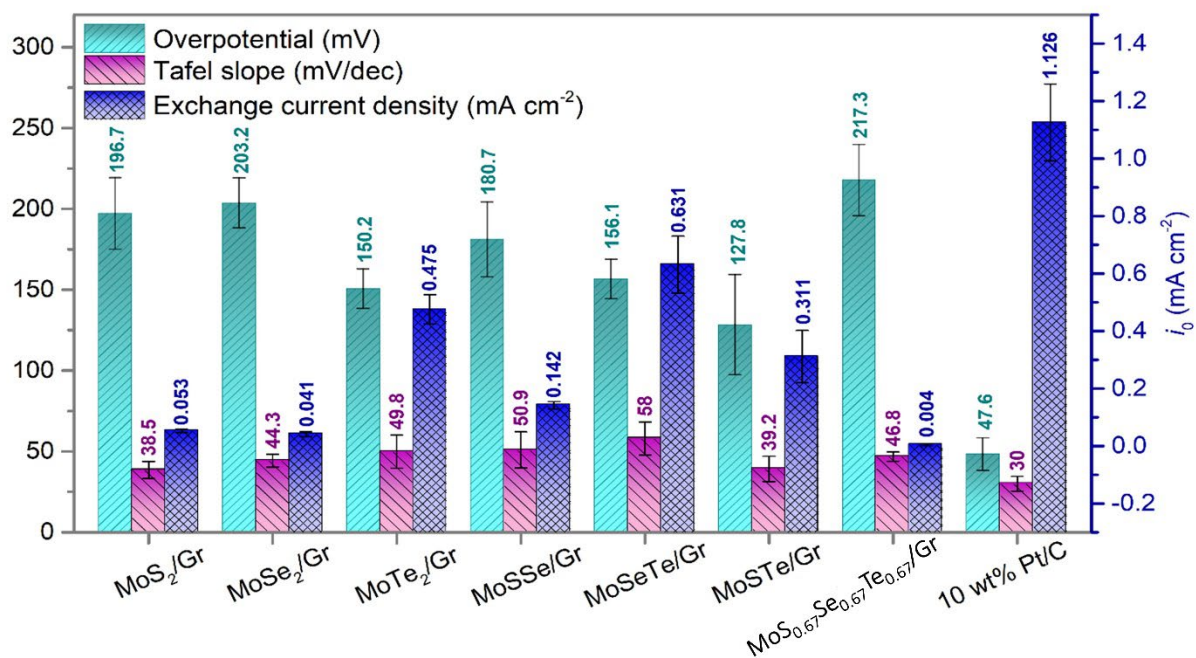
Moreover, all these hybrid and non-hybrid catalysts revealed very good stability performance for 96 h of constant potential test at an overpotential of 250 mV without any significant structural failure. Among non-hybrid nanocomposites, MoTe$_2$/Gr shows the best stability results maintaining the highest current density of around −90 mA cm^{-2}, all the hybrid catalysts showed stable behaviors with slight decrease in HER activities, where the MoSTe/Gr catalyst displayed the highest current density of around -160 mAcm^{-2} which gradually decreased to around −100 mA cm^{-2} after 96 h test. Among the hybrid MoXY/Gr catalysts, MoSTe/Gr exhibited the best stability performance in terms of retaining the highest current density. These remarkable stability results can be attributed to the compositional and structural stabilities of nanosheet structures of molybdenum dichalcogenides supported by strong graphene network. However, it is worth noting that the stability performance of non-hybrid MoCh$_2$/Gr samples are inferior to the hybrid MoXY/Gr samples. This clearly indicates the doping and hybridization of metal dichalcogenides help to improve the structural integrity during the long-term HER performance.[169,170]

Furthermore, all the significant parameters (overpotential, Tafel slope, and exchange current density) for the electrocatalytic performance of synthesized nanocomposites for HER are summarized in **Figure**. Although the chemical formula appears to be similar for

all the molybdenum dichalcogenides, each sample is slightly different structurally from each other. These structural differences give rise to variations in their electrical transport properties.[196] An important feature of tellurides that distinguishes the structure from sulfides and selenides is the large atomic number of Te and low electronegativity (2.10), allowing for a distinguished crystal structure, electronic configuration, and physicochemical properties.[196] Therefore, the catalyst samples containing Te, except for the highest-entropy alloy $MoS_{0.67}Se_{0.67}Te_{0.67}/Gr$, showed very promising HER activities to generate hydrogen from water splitting.

Now taking into account all the descriptors investigated for the four hybrid and three non-hybrid $MoCh_2/Gr$ nanocomposite systems, it is apparent that no nanocomposite system shows optimal results or trending for all the descriptors. That is, the lowest values for $|\Delta G_b|$ and overpotential are observed for MoS_2/Gr, but this nanocomposite also has a very high overpotential and very low current density, which are not ideal for a promising HER electrocatalyst. It should be noted, however, that one descriptor (i.e., ΔG_b, overpotential, current density, etc) appears insufficient to capture the complexity of the HER catalytic processes alone, particularly in higher-entropy alloys and nanocomposites, and multiple descriptors (i.e., activation energies (E_a) for all elementary steps, charge transfer coefficient (α), etc.) may provide deeper insights but that level of study is beyond the scope of this paper. Therefore, combined experimental and computational studies are preferred for studying the efficacy of HER electrocatalysts where multiple descriptors may be collected and analyzed.
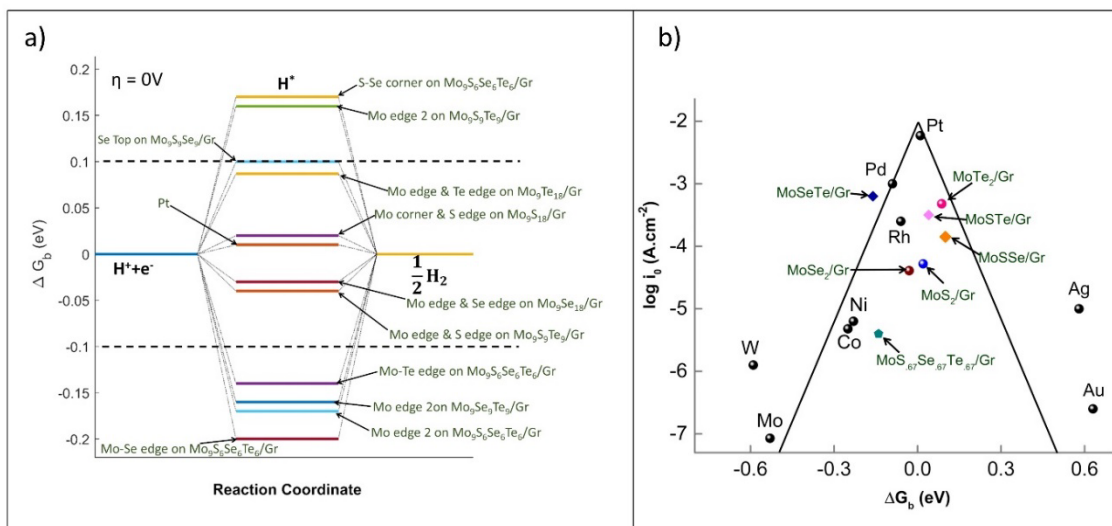
Figure 4.25: . **(a)** Free energy diagram for effective hydrogen atom binding at equilibrium (η = 0 V). Value of the binding free energy of Pt is taken from literature.[146] **(b)** Volcano plot of experimentally measured current density (i_0) vs. DFT-calculated Gibbs free energy of hydrogen binding ($\Delta G_{binding}$). With the exception of the $MoCh_2$/Gr systems, all presented data values are from literature sources.[110,145,146]

Experimentally extrapolated i_0 and theoretically calculated ΔG_b are depicted in a volcano plot to analyze the catalytic performances of the various $MoCh_2$/Gr nanocomposites. It is apparent from **Figure 4.25 b**; that the volcano plot does not capture the full pictures of catalytic activities for our studied $MoCh_2$/Gr nanocomposites. In recent literature, the efficacy of volcano plots to represent the catalytic efficiency has been questioned.[107,183,197,198] From **Figures 4.25**, it is clear that ΔG_b is not directly correlated with exchange current density (i_0). Instead, it shows that Tafel slopes (b) can be better associated with the ΔG_b to rank catalytic efficiency. The properties of current density and

overpotential both are embedded in the definition of Tafel slope. For the three non-hybrid MoCh$_2$/Gr nanocomposites, the value of Tafel slope can be ranked in the same order as their lowest $|\Delta G_b|$. Among the four hybrid MoCh$_2$/Gr, MoSTe/Gr and MoSeTe/Gr nanocomposites have the lowest and the highest value of $|\Delta G_b|$, respectively. Values of their Tafel slope are also in the same order. Though MoSSe/Gr has lower $|\Delta G_b|$ than the MoS$_{0.67}$Se$_{0.67}$Te$_{0.67}$/Gr, it contains only one catalytically active site, whereas the latter has four near thermoneutral binding sites. A recent study shows the Tafel constant (a) of the Tafel equation can be a more suitable descriptor for the HER electrocatalysis.[187] The Tafel constant (a) is mathematically defined as: $a = -b \times \log_{10}(i_0)$. A lower value of Tafel constant is considered as the indicator of good catalyst.

Table 4.5:Tafel constants for hybrid and non-hybrid molybdenum dichalcogenides, and platinum electrode.

Material	Exchange current density (i_0) A.cm^{-2}	Tafel slope (b) V.decade^{-1}	Tafel constant (a) V.decade^{-1}
MoS$_2$/Gr	5.30×10^{-5}	0.0385	0.165
MoSe$_2$/Gr	4.10×10^{-5}	0.0443	0.194
MoTe$_2$/Gr	4.76×10^{-4}	0.0498	0.166
MoSSe/Gr	1.42×10^{-4}	0.0509	0.196
MoSTe/Gr	3.11×10^{-4}	0.0392	0.137
MoSeTe/Gr	6.31×10^{-4}	0.0580	0.186
MoS$_{0.67}$Se$_{0.67}$Te$_{0.67}$/Gr	4.00×10^{-6}	0.0468	0.253
10 wt% Pt/C	1.126×10^{-3}	0.0300	0.088

From the **Table 3**, the lowest value for the Tafel constant is found for the molybdenum sulfotelluride/graphene (MoSTe/Gr) nanocomposite. Considering all the descriptors, MoSTe/Gr becomes apparent as the optimum nanocomposite for the HER electrocatalysis. It has more than one binding site with near-zero ΔG_b. It has the lowest overpotential, relatively low Tafel slope, and relatively high current density. Similar findings have been reported in the literature for metal-rich molybdenum chalcogenide nanocomposite comprised of sulfur and tellurium.[173]

4.3 Conclusion:

In summary, systematic computational and experimental investigations were carried out to evaluate the electrocatalytic performances for three non-hybrid molybdenum dichalcogenides and four hybrid molybdenum dichalcogenides with graphene support. The binding free energy values (ΔG_b) for hydrogen adsorption determined using DFT analysis show that all seven systems contain binding sites within the thermoneutral range of -0.2 eV and 0.2 eV, with MoS_2/Gr, $MoSe_2/Gr$, and MoSTe/Gr having the ΔG_b values closest to zero. It was also revealed that almost all catalytically active sites contain at least one Mo atom. Successful syntheses of molybdenum dichalcogenides over graphene support with compositions of MoS_2/Gr, $MoSe_2/Gr$, $MoTe_2/Gr$, MoSSe/Gr, MoSeTe/Gr, MoTe/Gr, and $MoS_{0.67}Se_{0.67}Te_{0.67}/Gr$ were carried out through a simple, ultrafast (90 s), and energy-efficient microwave-assisted solid-state technique. The as-produced nanocomposites have high activity and durability for HER electrocatalysis with overpotential values in the range of 127−217 mV and negligible activity loss for long-term hydrogen generation at constant potential of 250 mV. Among these nanocomposites, the $MoTe_2/Gr$, MoSTe/Gr, and MoSeTe/Gr samples demonstrate improved performance in comparison to the other nanocomposites in this study. Our study indicates that these promising results come from high intrinsic activities of nanocomposites containing the chalcogen tellurium at relatively high atomic ratios. Considering all four descriptors studied in this work (overpotential, Tafel slope, current density, and binding free energy of hydrogen), MoSTe/Gr ranks as the optimum candidate for cathodic material for electrocatalyic hydrogen generation from water splitting. Moreover, the correlation between experimental and computational results

demonstrates that the binding free energies are better correlated with the Tafel slope than the traditional volcano relationship which uses current density.

5. Enhancement of Hydrogen Evolution Reaction Activity using Metal−rich Molybdenum Sulfotelluride with Graphene Support: A Combined Experimental and Computational Study

5.1. Introduction

Hydrogen is an excellent storage solution for intermittent renewable energy resources. One of the effective strategies is to utilize the electricity from renewable sources to split water into hydrogen and oxygen.[199–201] Thus, the extra electricity generated from renewables can be stored as a form of useful hydrogen energy and while required this hydrogen can be used in fuel cells or in chemical industries. During this water electrolysis, the negative electrode (also known as cathode) undergoes with the hydrogen evolution reaction (HER). However, the efficiency of water-splitting reaction is very low, mainly due to the high overpotential. In this regard, the electrocatalysts are critical as cathode materials to promoting the HER kinetics and make the process energy-efficient by reducing overpotential.[202,203] In convention, platinum (Pt) and Pt-group metals are well recognized as highly efficient HER catalysts. Nevertheless, their high cost and lack of resource prevent their widespread industrial applications.[180,204,205] In purpose to establish a cost-effective production of green hydrogen, there is no alternative than replacing the expensive Pt-electrodes. As a result, last couple of decades have witnessed a fast-paced expansion of noble-metal-free HER electrocatalysts, including transition-metal chalcogenides (TMCs)[206–209] phosphides[210,211], carbides[212,213], etc., considering their unique properties of driving good electrocatalytic performance with low cost and natural abundance. To achieve better catalytic activities of TMC-based catalysts, structural engineering has been robustly practiced by many researchers. Numerous techniques have already been developed, such

as increasing the number of active sites by generating different nanostructured morphologies, by hybridizing with highly conductive materials such as graphene, reduced graphene oxide (rGO), carbon nanotubes (CNTs), or conducting polymers (polypyrrole, polyaniline, etc.), and by introducing dopants, defects, strains and vacancies through various surface modifications.[214–221] In addition, the HER activity of metal chalcogenides can be tuned by partially substituting one chalcogen (S, Se, or Te) with another chalcogen (S, Se or Te), leading to a new type of material with broken symmetry along the Z direction, thus improving the electrocatalytic performances in HER.[156,169,222–224] For instance, J. Zhang et al. has observed significantly improved HER performance in a single-layer SeMoS Janus structure compared to both MoS_2 and $MoSe_2$.[225] Similarly, in another study, T. Kosmala has demonstrated better HER results from molybdenum selenotellurides than $MoSe_2$ and $MoTe_2$.[169] Therefore, the doping at anion (chalcogen) sites of TMC compounds has the high potential for inventing new materials with enhanced electrocatalytic properties. Although, the coupling of metal chalcogenides with conducting supports (such as graphene, rGO, CNT, etc.) are essential to prevent the easy aggregation of TMC-layers, only a few of Janus-type Mo-S-Se compounds have been hybridized with conducting supports.[171,226,227] Moreover, the sulfides and selenides have been studied vigorously, while only a few of the recent papers have been focused on the remarkable properties and potential applications of telluride-based materials.[169,192,228–230] To the best of our knowledge, there has not been any work demonstrated electrocatalytic properties of molybdenum sulfotelluride compound for HER.

Molecular modeling studies have been performed with periodic plane-wave density functional theory (DFT) to delve into the surface-electrochemistry of hydrogen binding (also known as chemisorption or adsorption). Binding energetics, which are considered major descriptors for catalytic performance but difficult to attain with experimental measurement, have been calculated with DFT. The role of binding energy in catalysis is supported by Sabatier's principle, stating that for ideal catalysis conditions the binding free energy should be near zero.[131] In this computational analysis, the conventional criterion of $\Delta G_{binding} \approx 0$ has been considered as the measure to establish the most suitable binding sites for HER catalysis.

In literature, there are many studies for molybdenum chalcogenides with or without graphene support as hydrogen electrodes, but to the best of our knowledge no similar study has yet been carried out to understand HER activity of metal rich nanocomposite of molybdenum sulfotelluride and graphene as an electrocatalyst.[101,115,116,130,159,171] In this computational study, the free energy calculations have been performed with zero applied overpotential ($\eta = 0$) as per the established norm. The most well-known graphical depiction of Sabatier's principle is the volcano plot, which in this study exhibits the position of molybdenum sulfotelluride/graphene nanocomposite near the apex of the volcano.[131,132] Our combined experimental and computational studies demonstrate the higher electrocatalytic ability of MoS_xTe_y/Gr composite comprised of a higher molybdenum-to-chalcogen ratio for HER, thus showing potential for practical application with prospective commercialization.

5.2 Computational Methodology

In the computational analysis, multiple types of molybdenum sulfotelluride/graphene nanocomposite systems have been studied, as described in Table 5.1. Initially, a $Mo_9S_8Te_{10}$/Gr composite structure was constructed, with stoichiometric ratio between molybdenum and chalcogen atoms in the nanoparticle. The three additional systems have been designed to be comprised of more molybdenum atoms than the stoichiometric ratio. The $Mo_9S_8Te_{10}$/Gr composite structure was generated by constructing a supercell model of $Mo_9S_8Te_{10}$ supported on a $7 \times 7 \times 1$ graphene basal plane. To create the $Mo_9S_8Te_{10}$ nanoparticles, initially a Mo_9Te_{18} nanoparticle was created from the previously optimized geometry in the solid state hexagonal $MoTe_2$ lattice. Subsequently, eight Te atoms were replaced with eight S atoms in a random sequence. For the $Mo_9S_8Te_{10}$ nanoparticle, the $(01\bar{1}0)$ plane best represents the exposed chalcogen edge, and similarly the $(10\bar{1}0)$ plane best represents the exposed Mo edge. After the geometry optimization calculation of the $Mo_9S_8Te_{10}$/Gr structure, a $Mo_9S_6Te_7$/Gr nanocomposite structure was constructed by systematically removing one Te atom from the bottom layer of the exposed Mo edge ($10\bar{1}0$ plane), one Te atom from the upper layer of the chalcogen edge ($01\bar{1}0$ plane), one S atom from the upper layer of the chalcogen edge ($10\bar{1}0$ plane), and one S and one Te atoms from the chalcogen corner site.

Table 5.1: Optimized geometries of molybdenum sulfotelluride/graphene nanocomposite structures from periodic plane-wave DFT calculations.

H C S Mo Te	Mo$_9$S$_8$Te$_{10}$/Gr	Mo$_9$S$_6$Te$_7$/Gr	Mo$_9$S$_4$Te$_5$/Gr (Type-1)	Mo$_9$S$_4$Te$_5$/Gr (Type-2)
Top views of nanoparticles				
Side views of nanoparticles				
Top views of nanoparticles over graphene				
Side views of nanoparticles over graphene				
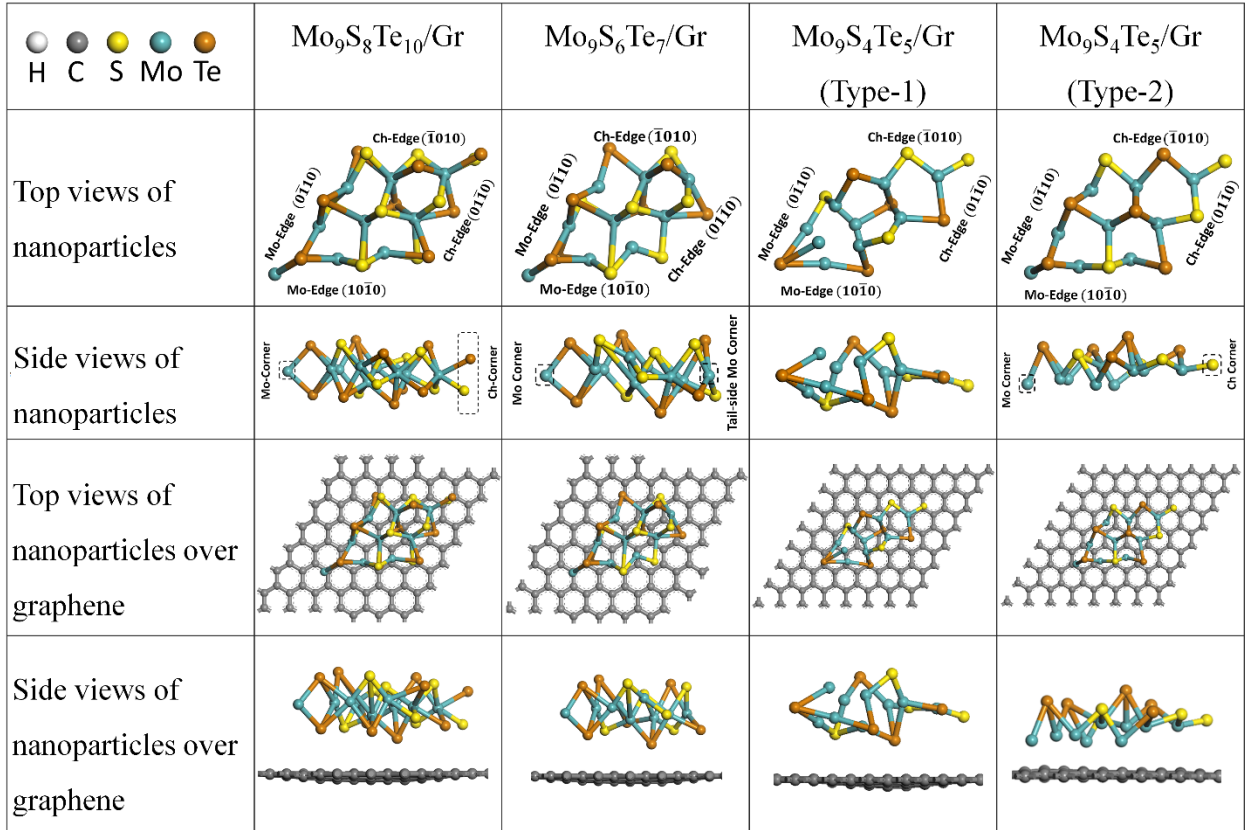
To capture the trends in experimental results from our Dr. Xinyu Zhang's lab, two types of Mo$_9$S$_4$Te$_5$/Gr model systems were considered with a similar atomic ratio as experiments (1: 0.46: 0.58 ≈ 9:4:5). The nanoparticles Mo$_9$S$_4$Te$_5$ were constructed using the same methodology. Two types of nanoparticles were constructed. In Type-1, all of the Mo atoms were kept on the upper layer with chalcogen atoms adjacent to the graphene. In Type-2, all of the chalcogen atoms were kept on the upper layer with the Mo atoms adjacent to the graphene. After the geometry optimization, the structure of Type-1 Mo$_9$S$_4$Te$_5$ nanoparticle showed significant curvature with the upward movement of chalcogenide atoms as the Mo atoms favored Mo-Mo bond formation to minimize total energy; as a result, the Type-1

structure showed no distinguishable Mo corners or Mo edges. This geometric distortion of the 2-D shape in the Type-1 structure was not observed in the Type-2 structure, where the graphene support served a more significant role in conserving the 2-D structure of the nanoparticle.

The computational study has been carried out using periodic plane-wave density functional theory (DFT) with the Cambridge Serial Total Energy Packages (CASTEP).[83,134,184–186,231–234] For the level of theory, spin polarized generalized gradient approximation (GGA) with Perdew-Burke-Ernzerhof (PBE) functional has been used with Kohn-Sham orbitals with an energy cutoff of 400 eV.[85,135,235] The effect of the core electrons has been represented with the Vanderbilt Ultrasoft Pseudopotentialls (USPP) method.[136] To address the nonbonded interactions of the nanocomposites, a semi-empirical dispersion energy correction is utilized by the method of Tkatchenko and Scheffler (TS).[23] In all geometry optimization calculation, two point steep gradient displacement (TPSD) algorithm is used.[137] For the dipole correction, self-consistent scheme has been applied. Relativistic treatment has been done with Koelling-Harmon Scalar method.[139] A vacuum space of 20 Å has been used between vertically repeated composite models for all the systems. For all constructed nanocomposites in this study, the Brillouin zones have been sampled by a $2\times2\times1$ k-point grid generated using Monkhorst-Pack scheme.[140] The convergence criteria for energy were set to 2×10^{-5} eV per atom and for displacement this tolerance was set to 0.002 Å.

5.3 Results and Discussion:

For the computational study, multiple hydrogen adsorption sites on each of the molybdenum sulfotelluride/graphene nanocomposites were investigated for binding energetics. Adsorbed hydrogen (H_{ads}) is the common intermediate species in all three steps of HER: Volmer, Hyerovsky and Tafel. The binding energetics of H_{ads} is established as one of the most important descriptors of potential hydrogen evolution catalysts with the assumption of Brønsted-Evans-Polanyi (BEP) linear correlations between reaction energy and the activation energy of an elementary reaction.[188,189]

For the $Mo_9S_8Te_{10}$/Gr nanocomposite structure, these binding sites consist of chalcogen and Mo atoms. For the $Mo_9S_6Te_7$/Gr and $Mo_9S_4Te_5$/Gr (Type-1 & Type-2) structures, the binding sites are primarily comprised of exposed Mo atoms, since the sites associated with Mo atoms possessed the lowest binding energies for the $Mo_9S_8Te_{10}$/Gr structure. For each of these sites, the effective binding electronic energy for a single hydrogen atom on the nanoparticle supported by the graphene, has been calculated using the following equation:

$$\Delta E_{Binding} = \frac{1}{2}(E_{2H^*+Nanocomposite} - E_{Nanocomposite} - E_{H_2}) \ldots\ldots\ldots\ldots\ldots\ldots\ldots (1)$$

Here $E_{2H^*+Nanocomposite}$ is the total electronic energy of the two hydrogen atoms bound to the nanoparticle-graphene composite, $E_{Nanocomposite}$ is the total electronic energy of only nanoparticle-graphene composite, and E_{H_2} is the electronic energy of a hydrogen molecule placed in 17.2Å×17.2Å×20Å vacuum hexagonal unit cell. Binding free energy ($\Delta G_{Binding}$) which is a more appropriate descriptor for the catalytic activity than electronic energy

alone, has been calculated using the generalized expression for HER catalysis developed by Nørskov and coworkers in the following equation[110]:

$$\Delta G_{Binding} = \Delta E_{Binding} + 0.24 \ eV \ \dots\dots\dots\dots\dots\dots\dots\dots\dots\dots\dots\dots \ (2)$$

For the $Mo_9S_8Te_{10}$/Gr nanocomposite structure, the binding electronic energy values range from -0.292 eV to 0.565 eV, and the binding free energy values range from the -0.052 eV to 0.805 eV (**Fig. 4** and **Table S5**, respectively). The exposed Mo corner site exhibits the most thermoneutral free energy change (-0.052 eV), i.e. the lowest absolute value of binding free energy ($|\Delta G_{Binding}|$). Thus, the Mo corner is the most optimal catalytic active binding site for hydrogen evolution according to the Sabatier Principle for this nanocomposite structure.

Table 5.2: Theoretically calculated binding energies ($\Delta E_{binding}$ and $\Delta G_{binding}$) of hydrogen atoms on a number of adsorption sites of $Mo_9S_8Te_{10}$/Gr composite.

	Binding sites	$\Delta E_{binding}$ (eV)	$\Delta G_{binding}$ (eV)
1	Chalcogen Edge (Vicinal)	0.357	0.597
2	Mo Corner	-0.293	-0.053
3	Mo and Chalcogen Edge (Ch=Te)	0.565	0.805
4	Mo and Chalcogen Edge (Ch=S)	0.175	0.415
5	Chalcogen Top (Ch=Te & S)	0.614	0.854
6	Chalcogen Top (Ch=S)	0.385	0.625
7	Chalcogen Corner	0.003	0.243

Table 5.3: Theoretically calculated binding energies ($\Delta E_{binding}$ and $\Delta G_{binding}$) of hydrogen atoms on various Mo based binding sites of $Mo_9S_6Te_7/Gr$ composite.

	Binding sites	$\Delta E_{binding}$ (eV)	$\Delta G_{binding}$ (eV)
1	Mo Corner	-0.286	-0.046
2	Mo Edge 1	0.169	0.409
3	Mo Edge 2	-1.153	-0.913
4	Mo Corner and Mo Edge	-0.065	0.175
5	Mo Corner (tail side)	-0.164	0.076

Table 5.4: Theoretically calculated binding energies ($\Delta E_{binding}$ and $\Delta G_{binding}$) of hydrogen atoms on various Mo based binding sites of $Mo_9S_4Te_5/Gr$ (Type-1) composite.

	Binding sites	$\Delta E_{binding}$ (eV)	$\Delta G_{binding}$ (eV)
1	Mo Corner	-1.005	-0.765
2	**Mo Corner and Mo Edge 1**	**-0.191**	**0.048**
3	Mo Corner and Mo Edge 2	-0.992	-0.752
4	**Mo Tail Corner and Mo Edge**	**-0.203**	**0.036**

Table 5.5. Theoretically calculated binding energies ($\Delta E_{binding}$ and $\Delta G_{binding}$) of hydrogen atoms on various Mo based binding sites of $Mo_9S_4Te_5$/Gr (Type-2; chalcogen atoms on top) composite.

	Binding sites	$\Delta E_{binding}$ (eV)	$\Delta G_{binding}$ (eV)
1	Mo Corner	-0.715	-0.475
2	**Mo Corner and Mo Edge 1**	**-0.283**	**-0.043**
3	Mo Corner and Mo Edge 2	-0.845	-0.605

Figure 5.1: Calculated free energy of binding (ΔG: denoted with red circles) and binding electronic energy (ΔE: denoted with black squares) values at different binding sites of the $Mo_9S_8Te_{10}$/Gr nanocomposite structure. The binding site indexing is as follows: (1) Chalcogen edge, (2) Mo corner, (3) Mo edge-Te edge, (4) Mo edge-S edge, (5) Chalcogen top (S & Te), (6) Chalcogen top (only S), and (7) Chalcogen corner.

Based on the results of the $Mo_9S_8Te_{10}$/Gr nanocomposite structure, an additional $Mo_9S_6Te_7$/Gr nanocomposite structure was constructed with more exposed Mo corner sites by systematically removing chalcogen atoms from the $Mo_9S_8Te_{10}$ nanoparticle. For this nanocomposite, only Mo-based binding sites are considered for the calculation based on learnings from the previous structure of stoichiometric ratio. The resultant binding electronic energy values range from -1.153 eV to 0.169 eV, and the range of binding free energy values is from -0.046 eV to 0.409 eV (**Fig. 5.2** and **Table 5.3**, respectively). For the $Mo_9S_6Te_7$/Gr structure, three adsorption sites are found that have near zero binding free energy values ($\Delta G_{Binding} \approx 0$): (i) the exposed Mo corner, (ii) the exposed tail-side Mo corner, and (iii) the bridge site between a Mo corner atom and a Mo edge atom.
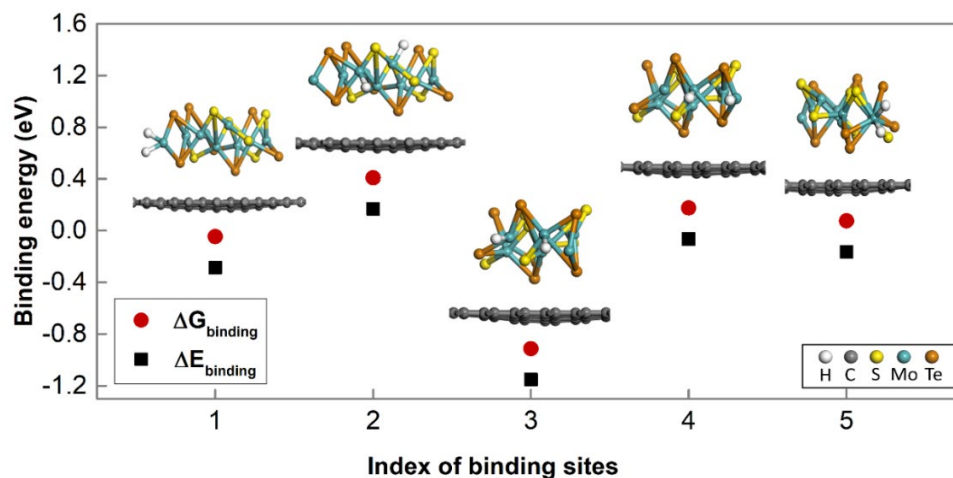
Figure 5.2: Calculated free energy of binding (ΔG: denoted with red circles) and binding electronic energy (ΔE: denoted with black squares) values at different binding sites of $Mo_9S_6Te_7$/Gr nanocomposite structure. The binding site indexing is as follows: (1) Mo corner, (2) Mo edge 1, (3) Mo edge 2, (4) Mo corner-Mo edge, and (5) tail-side Mo corner.

In case of the two types of Mo$_9$S$_4$Te$_5$/Gr nanocomposite structures, which were constructed to closely resemble the atomic ratio (Mo: S: Te = 1: 0.46: 0.58 ≈ 9: 4: 5) of the experimentally determined best system (Figures 5.3), only Mo-based hydrogen binding sites are considered based on learnings from the previous structure of stoichiometric ratio. In both types of these metal-rich nanocomposites, a number of thermoneutral hydrogen binding energy values have been observed. In the Type-1 Mo$_9$S$_4$Te$_5$/Gr nanocomposite structure, two optimal binding sites are found, and both of these sites are comprised of the Mo corner (Figure 5.3). In the Type-2 Mo$_9$S$_4$Te$_5$/Gr nanocomposite structure with all chalcogen atoms on the upper layer, the number of available binding sites with primarily Mo atoms is very limited. Yet, as displayed in Figure 5.3 and Tables 5.5, one site comprised of a partial Mo corner does show a binding free energy value in close proximity to zero.
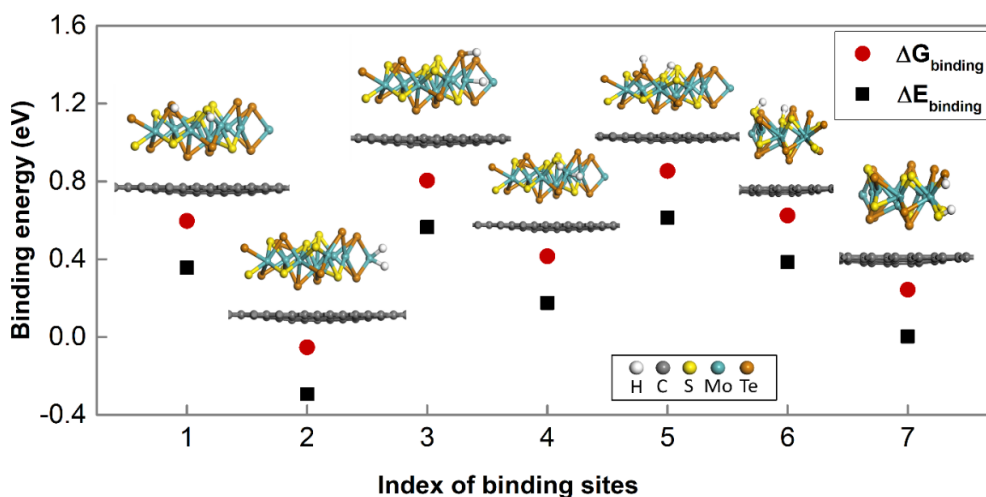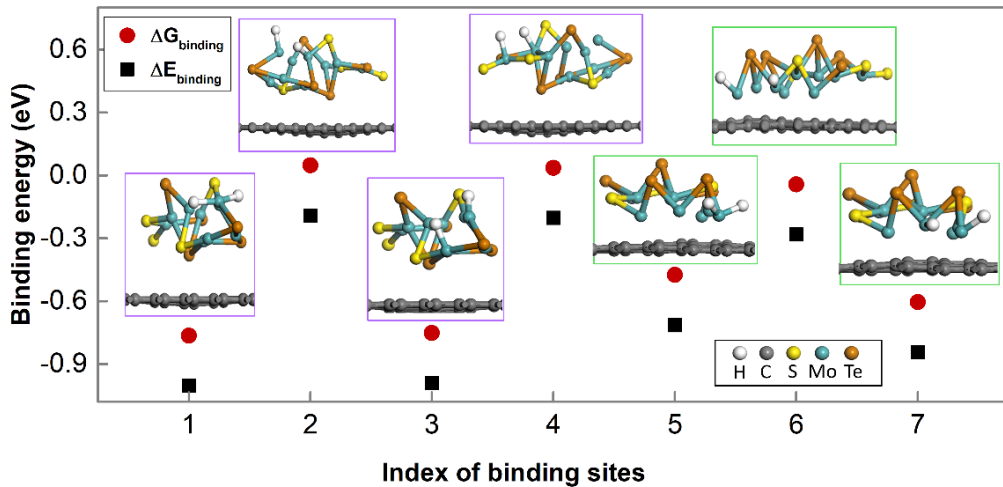

Figure 5.3: Calculated free energy of binding (ΔG: denoted with red circles) and binding electronic energy (ΔE: denoted with black squares) values at different binding sites for both types of Mo$_9$S$_4$Te$_5$/Gr nanocomposite (Type-1 and Type-2) structures. The binding site indexing is as follow; for **Type-1** (purple boxes): (1) Mo corner, (2) Mo corner-Mo

edge 1, (3) Mo corner-Mo edge 2, (4) tail-side Mo corner-Mo edge, and for **Type-2** (green boxes): (5) Mo corner, (6) Mo corner-Mo edge 1, and (7) Mo corner-Mo edge 2.

Conventionally, the binding free energies for high-performing catalytically active sites are within the range of -0.2 eV and 0.2 eV. Each of the composite systems which have been considered in this computational investigation possess binding sites within this range. Notably, the two Mo-rich systems ($Mo_9S_6Te_7$/Gr and $Mo_9S_4Te_5$/Gr) have multiple catalytically active binding sites according to the Sabatier's principle (**Figure 5.6**) as compared to the composite system comprised of a nanoparticle of stoichiometric ratio of metal to chalcogen atoms.

As seen in **Figure 5.2**, for instance, there are significant differences among the binding free energies of similar binding sites (e.g., $\Delta G_{Binding}$ of Mo edge 1 and Mo edge 2 sites in $Mo_9S_6Te_7$/Gr) due to the asymmetric nature of binary active sites where Mo atoms may have different configurations of chalcogen neighbors. An important implication of these binary active sites is the existence of synergy between a binding site and its nearest neighboring atoms due to both steric and electronic effects.

Besides the computational studies, experimental investigations of electrocatalytic HER activities of six samples molybdenum sulfotelluride (MST) were carried out by Dr. Shatila Sarwar under the supervision of Professor Xinyu Zhang. Experimental studies were done with linear sweep voltammograms (LSVs) in an acidic electrolyte of 0.5 M H_2SO_4. The *iR* corrected−LSVs are shown in **Figure**, where MST-2 displays the best catalytic behavior with the smallest overpotential (η) of 62.2 mV *vs*. RHE to reach the cathodic current density

of 10 mA cm^{-2}. As displayed in **Figure**, the order of HER activity based on η is MST-2 > MST-1 > MST-5 > MST-6 > MST-3 > MST-4. It clearly indicates, the ratio of molybdenum sulfide to molybdenum telluride is crucial to the catalytic ability and it is found that too much of sulfur does not favor the hydrogen evolution (for MST-3 and MST-6, **Figure 5.4b**). On the other side, the best results are found from the samples containing almost equal ratio of S and Te (MST-2, MST-5) or sample with a little high amount of Te (MST-1). Among these samples, MST-1 may have contained some unreacted Te-powder, and the physical mixture of MST-5 may not have a fully interconnected network in crystal structure, which limit their catalytic performances. Besides, MST-4 contains a very small amount of active catalyst comparing to the high amount of graphene present in the sample, thus does not show good HER activity. Consequently, MST-2 exhibits the best combination of molybdenum sulfide and molybdenum telluride ratio on graphene network and is further studied for electrocatalytic behaviors, which is renamed as 'MoS$_{0.46}$Te$_{0.58}$/Gr' based on the XPS elemental results. The HER activity of MoS$_{0.46}$Te$_{0.58}$/Gr nanocomposite was compared with bare GCE, graphene, MoS$_2$/Gr, MoTe$_2$/Gr, and 10 wt.% Pt/C catalyst samples based on LSV curves (Figure 5.4). The observed overpotentials (η) for these samples are displayed in Figure 5.4 and it clearly indicates that MoS$_{0.46}$Te$_{0.58}$/Gr catalyst emerges with a smaller overpotential than those of MoS$_2$/Gr and MoTe$_2$/Gr samples. The η of MoS$_{0.46}$Te$_{0.58}$/Gr is around only 62.2 mV at 10 mA cm^{-2}, and the cathodic current density rises promptly with an increase in η. In comparison, both MoS$_2$/Gr and MoTe$_2$/Gr exhibit higher overpotential, approximately 197.2 and 167.1 mV, respectively. In contrast, bare GCE and graphene does not show any catalytic activity. Furthermore, the Tafel diagrams were derived from LSVs by fitting the linear sections to the Tafel equation (η =

a + b log i), where η is overpotential, a is a constant, b is the Tafel slope and i represents the cathodic current density.[187] Tafel slope can reveal the rate determining step (RDS) during hydrogen generation. As a result of applying sufficient potential at specific reaction condition, the HER takes place through an adsorption step (Volmer, $H^+ + e^- \rightarrow H_{ads}$, 120 mV dec^{-1}), following by a reduction step (Heyrovsky, $H^+ + H_{ads} + e^- \rightarrow H_2$, 40 mV dec^{-1} or Tafel, $2H_{ads} \rightarrow H_2$, 30 mV dec^{-1}).[187] Tafel step is the fastest reaction in HER, therefore it is noticeable that the smaller Tafel slope favors HER activities. From the present results shown in Figure 5.4, MoS$_{0.46}$Te$_{0.58}$/Gr exhibits a Tafel slope of 61.1 mV dec^{-1}, which combines both outcomes from MoS$_2$/Gr (54.2 mV dec^{-1}) and MoTe$_2$/Gr (99.4 mV dec^{-1}). Moreover, it suggests that the Volmer–Heyrovsky reaction mechanism dominates in the HER process of MoS$_{0.46}$Te$_{0.58}$/Gr. In addition, the exchange current densities (i_0) are also measured following the Tafel slope extrapolation method,[187] and all the key parameters of HER performance are displayed in Table 5.6. The kinetics of hydrogen evolution process was further investigated by electrochemical impedance spectroscopy (EIS) measurements. Figure 5.4 represents the Nyquist plots of bare GCE, graphene, MoS$_2$/Gr, MoTe$_2$/Gr and MoS$_{0.46}$Te$_{0.58}$/Gr at a given overpotential of 150 mV, and corresponding R$_s$ and R$_{ct}$ values are displayed in Table 5.6, based on the Z-fitting obtained from EC-Lab software. Here, a small internal resistance (R_s) of 0.516 Ω cm^2 for MoS$_{0.46}$Te$_{0.58}$/Gr indicates that the intrinsic resistance of electrode material and ionic resistance of electrolyte is much low for the hybrid MoS$_{0.46}$Te$_{0.58}$/Gr system. In the high−frequency zone, it exhibits one capacitive semicircle, indicating that the reaction is kinetically controlled. This semicircle represents the charge transfer process at the interface between the electrolyte and the catalytic electrode, which is composed of the charge

transfer resistance (R_{ct}) and the double layer capacitance (C_{dl}). The lower value of R_{ct} represents faster charge transfers in the electrode, resulting rapid reaction in the electrocatalytic kinetics. The low−frequency inclined line signifies the Warburg impedance (Z_W) for the diffusion process of H^+ ions through active materials, which is prominently shown for only $MoS_{0.46}Te_{0.58}$/Gr hybrid. As exhibited in Figure 5.4 and Table 5.6, a small R_{ct} of 10.294 Ω cm^2 can be found for $MoS_{0.46}Te_{0.58}$/Gr, which indicates a higher conductivity and faster electron transfer process, and further explains the higher HER activity of $MoS_{0.46}Te_{0.58}$/Gr catalyst.

Table 5.6: The major HER parameters of all catalyst sample measured with LSV

Samples	Overpotential (mV vs. RHE)	Tafel slope (mV dec^{-1})	Exchange current density, i_0 (A cm^{-2}) × 10^{-3}	Normalized solution resistance, R_s (Ohm cm^2)	Normalized charge transfer resistance, R_{ct} (Ohm cm^2)
Bare GCE	> 400	-	-	1.102	79.474
Graphene	> 350	-	-	1.061	71.145
MoS$_2$/Gr	197.2	54.2	0.075	0.601	57.373
MoTe$_2$/Gr	167.1	99.4	0.194	0.672	34.692
MoS$_{0.46}$Te$_{0.58}$/Gr	62.2	61.1	0.694	0.516	10.294
10 wt.% Pt/C	47.7	32.1	1.882	0.488	7.876
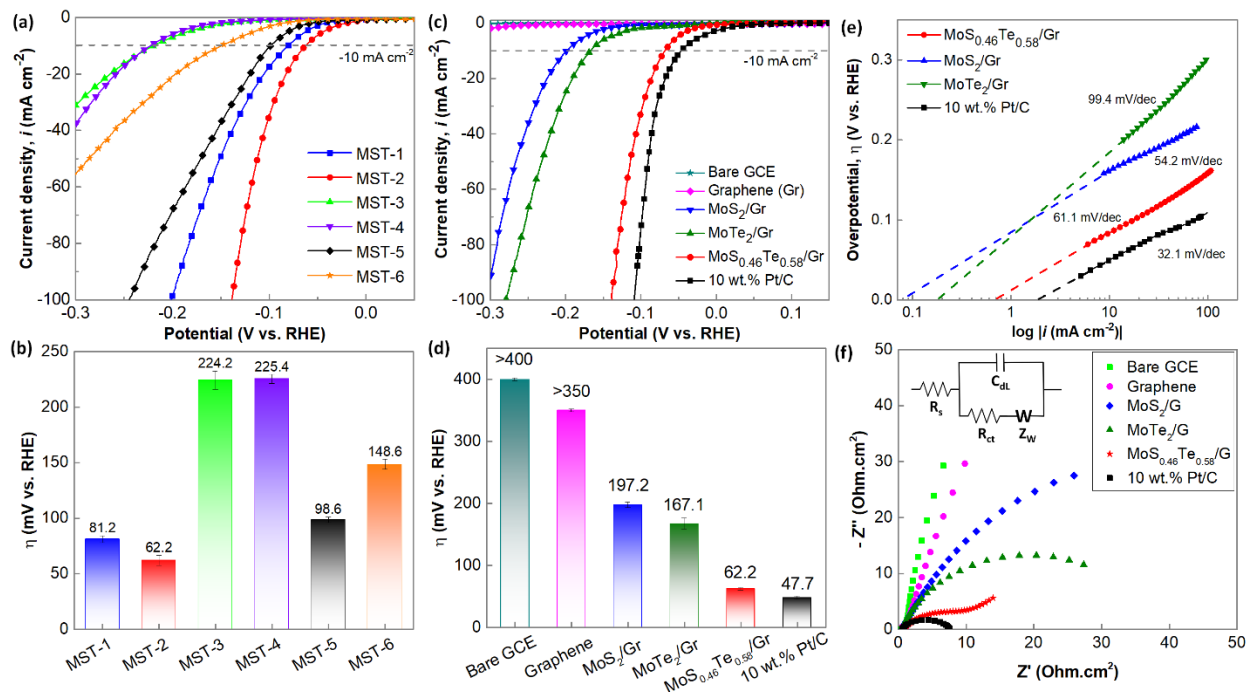
Figure 5.4: (a) LSVs at a scan rate of 2 mV s^{-1} for samples MST-1 to MST-6. (b) Corresponding overpotentials to reach the current density of 10 mA cm^{-2}. (c) LSVs of bare GCE, graphene, MoS$_2$/Gr, MoTe$_2$/Gr, MoS$_{0.46}$Te$_{0.58}$/Gr and Pt/C catalysts at a scan rate of 2 mV s^{-1}. (d) Corresponding overpotentials at the cathodic current density of 10 mA cm^{-2}. (e) Tafel slopes and (f) Nyquist plots of catalyst samples.

Finally, a continuous cycling test was carried out for 5000 cycles at a scan rate of 50 mV s^{-1} to determine the long-term durability of MoS$_{0.46}$Te$_{0.58}$/Gr catalyst. Their polarization curves are displayed in **Figure 5.5a** within a potential range of 0 to −0.25 V *vs.* RHE. The polarization curves show slight changes after 5000 cycles, resulting an overpotential (η) shift of only 10 mV at high current density of −200 mA cm^{-2}. Additionally, a chronoamperometric curve was obtained at the η of 150 mV, which is presented in **Figure 5.5b**. This constant potential test exhibits almost no degradation in the cathodic current

density (around −45 mA cm^{-2}) for over 90 h of electrolysis. It suggests the remarkable stability of MoS$_{0.46}$Te$_{0.58}$/Gr during the HER process, which can well be attributed to compositional and structural stability of MoS$_{0.46}$Te$_{0.58}$/Gr heterostructure supported by graphene network. Moreover, the electrochemical double-layer capacitance (C$_{dl}$) was measured to evaluate the electrochemically active surface area (ECSA) of MoS$_{0.46}$Te$_{0.58}$/Gr hybrid. The ECSA value is supposed to be linearly proportional to the value of C$_{dl}$, which can be derived by CV measurements.[236] **Figure 5.5c** and **5.5e** exhibit the non-faradaic CV curves for MoS$_{0.46}$Te$_{0.58}$/Gr catalyst before and after the cycling stability tests for 5000 cycles, respectively. As shown in **Figure 5.5d**, the variation of average capacitive currents, $\frac{1}{2}$ (i$_a$−i$_c$) are displayed with respect to the scan rate for MoS$_2$/Gr, MoTe$_2$/Gr and MoS$_{0.46}$Te$_{0.58}$/Gr catalyst samples. Additionally, as shown in **Figure 5.5f**, C$_{dl}$ of MoS$_{0.46}$Te$_{0.58}$/Gr increases almost four times, resulting the value of 70.52 mF cm^{-2} after 5000 cycles of HER test. This phenomenon indicates an improvement in active sites of the material due to the H$_2$ bubbling from catalyst surface, creating more defects in nanosheets. The elemental and structural analyses of MoS$_{0.46}$Te$_{0.58}$/Gr were further examined after stability test, where the results clearly show insignificant degradation of active material after 5000 cycles. The atomic ratio retains almost similar as initial and MoS$_{0.46}$Te$_{0.58}$ nanosheets remain uniformly embedded in graphene network.
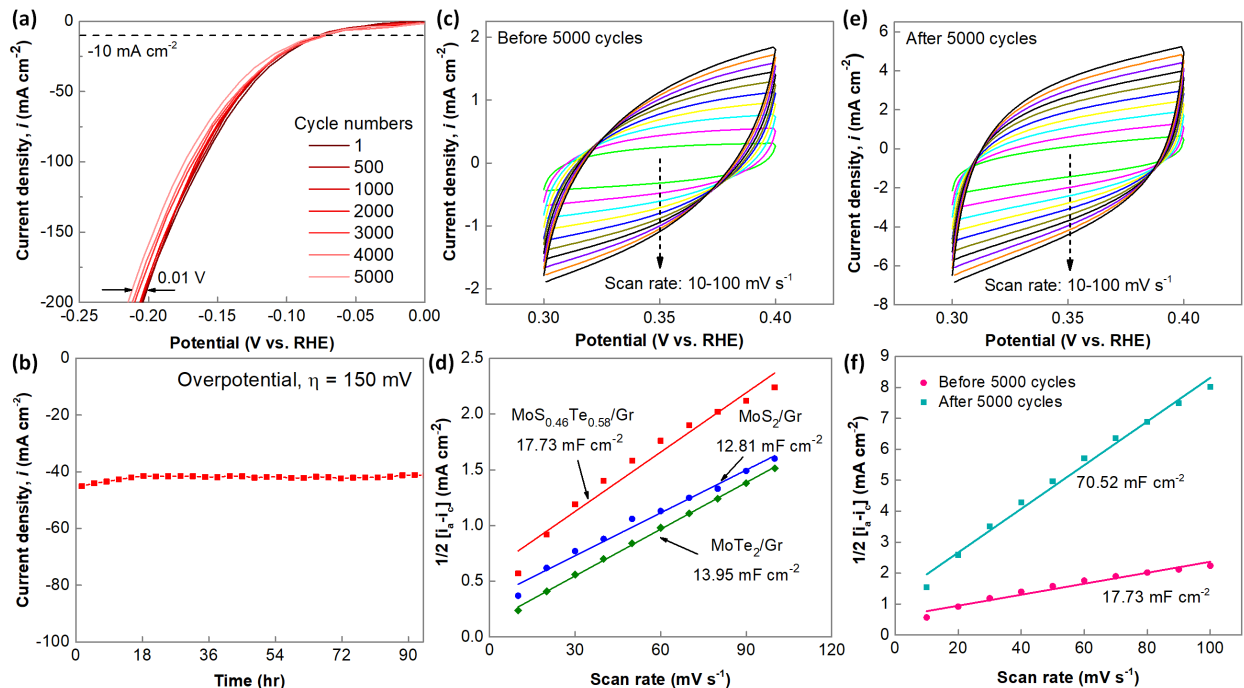
Figure 5.5: (a) Cycling stability of $MoS_{0.46}Te_{0.58}$/Gr at a scan rate of 50 mV s^{-1} (LSV curves from 1 to 5000 cycles are displayed). (b) Chronoamperometric curve during the electrolysis over 90 hours at a constant overpotential of 150 mV. (c) CVs of $MoS_{0.46}Te_{0.58}$/Gr in a non-faradaic potential window before 5000 cycles. (d) Measured EDLCs for MoS_2/Gr, $MoTe_2$/Gr and $MoS_{0.46}Te_{0.58}$/Gr. (e) CVs of $MoS_{0.46}Te_{0.58}$/Gr in a non-faradaic potential window after 5000 cycles. (f) Measured EDLCs for $MoS_{0.46}Te_{0.58}$/Gr before and after 5000 cycles.

The above results unambiguously reveal that the $MoS_{0.46}Te_{0.58}$/Gr nanocomposite acquires improved HER activity in comparison to either MoS_2/Gr or $MoTe_2$/Gr. The superior HER performance can be considered from the combination of molybdenum sulfide and molybdenum telluride presents a synergistic effect on graphene network, assembling the intrinsic properties of the two components. Therefore, more active sites have been exposed due to the surface defects and shorten the electron transfer pathways. Additionally, the

133

stable connection between $MoS_{0.46}Te_{0.58}$/Gr nanostructure and graphene can further remarkedly accelerate the electron transfer ability, favoring the much enhanced HER performance and stability for long-term tests. From this study, it has also been demonstrated that Mo-rich nanocomposites with the slight increase in Te fraction (or conversely reduction of S) in the hybrid nanostructure is associated with better catalytic performances.

Moreover, using the experimentally measured current density (i_0) along with the theoretically determined $\Delta G_{binding}$ value of the best performing nanocomposite, the relative position of this nanocomposite in the volcano plot (**Figure 5.7**) is found very close to the apex, approaching the high-performing noble metals Pt and Pd.
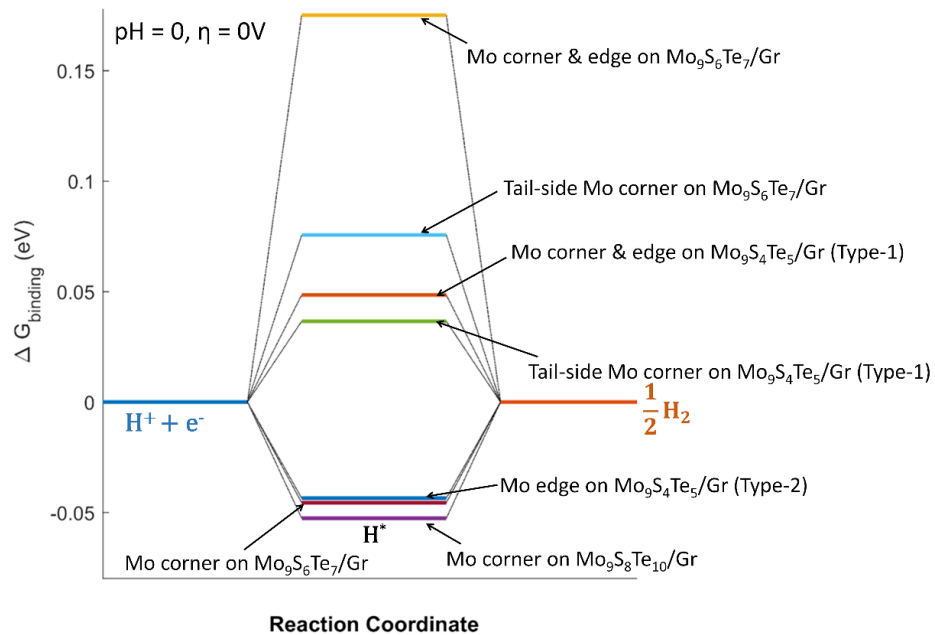
Figure 5.6: Free energy diagram for effective hydrogen atom binding at equilibrium ($\eta = 0$ V). Values of the binding free energy of Pt and Pd are taken from literature.
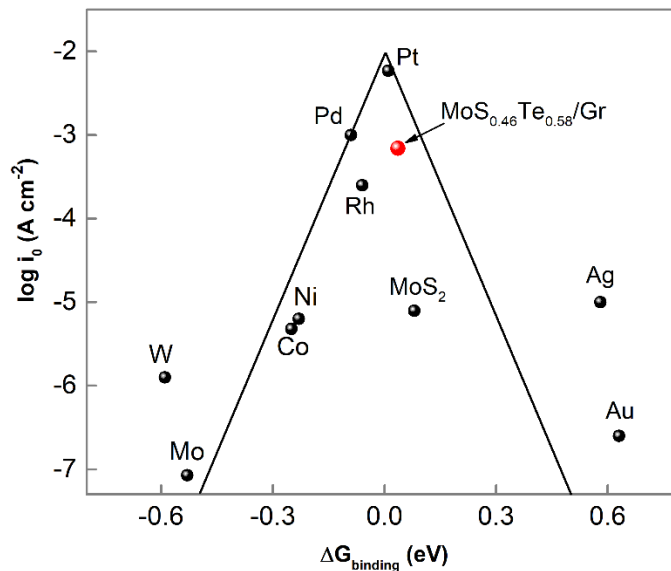
Figure 5.7: Volcano plot of experimentally measured current density (i_0) vs. DFT calculated Gibbs free energy of hydrogen binding ($\Delta G_{binding}$). With the exception of the $MoS_{0.46}Te_{0.58}$/Gr system, all presented data values are from literature sources.[110,145,146] The computationally derived $\Delta G_{binding}$ value for the $MoS_{0.46}Te_{0.58}$/Gr composite is from the $Mo_9S_4Te_5$/Gr system with the most similar empirical formula.

5.4. Conclusion

In summary, various samples with different precursor ratios were explored and their electrocatalytic HER activities were examined in acidic medium. It is evidenced that the HER catalytic activity is noticeably modified with the ratio of Mo, S and Te elements. The best result was found from the $MoS_{0.46}Te_{0.58}$/Gr nanocomposite consisting slightly more Te than S atom and higher amount of Mo than the stoichiometry, which shows a small overpotential of only 62.2 mV to reach the cathodic current density of 10 mA cm^{-2}, a small Tafel slope of 61.1 mV dec^{-1}, high TOF of 0.53 s^{-1} at an overpotential of 150 mV and

negligible degradation of activity from long−term stability tests. This excellent electrocatalytic behavior is derived from the coexistence of S and Te atoms which reduces the apparent activation energy by creating more active sites in defect−rich catalyst surface, accelerating both ion and electron transfer and the presence of graphene improves the electrical conductivity. In addition, the computational results clearly provide microscopic insight by way of effective hydrogen binding free energy values into the experimental catalytic performance for HER. Here, it has been deduced that the most active sites for catalysis of the molybdenum sulfotelluride/graphene nanocomposite are primarily comprised of exposed Mo atoms. This combined computational and experimental study shows the very high potential for the metal-rich molybdenum sulfotelluride nano-electrocatalyst with graphene support for hydrogen generation through water electrolysis. Moreover, in basis of the proposed microwave−assisted synthesis method, other hybrid metal chalcogenides can also be prepared in large−scale with low cost, high efficiency, and stability, which will boost the practical applications of metal chalcogenide−based heterostructures as high−performance HER electrocatalysts.

6. Future Research and Conclusion

6.1. Future Direction for the Study of Serine Protease

Serine proteases are classified based on their substrate specificity: trypsin-like, chymotrypsin-like, thrombin-like, elastase-like, and subtilisin-like. In this study, investigation of the reaction pathway analysis of serine protease has carried out with chymotrypsin enzyme. To have a more robust conclusion about the reaction mechanism of the serine proteases, same pathway analysis should be carried out with other enzyme representing different serine protease classes.

Besides carrying out reaction energetics calculation with atomistic modeling, experimental collaborations will be needed to test and confirm the hypothesis posited in this computational studies. A power full experimental method to test the reaction mechanism hypothesis is the isotope effect on enzyme catalysis. Replacing the one targeted specific hydrogen in the active site with deuterium, may alter the Michaelis-Menten parameters for that enzyme. Then carrying out the computational analysis of the enzyme with deuterium will provide the unbiased hypothesis test about the competing reaction mechanism. This should be an important direction for the future study.

The QM-cluster investigation, cannot provide the effect of pH and temperature on enzyme catalysis, which requires the study of full enzyme. QM/MM study can be very helpful for

this purposes. To find the ionization states of various residues while titrating the enzyme at various pH point with the help of various computational method (e.g. Tanford-Roxby, Monte Carlo proton transfer, Sham-Warshel method etc.).[237–239]

Very recently machine learning and artificial intelligence (AI) predicted modifications of a hydrolases have demonstrated significant advancement in efficiency and applicability.[240] Similar approach should be applied to rationally design a more efficient, industry friendly, and use-specific serine proteases.[241] Using existing databases for serine proteases and combining the insights gathered from atomistic modeling, machine learning can open a new window for potential improvements in the field of enzyme engineering.

6.2. Future Direction for the Study of HER with Transition Metal Chalcogenides with graphene nanocomposite

As mentioned in this document previously, according to the literature, there are disagreements about the decisive step of HER. According to the *slow discharge theory* the electrochemical adsorption step (Volmer reaction) is the decisive step. *Electrochemical desorption theory* insists that the electrochemical desorption step (Heyrovsky reaction) is the decisive one, whereas the *blending theory*, the rate determining step is the complex desorption step (Heyrovsky-Tafel reaction).[242] A full kinetic study with activation energy determination may help to settle the debate and elucidates more possible way to improving catalytic ability. The major hurdle for kinetic investigation, is to determining the activation which has to allow the removal of charge from the studied systems, which requires

modification of typical DFT codes.[190] Until recently these codes were not open, but since 2018 Solvated Jellium (SJ) method implemented in the GPAW package is allows for the addition/subtraction of electrons (or fractions thereof) to/from the unit cell in order to keep the electrode potential at a target value.[243–246] With the help of this or similar tools, along the determination of the decisive steps can be determined, the debate about the volcano plot may also be settled. Besides carrying out computational kinetic investigation, binding thermodynamics for hydrogen adsorption similar to this study in different active sites for other transition metal instead of molybdenum chalcogenides and their hybrid variations should be done for potential electrocatalyst screening. As a choice of conductive support, in place of graphene or reduced graphene oxide, nitrogen-doped graphene can be a highly potential arena for investigation.

Another potential future prospect is to apply data analysis and machine learning to HER catalyst screening.[247–249] Combining data points from atomistic modeling with machine learning is currently a highly active field of research.[250–252] Using various computational and experimental descriptors of all studied HER catalysts, machine learning tools may predict cathodic catalysts with high potential.[253–255]

References:

(1)   Grand View Research. Catalyst Market Size, Share, Trends, Industry Growth Report 2019-2025 https://www.grandviewresearch.com/industry-analysis/catalyst-market.

(2)   Weller, A.; Fletcher, S. Catalysis https://www.chem.ox.ac.uk/catalysis.aspx.

(3)   Armor, J. What is Catalysis or Catalysts, So what? http://nacatsoc.org/above/what-is-catalysis/3/.

(4)   Chorkendorff, I.; Niemantsverdriet, J. W. *Concepts of Modern Catalysis and Kinetics*, 3rd ed.; Wiley-VCH Verlag GmbH & Co. KGaA, 2017.

(5)   McNaught, A. D.; Wilkinson, A. *IUPAC Compendium of Chemical Terminology: Gold Book*, 2nd ed.; International Union of Pure and Applied Chemistry, 1997.

(6)   Carson, R. *Silent Spring*; Houghton Mifflin Company, 1962.

(7)   Commoner, B. *The Closing Circle: Nature, Man, and Technology*; Random House Inc., 1971.

(8)   Anastas, P. T.; Warner, J. 12 Principles of Green Chemistry https://www.acs.org/content/acs/en/greenchemistry/principles/12-principles-of-green-chemistry.html.

(9)   Linthorst, J. A. An Overview: Origins and Development of Green Chemistry. *Found. Chem.* **2010**, *12* (1), 55–68. https://doi.org/10.1007/s10698-009-9079-4.

(10)   Woodhouse, E. J.; Breyman, S. Green Chemistry as Social Movement? *Sci. Technol. Hum. Values* **2005**, *30* (2), 199–222. https://doi.org/10.1177/0162243904271726.

(11)   Green Chemistry Challenge Winners https://www.epa.gov/greenchemistry/green-chemistry-challenge-winners (accessed Jun 9, 2022).

(12)   *Catalysis: An Integrated Textbook for Students*; Hanefeld, U., Lefferts, L., Eds.; Wiley-VCH Verlag GmbH & Co. KGaA, 2018.

(13)   Godula-Jopek, A. Introduction. In *Hydrogen Production by Electrolysis*; Godula-Jopek, A., Ed.; Wiley-VCH Verlag GmbH & Co. KGaA, 2015; pp 1–32.

(14)   Sheldon, R.; Arends, I. W. C. E.; Hanefeld, U. *Green Chemistry and Catalysis*; Wiley-VCH Verlag GmbH & Co. KGaA, 2007.

(15)   Vakhrushev, A. V. *Computational Multiscale Modeling of Multiphase Nanosystems: Theory and Applications*; Apple Academic Press, 2018.

(16)   Levitt, M. Birth and Future of Multiscale Modeling for Macromolecular Systems (Nobel

Lecture). *Angew. Chemie - Int. Ed.* **2014**, *53* (38), 10006–10018. https://doi.org/10.1002/anie.201403691.

(17)   Karplus, M. Development of Multiscale Models for Complex Chemical Systems: From H+H2 to Biomolecules (Nobel Lecture). *Angew. Chemie - Int. Ed.* **2014**, *53* (38), 9992–10005. https://doi.org/10.1002/anie.201403924.

(18)   Warshel, A. Multiscale Modeling of Biological Functions: From Enzymes to Molecular Machines (Nobel Lecture). *Angew. Chemie - Int. Ed.* **2014**, *53* (38), 10020–10031. https://doi.org/10.1002/anie.201403689.

(19)   Fogler, H. S. *Elements of Chemical Reaction Engineering*, 5th ed.; Pearson, 2016.

(20)   Shuler, M. L.; Kargi, F. *Bioprocess Engineering: Basic Concepts*, 2nd ed.; Prentice Hall PTR, 2002.

(21)   *Electrocatalysis : Computational, Experimental, and Industrial Aspects*, 1st ed.; Zinola, C. F., Ed.; CRC Press, Taylor and Francis Group: Boca Raton, 2010.

(22)   Von Lilienfeld, O. A.; Tavernelli, I.; Rothlisberger, U.; Sebastiani, D. Optimization of Effective Atom Centered Potentials for London Dispersion Forces in Density Functional Theory. *Phys. Rev. Lett.* **2004**, *93* (15), 1–4. https://doi.org/10.1103/PhysRevLett.93.153004.

(23)   Tkatchenko, A.; Scheffler, M. Accurate Molecular van Der Waals Interactions from Ground-State Electron Density and Free-Atom Reference Data. *Phys. Rev. Lett.* **2009**, *102* (7), 6–9. https://doi.org/10.1103/PhysRevLett.102.073005.

(24)   Zimmerli, U.; Parrinello, M.; Koumoutsakos, P. Dispersion Corrections to Density Functionals for Water Aromatic Interactions. *J. Chem. Phys.* **2004**, *120* (6), 2693–2699. https://doi.org/10.1063/1.1637034.

(25)   Grimme, S. Accurate Description of van Der Waals Complexes by Density Functional Theory Including Empirical Corrections. *J. Comput. Chem.* **2004**, *25* (12), 1463–1473. https://doi.org/10.1002/jcc.20078.

(26)   Choi, Y.; Adamczyk, A. J. Tuning Hydrogenated Silicon, Germanium, and SiGe Nanocluster Properties Using Theoretical Calculations and a Machine Learning Approach. *J. Phys. Chem. A* **2018**, *122* (51), 9851–9868. https://doi.org/10.1021/acs.jpca.8b09797.

(27)   Minkler, M. J.; Kim, J.; Lawson, K. E.; Ali, A.; Zhao, R.; Adamczyk, A. J.; Beckingham, B. S. Solution Processible Statistical Poly(3-Methoxythiophene)-Co-Poly(3-Hexylthiophene) Copolymer. *Mater. Lett.* **2019**, *256*, 126563. https://doi.org/10.1016/j.matlet.2019.126563.

(28)   Bowler, D. R.; Miyazaki, T. O(N) Methods in Electronic Structure Calculations. *Reports Prog. Phys.* **2012**, *75* (3). https://doi.org/10.1088/0034-4885/75/3/036503.

(29)   Lever, G.; Cole, D. J.; Hine, N. D. M.; Haynes, P. D.; Payne, M. C. Electrostatic Considerations Affecting the Calculated HOMO-LUMO Gap in Protein Molecules. *J. Phys. Condens. Matter* **2013**, *25* (15). https://doi.org/10.1088/0953-8984/25/15/152101.

(30)   Lever, G.; Cole, D. J.; Lonsdale, R.; Ranaghan, K. E.; Wales, D. J.; Mulholland, A. J.; Skylaris,

C. K.; Payne, M. C. Large-Scale Density Functional Theory Transition State Searching in Enzymes. *J. Phys. Chem. Lett.* **2014**, *5* (21), 3614–3619. https://doi.org/10.1021/jz5018703.

(31)   Shuki, A. Empirical Valence Bond Simulations of Biological Systems. In *Theory and Applications of the Empirical Valence Bond Approach: From Physical Chemistry to Chemical Biology*; Duarte, F., Kamerlin, S. C. L., Eds.; John Wiley and Sons, Ltd., 2017; pp 145–172.

(32)   Kamerlin, S. C. L.; Warshel, A. The EVB as a Quantitative Tool for Formulating Simulations and Analyzing Biological and Chemical Reactions. *Faraday Discuss.* **2010**, *145*, 71–106. https://doi.org/10.1038/jid.2014.371.

(33)   Adamczyk, A. J.; Warshel, A. Converting Structural Information into an Allosteric-Energy-Based Picture for Elongation Factor Tu Activation by the Ribosome. *Proc. Natl. Acad. Sci. U. S. A.* **2011**, *108* (24), 9827–9832. https://doi.org/10.1073/pnas.1105714108.

(34)   Adamczyk, A. J.; Warshel, A. Converting Structural Information into an Allosteric-Energy-Based Picture for Elongation Factor Tu Activation by the Ribosome. In *243rd National Spring Meeting of the American Chemical Society*; San Diego, Ca, 2012.

(35)   Georgieva, P.; Himo, F. Quantum Chemical Modeling of Enzymatic Reactions: The Case of Histone Lysine Methyltransferase. *J. Comput. Chem.* **2010**, *31* (8), 1707–1714. https://doi.org/10.1002/jcc.21458.

(36)   Gomaa, A. M. Application of Enzymes in Brewing. *J. Nutr. Food Sci. Forecast* **2018**, *1* (1), 1–5.

(37)   Grand View Research. Enzymes Market Size & Share, Industry Analysis Report, 2019-2025 https://www.grandviewresearch.com/industry-analysis/enzymes-industry.

(38)   Schomburg, I.; Chang, A.; Placzek, S.; Söhngen, C.; Rother, M.; Lang, M.; Munaretto, C.; Ulas, S.; Stelzer, M.; Grote, A.; Scheer, M.; Schomburg, D. BRENDA in 2013: Integrated Reactions, Kinetic Data, Enzyme Function Data, Improved Disease Classification: New Options and Contents in BRENDA. *Nucleic Acids Res.* **2013**, *41* (D1), 764–772. https://doi.org/10.1093/nar/gks1049.

(39)   Recommendations of the Nomenclature Committee of the International Union of Biochemistry and Molecular Biology on the Nomenclature and Classification of Enzymes by the Reactions they Catalyse https://web.archive.org/web/20170711144836/http://www.chem.qmul.ac.uk/iubmb/enzyme/.

(40)   Grand View Research. *Enzymes Market*; 2018.

(41)   Warshel, A.; Sharma, P. K.; Kato, M.; Xiang, Y.; Liu, H.; Olsson, M. H. M. Electrostatic Basis for Enzyme Catalysis. *Chem. Rev.* **2006**, *106* (8), 3210–3235. https://doi.org/10.1021/cr0503106.

(42)   Jencks, W. P. *Catalysis in Chemistry and Enzymology*; Dover Publications, 1987.

(43)   Hur, S.; Bruice, T. C. Just a near Attack Conformer for Catalysis (Chorismate to Prephenate Rearrangements in Water, Antibody, Enzymes, and Their Mutants). *J. Am.*

Chem. Soc. **2003**, *125* (35), 10540–10542. https://doi.org/10.1021/ja0357846.

(44)   Hammes, G. G.; Benkovic, S. J.; Hammes-Schiffer, S. Flexibility, Diversity, and Cooperativity: Pillars of Enzyme Catalysis. *Biochemistry* **2011**, *50* (48), 10422–10430. https://doi.org/10.1021/bi201486f.

(45)   Benkovic, S. J.; Hammes-Schiffer, S. A Perspective on Enzyme Catalysis. *Science (80-.).* **2003**, *301* (5637), 1196–1202. https://doi.org/10.1126/science.1085515.

(46)   Hammes, G. G. Multiple Conformational Changes in Enzyme Catalysis. *Biochemistry* **2002**, *41* (26), 8221–8228. https://doi.org/10.1021/bi0260839.

(47)   Boyer, R. *Concepts in Biochemistry*, 2nd ed.; John Wiley & Sons, Inc., 2002.

(48)   Koshland, D. E. Application of a Theory of Enzyme Specificity to Protein Synthesis. *Proc. Natl. Acad. Sci.* **1958**, *44* (2), 98–104. https://doi.org/10.1073/pnas.44.2.98.

(49)   Amils, R.; Ellis-Evans, C.; Hinghofer-Szalkay, H. Life in Extreme Environments. *Life Extrem. Environ.* **2007**, *409* (September 2000), 1–450. https://doi.org/10.1007/978-1-4020-6285-8.

(50)   Canganella, F.; Wiegel, J. Extremophiles: From Abyssal to Terrestrial Ecosystems and Possibly Beyond. *Naturwissenschaften* **2011**, *98* (4), 253–279. https://doi.org/10.1007/s00114-011-0775-2.

(51)   Daniel, R. M.; Danson, M. J.; Eisenthal, R.; Lee, C. K.; Peterson, M. E. The Effect of Temperature on Enzyme Activity: New Insights and Their Implications. *Extremophiles* **2008**, *12* (1), 51–59. https://doi.org/10.1007/s00792-007-0089-7.

(52)   Somero, G. N. Adaptation of Enzymes to Temperature: Searching for Basic "Strategies." *Comp. Biochem. Physiol. - B Biochem. Mol. Biol.* **2004**, *139* (3 SPEC.ISS.), 321–333. https://doi.org/10.1016/j.cbpc.2004.05.003.

(53)   Trivedi, S.; Gehlot, H. S.; Rao, S. R. Protein Thermostability in Archaea and Eubacteria. *Genet. Mol. Res.* **2006**, *5* (4), 816–827.

(54)   Schiraldi, C.; De Rosa, M. The Production of Biocatalysts and Biomolecules from Extremophiles. *Trends Biotechnol.* **2002**, *20* (12), 515–521. https://doi.org/10.1016/S0167-7799(02)02073-5.

(55)   Jaenicke, R.; Böhm, G. The Stability of Proteins in Extreme Environments. *Curr. Opin. Struct. Biol.* **1998**, *8* (6), 738–748. https://doi.org/10.1016/S0959-440X(98)80094-8.

(56)   Fields, P. A.; Somero, G. N. Hot Spots in Cold Adaptation: Localized Increases in Conformational Flexibility in Lactate Dehydrogenase A4 Orthologs of Antarctic Notothenioid Fishes. *Proc. Natl. Acad. Sci. U. S. A.* **1998**, *95* (19), 11476–11481. https://doi.org/10.1073/pnas.95.19.11476.

(57)   Warshel, A.; Russell, S. T. Calculations of Electrostatic Interactions in Biological Systems and in Solutions. *Q. Rev. Biophys.* **1984**, *17* (3), 283–422. https://doi.org/10.1017/S0033583500005333.

(58)   Anwar, A.; Saleemuddin, M. Alkaline Proteases: A Review. *Bioresour. Technol.* **1998**, *64* (3), 175–183. https://doi.org/10.1016/S0960-8524(97)00182-X.

(59)   Heinrich, M. R. Solvent Effects on Enzymes: Implications for Extraterrestrial Life. In *Molecular Evolution: Prebiological and Biological*; Rohlfing, D. L., Oparin, A. I., Eds.; Plenum Press, 1972; pp 331–342. https://doi.org/https://doi.org/10.1007/978-1-4684-2019-7.

(60)   Wiggers, H. J.; Cheleski, J.; Zottis, A.; Oliva, G.; Andricopulo, A. D.; Montanari, C. A. Effects of Organic Solvents on the Enzyme Activity of Trypanosoma Cruzi Glyceraldehyde-3-Phosphate Dehydrogenase in Calorimetric Assays. *Anal. Biochem.* **2007**, *370* (1), 107–114. https://doi.org/10.1016/j.ab.2007.06.042.

(61)   Chatzikonstantinou, A. V.; Norra, G. F.; Stamatis, H.; Voutsas, E. Prediction of Solvent Effect on Enzyme Enantioselectivity. *Fluid Phase Equilib.* **2017**, *450*, 126–132. https://doi.org/10.1016/j.fluid.2017.07.016.

(62)   Hedstrom, L. Serine Protease Mechanism and Specificity. *Chem. Rev.* **2002**, *102* (12), 4501–4523. https://doi.org/10.1021/cr000033x.

(63)   Neitzel, J. J. Enzyme Catalysis: The Serine Proteases https://www.nature.com/scitable/topicpage/enzyme-catalysis-the-serine-proteases-nbsp-14398894/.

(64)   Gudmundsdóttir, Á.; Pálsdóttir, H. M. Atlantic Cod Trypsins: From Basic Research to Practical Applications. *Mar. Biotechnol.* **2005**, *7* (2), 77–88. https://doi.org/10.1007/s10126-004-0061-9.

(65)   Chelulei Cheison, S.; Brand, J.; Leeb, E.; Kulozik, U. Analysis of the Effect of Temperature Changes Combined with Different Alkaline PH on the β-Lactoglobulin Trypsin Hydrolysis Pattern Using MALDI-TOF-MS/MS. *J. Agric. Food Chem.* **2011**, *59* (5), 1572–1581. https://doi.org/10.1021/jf1039876.

(66)   Sundus, H.; Mukhtar, H.; Nawaz, A. Industrial Applications and Production Sources of Serine Alkaline Proteases: A Review. *J. Bacteriol. Mycol. Open Access* **2016**, *3* (1), 191–194. https://doi.org/10.15406/jbmoa.2016.03.00051.

(67)   Salwan, R.; Sharma, V. Trends in Extracellular Serine Proteases of Bacteria as Detergent Bioadditive: Alternate and Environmental Friendly Tool for Detergent Industry. *Arch. Microbiol.* **2019**, *201* (7), 863–877. https://doi.org/10.1007/s00203-019-01662-8.

(68)   Contesini, F. J.; Melo, R. R. de; Sato, H. H. An Overview of Bacillus Proteases: From Production to Application. *Crit. Rev. Biotechnol.* **2018**, *38* (3), 321–334. https://doi.org/10.1080/07388551.2017.1354354.

(69)   Craik, C. S.; Page, M. J.; Madison, E. L. Proteases as Therapeutics HHS Public Access. **2011**, *435* (1), 1–16. https://doi.org/10.1042/BJ20100965.

(70)   Madala, P. K.; Tyndall, J. D. A.; Nall, T.; Fairlie, D. P. Update 1 of: Proteases Universally Recognize Beta Strands in Their Active Sites. *Chem. Rev.* **2010**, *110* (6), PR1–PR31. https://doi.org/10.1021/cr900368a.

(71)   Yon-Kahn, J.; Hervé, G. *Molecular and Cellular Enzymology*; Springer, 2010. https://doi.org/https://doi.org/10.1007/978-3-642-01228-0.

(72)   Craik, C. S.; Roczniak, S.; Largman, C.; Rutter, W. J. The Catalytic Role of the Active Site

Aspartic Acid in Serine Proteases. *Science (80-.).* **1987**, *237* (4817), 909–913. https://doi.org/10.1126/science.3303334.

(73) Kraut, J. Serine Proteases: Structure and Mechanism of Catalysis. *Annu. Rev. Biochem.* **1977**, *46* (1), 331–358. https://doi.org/10.1146/annurev.bi.46.070177.001555.

(74) Radisky, E. S.; Lee, J. M.; Lu, C. J. K.; Koshland, D. E. Insights into the Serine Protease Mechanism from Atomic Resolution Structures of Trypsin Reaction Intermediates. *Proc. Natl. Acad. Sci. U. S. A.* **2006**, *103* (18), 6835–6840. https://doi.org/10.1073/pnas.0601910103.

(75) Ishida, T.; Kato, S. Theoretical Perspectives on the Reaction Mechanism of Serine Proteases: The Reaction Free Energy Profiles of the Acylation Process. *J. Am. Chem. Soc.* **2003**, *125* (39), 12035–12048. https://doi.org/10.1021/ja021369m.

(76) Topf, M.; Richards, W. G. Theoretical Studies on the Deacylation Step of Serine Protease Catalysis in the Gas Phase, in Solution, and in Elastase. *J. Am. Chem. Soc.* **2004**, *126* (44), 14631–14641. https://doi.org/10.1021/ja047010a.

(77) Topf, M.; Várnai, P.; Schofield, C. J.; Richards, W. G. Molecular Dynamics Simulations of the Acyl-Enzyme and the Tetrahedral Intermediate in the Deacylation Step of Serine Proteases. *Proteins Struct. Funct. Genet.* **2002**, *47* (3), 357–369. https://doi.org/10.1002/prot.10097.

(78) Scheiner, S. Analysis of Catalytic Mechanism of Serine Proteases. Viability of the Ring-Flip Hypothesis. *J. Phys. Chem. B* **2008**, *112* (22), 6837–6846. https://doi.org/10.1021/jp710617w.

(79) Emsley, J. Very Strong Hydrogen Bonding. *Chem. Soc. Rev.* **1980**, *9* (1), 91–124. https://doi.org/10.1039/CS9800900091.

(80) Larson, J. W.; McMahon, T. B. Gas-Phase Bihalide and Pseudobihalide Ions. An Ion Cyclotron Resonance Determination of Hydrogen Bond Energies in XHY- Species (X, Y = F, Cl, Br, CN). *Inorg. Chem.* **1984**, *23* (14), 2029–2033. https://doi.org/10.1021/ic00182a010.

(81) Naray-Szabo, G.; Warshel, A.; Sussman, F.; Hwang, J. K. How Do Serine Proteases Really Work? *Biochemistry* **1989**, *28* (9), 3629–3637. https://doi.org/10.1021/bi00435a001.

(82) Agmon, N. The Grotthuss Mechanism. *Chem. Phys. Lett.* **1995**, *244* (5–6), 456–462. https://doi.org/10.1016/0009-2614(95)00905-J.

(83) Kohn, W.; Sham, L. J. Self-Consistent Equations Including Exchange and Correlation Effects. *Phys. Rev.* **1965**, *140* (4A), 1133–1136. https://doi.org/10.1103/PhysRev.140.A1133.

(84) Frisch, M. J.; Trucks, G. W.; Schlegel, H. B.; Scuseria, G. E.; Robb, M. A.; Cheeseman, J. R.; Scalmani, G.; Barone, V.; Petersson, G. A.; Nakatsuji, H.; Li, X.; Caricato, M.; Marenich, A. V.; Bloino, J.; Janesko, B. G.; Gomperts, R.; Mennucci, B.; Hratchian, H. P.; Ortiz, J. V.; Izmaylov, A. F.; Sonnenberg, J. L.; Williams; Ding, F.; Lipparini, F.; Egidi, F.; Goings, J.; Peng, B.; Petrone, A.; Henderson, T.; Ranasinghe, D.; Zakrzewski, V. G.; Gao, J.; Rega, N.; Zheng, G.; Liang, W.; Hada, M.; Ehara, M.; Toyota, K.; Fukuda, R.; Hasegawa, J.; Ishida, M.; Nakajima, T.; Honda, Y.; Kitao, O.; Nakai, H.; Vreven, T.; Throssell, K.; Montgomery Jr.,

J. A.; Peralta, J. E.; Ogliaro, F.; Bearpark, M. J.; Heyd, J. J.; Brothers, E. N.; Kudin, K. N.; Staroverov, V. N.; Keith, T. A.; Kobayashi, R.; Normand, J.; Raghavachari, K.; Rendell, A. P.; Burant, J. C.; Iyengar, S. S.; Tomasi, J.; Cossi, M.; Millam, J. M.; Klene, M.; Adamo, C.; Cammi, R.; Ochterski, J. W.; Martin, R. L.; Morokuma, K.; Farkas, O.; Foresman, J. B.; Fox, D. J. Gaussian 16 Rev. C.01. Wallingford, CT 2016.

(85)   Langreth, D. C.; Mehl, M. J. Beyond the Local-Density Approximation in Calculations of Ground-State Electronic Properties. *Phys. Rev. B* **1983**, *28* (4), 1809–1834. https://doi.org/10.1103/PhysRevB.28.1809.

(86)   Grimme, S. Semiempirical Hybrid Density Functional with Perturbative Second-Order Correlation. *J. Chem. Phys.* **2006**, *124* (3), 1–16. https://doi.org/10.1063/1.2148954.

(87)   Andzelm, J.; Kölmel, C.; Klamt, A. Incorporation of Solvent Effects into Density Functional Calculations of Molecular Energies and Geometries. *J. Chem. Phys.* **1995**, *103* (21), 9312–9320. https://doi.org/10.1063/1.469990.

(88)   Grimme, S.; Antony, J.; Ehrlich, S.; Krieg, H. A Consistent and Accurate Ab Initio Parametrization of Density Functional Dispersion Correction (DFT-D) for the 94 Elements H-Pu. *J. Chem. Phys.* **2010**, *132* (15). https://doi.org/10.1063/1.3382344.

(89)   Hohenberg, P.; Kohn, W. Inhomogenous Electron Gas. *Phys. Rev.* **1964**, *136* (3B), 391–402. https://doi.org/10.1103/PhysRev.136.B864.

(90)   Jensen, F. *Introduction to Computational Chemistry*, 3rd ed.; John Wiley and Sons, Ltd., 2017.

(91)   Elsässer, B.; Goettig, P. Mechanisms of Proteolytic Enzymes and Their Inhibition in QM/MM Studies. *Int. J. Mol. Sci.* **2021**, *22* (6), 1–26. https://doi.org/10.3390/ijms22063232.

(92)   Ali, A.; Adamczyk, A. J. Reaction Pathway Analysis of Serine Protease with QM Cluster Study. *Phys. Chem. Chem. Phys.*

(93)   Grand View Research. Hydrogen Generation Market Size, Share & Trends Analysis Report By Application (Coal Gasification, Steam Methane Reforming), By Systems (Merchant, Captive), By Technology, And Segment Forecasts, 2020 - 2027 https://www.grandviewresearch.com/industry-analysis/hydrogen-generation-market.

(94)   Voldsund, M.; Jordal, K.; Anantharaman, R. Hydrogen Production with CO2 Capture. *Int. J. Hydrogen Energy* **2016**, *41* (9), 4969–4992. https://doi.org/10.1016/j.ijhydene.2016.01.009.

(95)   Zou, X.; Zhang, Y. Noble Metal-Free Hydrogen Evolution Catalysts for Water Splitting. *Chem. Soc. Rev.* **2015**, *44* (15), 5148–5180. https://doi.org/10.1039/c4cs00448e.

(96)   Ohta, T. Thermodynamics of Water-Splitting. In *Solar-Hydrogen Energy Systems An Authoritative Review of Water-splitting Systems by Solar Beam and Solar Heat: Hydrogen Production, Storage and Utilisation*; Ohta, T., Ed.; Pergamon Press, 1979; pp 25–33. https://doi.org/10.1016/B978-0-08-022713-9.50008-2.

(97)   Millet, P. Fundamentals of Water Electrolysis. In *Hydrogen Production by Electrolysis*; Godula-Jopek, A., Ed.; Wiley-VCH Verlag GmbH & Co. KGaA, 2015; pp 33–61.

(98)   *Electrochemical Dictionary*, 2nd ed.; Bard, A. J., Inzelt, G., Scholz, F., Eds.; Springer Berlin Heidelberg, 2012. https://doi.org/10.1007/978-3-642-29551-5.

(99)   *Hydrogen Production by Electrolysis*; Godula-Jopek, A., Ed.; Wiley-VCH Verlag GmbH & Co. KGaA, 2015.

(100)   Durst, J.; Siebel, A.; Simon, C.; Hasché, F.; Herranz, J.; Gasteiger, H. A. New Insights into the Electrochemical Hydrogen Oxidation and Evolution Reaction Mechanism. *Energy Environ. Sci.* **2014**, *7* (7), 2255–2260. https://doi.org/10.1039/c4ee00440j.

(101)   Liao, T.; Sun, Z.; Sun, C.; Dou, S. X.; Searles, D. J. Electronic Coupling and Catalytic Effect on H2 Evolution of MoS2/Graphene Nanocatalyst. *Sci. Rep.* **2014**, *4*, 1–7. https://doi.org/10.1038/srep06256.

(102)   Kibler, L. A. Hydrogen Electrocatalysis. *ChemPhysChem* **2006**, *7* (5), 985–991. https://doi.org/10.1002/cphc.200500646.

(103)   Despic, A. R. Deposition and Dissolution of Metals and Alloys. Part B: Mechanisms, Kinetics, Texture, and Morphology. In *Comprehensive Treatise of Electrochemistry, Volume 7 Kinetics and Mechanisms of Electrode Processes*; Bockris, J. O., Yeager, E., Khan, S. U. M., White, R. E., Eds.; Plenum Press, 1983; pp 451–528. https://doi.org/10.1007/978-1-4613-3584-9.

(104)   Bockris, J. O.; Nagy, Z. Symmetry Factor and Transfer Coefficient: A Source of Confusion in Electrode Kinetics. *J. Chem. Educ.* **1973**, *50* (12), 839–843. https://doi.org/10.1021/ed050p839.

(105)   Vetter, K. J. *Electrochemical Kinetics: Theoretical and Experimental Aspects*, 1st ed.; Academic Press Inc., 1967.

(106)   Alonso-Vante, N.; Roldán, C. A. C.; de Guadalupe González Huerta, R.; Sánchez, G. R.; Robledo, A. M. *Fundamentals of Electrocatalyst Materials and Interfacial*; Scrivener Publishing LLC, 2019.

(107)   Quaino, P.; Juarez, F.; Santos, E.; Schmickler, W. Volcano Plots in Hydrogen Electrocatalysis - Uses and Abuses. *Beilstein J. Nanotechnol.* **2014**, *5* (1), 846–854. https://doi.org/10.3762/bjnano.5.96.

(108)   Esposito, D. V.; Hunt, S. T.; Stottlemyer, A. L.; Dobson, K. D.; McCandless, B. E.; Birkmire, R. W.; Chen, J. G. Low-Cost Hydrogen-Evolution Catalysts Based on Monolayer Platinum on Tungsten Monocarbide Substrates. *Angew. Chemie - Int. Ed.* **2010**, *49* (51), 9859–9862. https://doi.org/10.1002/anie.201004718.

(109)   Dubouis, N.; Grimaud, A. The Hydrogen Evolution Reaction: From Material to Interfacial Descriptors. *Chem. Sci.* **2019**, 9165–9181. https://doi.org/10.1039/c9sc03831k.

(110)   Nørskov, J. K.; Bligaard, T.; Logadottir, A.; Kitchin, J. R.; Chen, J. G.; Pandelov, S.; Stimming, U. Trends in the Exchange Current for Hydrogen Evolution. *J. Electrochem. Soc.* **2005**, *152* (3), J23–J26. https://doi.org/10.1149/1.1856988.

(111)   Greeley, J.; Jaramillo, T. F.; Bonde, J.; Chorkendorff, I. B.; Nørskov, J. K. Computational High-Throughput Screening of Electrocatalytic Materials for Hydrogen Evolution. *Nat. Mater.* **2006**, *5* (11), 909–913. https://doi.org/10.1038/nmat1752.

(112) Wang, M.; Chen, L.; Sun, L. Recent Progress in Electrochemical Hydrogen Production with Earth-Abundant Metal Complexes as Catalysts. *Energy Environ. Sci.* **2012**, *5* (5), 6763–6778. https://doi.org/10.1039/c2ee03309g.

(113) Miles, M. H. Periodic Variations of Overvoltages for Water Electrolysis in Acid Solutions from Cyclic Voltammetric Studies. *J. Electrochem. Soc.* **1976**, *123* (10), 1459. https://doi.org/10.1149/1.2132619.

(114) Faber, M. S.; Lukowski, M. A.; Ding, Q.; Kaiser, N. S.; Jin, S. Earth-Abundant Metal Pyrites (FeS2, CoS2, NiS2, and Their Alloys) for Highly Efficient Hydrogen Evolution and Polysulfide Reduction Electrocatalysis. *J. Phys. Chem. C* **2014**, *118* (37), 21347–21356. https://doi.org/10.1021/jp506288w.

(115) Hinnemann, B.; Moses, P. G.; Bonde, J.; Jørgensen, K. P.; Nielsen, J. H.; Horch, S.; Chorkendorff, I.; Nørskov, J. K. Biomimetic Hydrogen Evolution: MoS2 Nanoparticles as Catalyst for Hydrogen Evolution. *J. Am. Chem. Soc.* **2005**, *127* (15), 5308–5309. https://doi.org/10.1021/ja0504690.

(116) Putungan, D. B.; Lin, S. H.; Kuo, J. L. A First-Principles Examination of Conducting Monolayer 1T '-MX2 (M = Mo, W; X = S, Se, Te): Promising Catalysts for Hydrogen Evolution Reaction and Its Enhancement by Strain. *Phys. Chem. Chem. Phys.* **2015**, *17* (33), 21702–21708. https://doi.org/10.1039/c5cp03799a.

(117) Yun, W. S.; Han, S. W.; Hong, S. C.; Kim, I. G.; Lee, J. D. Thickness and Strain Effects on Electronic Structures of Transition Metal Dichalcogenides: 2H-MX 2 Semiconductors (M = Mo, W; X = S, Se, Te). *Phys. Rev. B - Condens. Matter Mater. Phys.* **2012**, *85* (3), 1–5. https://doi.org/10.1103/PhysRevB.85.033305.

(118) Ruppert, C.; Aslan, O. B.; Heinz, T. F. Optical Properties and Band Gap of Single- and Few-Layer MoTe2 Crystals. *Nano Lett.* **2014**, *14* (11), 6231–6236. https://doi.org/10.1021/nl502557g.

(119) Seo, B.; Jung, G. Y.; Sa, Y. J.; Jeong, H. Y.; Cheon, J. Y.; Lee, J. H.; Kim, H. Y.; Kim, J. C.; Shin, H. S.; Kwak, S. K.; Joo, S. H. Monolayer-Precision Synthesis of Molybdenum Sulfide Nanoparticles and Their Nanoscale Size Effects in the Hydrogen Evolution Reaction. *ACS Nano* **2015**, *9* (4), 3728–3739. https://doi.org/10.1021/acsnano.5b00786.

(120) Lukowski, M. A.; Daniel, A. S.; Meng, F.; Forticaux, A.; Li, L.; Jin, S. Enhanced Hydrogen Evolution Catalysis from Chemically Exfoliated Metallic MoS2 Nanosheets. *J. Am. Chem. Soc.* **2013**, *135* (28), 10274–10277. https://doi.org/10.1021/ja404523s.

(121) Voiry, D.; Salehi, M.; Silva, R.; Fujita, T.; Chen, M.; Asefa, T.; Shenoy, V. B.; Eda, G.; Chhowalla, M. Conducting MoS2 Nanosheets as Catalysts for Hydrogen Evolution Reaction. *Nano Lett.* **2013**, *13* (12), 6222–6227. https://doi.org/10.1021/nl403661s.

(122) Wu, Z.; Fang, B.; Wang, Z.; Wang, C.; Liu, Z.; Liu, F.; Wang, W.; Alfantazi, A.; Wang, D.; Wilkinson, D. P. MoS2 Nanosheets: A Designed Structure with High Active Site Density for the Hydrogen Evolution Reaction. *ACS Catal.* **2013**, *3* (9), 2101–2107. https://doi.org/10.1021/cs400384h.

(123) Guo, B.; Yu, K.; Li, H.; Song, H.; Zhang, Y.; Lei, X.; Fu, H.; Tan, Y.; Zhu, Z. Hollow Structured Micro/Nano MoS2 Spheres for High Electrocatalytic Activity Hydrogen Evolution

Reaction. *ACS Appl. Mater. Interfaces* **2016**, *8* (8), 5517–5525. https://doi.org/10.1021/acsami.5b10252.

(124) Ye, G.; Gong, Y.; Lin, J.; Li, B.; He, Y.; Pantelides, S. T.; Zhou, W.; Vajtai, R.; Ajayan, P. M. Defects Engineered Monolayer MoS2 for Improved Hydrogen Evolution Reaction. *Nano Lett.* **2016**, *16* (2), 1097–1103. https://doi.org/10.1021/acs.nanolett.5b04331.

(125) Lightcap, I. V.; Kosel, T. H.; Kamat, P. V. Anchoring Semiconductor and Metal Nanoparticles on a Two-Dimensional Catalyst Mat. Storing and Shuttling Electrons with Reduced Graphene Oxide. *Nano Lett.* **2010**, *10* (2), 577–583. https://doi.org/10.1021/nl9035109.

(126) Kamat, P. V. Graphene-Based Nanoarchitectures. Anchoring Semiconductor and Metal Nanoparticles on a Two-Dimensional Carbon Support. *J. Phys. Chem. Lett.* **2010**, *1* (2), 520–527. https://doi.org/10.1021/jz900265j.

(127) Li, Y.; Wang, H.; Xie, L.; Liang, Y.; Hong, G.; Dai, H. MoS2 Nanoparticles Grown on Graphene: An Advanced Catalyst for the Hydrogen Evolution Reaction. *J. Am. Chem. Soc.* **2011**, *133* (19), 7296–7299. https://doi.org/10.1021/ja201269b.

(128) Wang, H.; Tran, D.; Qian, J.; Ding, F.; Losic, D. MoS2/Graphene Composites as Promising Materials for Energy Storage and Conversion Applications. *Adv. Mater. Interfaces* **2019**, *6* (20), 1900915 (1-23). https://doi.org/10.1002/admi.201900915.

(129) Sarker, S.; Peters, J.; Chen, X.; Li, B.; Chen, G.; Yan, L.; Richins, S. K.; Das, S.; Zhou, M.; Luo, H. Engineering Molybdenum Diselenide and Its Reduced Graphene Oxide Hybrids for Efficient Electrocatalytic Hydrogen Evolution. *ACS Appl. Nano Mater.* **2018**, *1* (5), 2143–2152. https://doi.org/10.1021/acsanm.8b00208.

(130) Tang, H.; Dou, K.; Kaun, C. C.; Kuang, Q.; Yang, S. MoSe2 Nanosheets and Their Graphene Hybrids: Synthesis, Characterization and Hydrogen Evolution Reaction Studies. *J. Mater. Chem. A* **2014**, *2* (2), 360–364. https://doi.org/10.1039/c3ta13584e.

(131) Parsons, R. The Rate of Electrolytic Hydrogen Evolution and the Heat of Adsorption of Hydrogen. *Trans. Faraday Soc.* **1958**, *54* (7), 1053–1063. https://doi.org/10.1039/tf9585401053.

(132) Gerischer, H. Mechanismus Der Elektrolytischen Wasserstoffabscheidung Und Adsorptionsenergie von Atomarem Wasserstoff. *Bull. des Sociétés Chim. Belges* **1958**, *67* (7–8), 506–527. https://doi.org/10.1002/bscb.19580670714.

(133) Jaramillo, T. F.; Jørgensen, K. P.; Bonde, J.; Nielsen, J. H.; Horch, S.; Chorkendorff, I. Identification of Active Edge Sites for Electrochemical H2 Evolution from MoS2 Nanocatalysts. *Science (80-.).* **2007**, *317* (5834), 100–102. https://doi.org/10.1126/science.1141483.

(134) Clark, S. J.; Segall, M. D.; Pickard, C. J.; Hasnip, P. J.; Probert, M. I. J.; Refson, K.; Payne, M. C. First Principles Methods Using CASTEP. *Zeitschrift für Krist.* **2005**, *220* (5–6), 567–570. https://doi.org/10.1524/zkri.220.5.567.65075.

(135) Perdew, J. P.; Burke, K.; Ernzerhof, M. Generalized Gradient Approximation Made Simple. *Phys. Rev. Lett.* **1996**, *77* (18), 3865–3868. https://doi.org/10.1103/PhysRevLett.77.3865.

(136) Vanderbilt, D. Soft Self-Consistent Pseudopotentials in a Generalized Eigenvalue Formalism. *Phys. Rev. B* **1990**, *41* (11), 7892–7895. https://doi.org/10.1103/PhysRevB.41.7892.

(137) Barzilai, J. Two-Point Step Size Gradient Methods.Pdf. *IMA J. Numer. Anal.* **1988**, *8* (1), 141–148. https://doi.org/10.1093/imanum/8.1.141.

(138) Neugebauer, J.; Scheffler, M. Adsorbate-Substrate and Adsorbate-Adsorbate Interactions of Na and K Adlayers on Al(111). *Phys. Rev. B* **1992**, *46* (24), 16067–16080. https://doi.org/10.1103/PhysRevB.46.16067.

(139) Koelling, D. D.; Harmon, B. N. A Technique for Relativistic Spin-Polarised Calculations. *J. Phys. C Solid State Phys.* **1977**, *10* (16), 3107–3114. https://doi.org/10.1088/0022-3719/10/16/019.

(140) Pack, J. D.; Monkhorst, H. J. Special Points for Brillouin-Zone Integration. *Phys. Rev. B* **1976**, *13* (12), 5188–5192. https://doi.org/10.1103/PhysRevB.13.5188.

(141) Dehghanimadvar, M.; Shirmohammadi, R.; Sadeghzadeh, M.; Aslani, A.; Ghasempour, R. Hydrogen Production Technologies: Attractiveness and Future Perspective. *Int. J. Energy Res.* **2020**, *44* (11), 8233–8254. https://doi.org/10.1002/er.5508.

(142) International Energy Agency. *The Future of Hydrogen: Seizing Today's Opportunities*; 2019.

(143) Committee on Climate Change. Hydrogen in a Low-Carbon Economy. **2018**, No. November, 1–128.

(144) Newborough, M.; Cooley, G. Developments in the Global Hydrogen Market: The Spectrum of Hydrogen Colours. *Fuel Cells Bull.* **2020**, *2020* (11), 16–22. https://doi.org/10.1016/S1464-2859(20)30546-0.

(145) Jaramillo, T. F.; Jørgensen, K. P.; Bonde, J.; Nielsen, J. H.; Horch, S.; Chorkendorff, I. Identification of Active Edge Sites for Electrochemical H_2 Evolution from MoS_2 Nanocatalysts. *Science (80-.).* **2007**, *317* (5834), 100–102. https://doi.org/10.1126/science.1141483.

(146) Gudmundsdóttir, S.; Skúlason, E.; Weststrate, K. J.; Juurlink, L.; Jónsson, H. Hydrogen Adsorption and Desorption at the Pt(110)-(1×2) Surface: Experimental and Theoretical Study. *Phys. Chem. Chem. Phys.* **2013**, *15* (17), 6323–6332. https://doi.org/10.1039/c3cp44503h.

(147) Greeley, J.; Nørskov, J. K. Large-Scale, Density Functional Theory-Based Screening of Alloys for Hydrogen Evolution. *Surf. Sci.* **2007**, *601* (6), 1590–1598. https://doi.org/10.1016/j.susc.2007.01.037.

(148) Greeley, J.; Nørskov, J. K.; Kibler, L. A.; El-Aziz, A. M.; Kolb, D. M. Hydrogen Evolution over Bimetallic Systems: Understanding the Trends. *ChemPhysChem* **2006**, *7* (5), 1032–1035. https://doi.org/10.1002/cphc.200500663.

(149) Yang, B.; Xu, J.; Bin, D.; Wang, J.; Zhao, J.; Liu, Y.; Li, B.; Fang, X.; Liu, Y.; Qiao, L.; Liu, L.; Liu, B. Amorphous Phosphatized Ruthenium-Iron Bimetallic Nanoclusters with Pt-like Activity for Hydrogen Evolution Reaction. *Appl. Catal. B Environ.* **2021**, *283* (September

2020), 119583. https://doi.org/10.1016/j.apcatb.2020.119583.

(150)   Wu, T.; Hong, J.; Lu, Z.; Wu, H.; Wu, C.; Tang, Z.; Liu, X.; Zeng, B.; Xu, Y.; Chen, G.; Yuan, C.; Dai, L. In-Situ Generation of Ru-Catechol Coordinative Polymer Precursor for High-Performance Hydrogen Evolution Reaction Doped Carbon Catalyst. *Appl. Catal. B Environ.* **2021**, *285* (September 2020), 119795. https://doi.org/10.1016/j.apcatb.2020.119795.

(151)   Wang, Z. J.; Li, M. X.; Yu, J. H.; Ge, X. B.; Liu, Y. H.; Wang, W. H. Low-Iridium-Content IrNiTa Metallic Glass Films as Intrinsically Active Catalysts for Hydrogen Evolution Reaction. *Adv. Mater.* **2020**, *32* (4), 1–7. https://doi.org/10.1002/adma.201906384.

(152)   Zhu, J.; Cai, L.; Yin, X.; Wang, Z.; Zhang, L.; Ma, H.; Ke, Y.; Du, Y.; Xi, S.; Wee, A. T. S.; Chai, Y.; Zhang, W. Enhanced Electrocatalytic Hydrogen Evolution Activity in Single-Atom Pt-Decorated VS2 Nanosheets. *ACS Nano* **2020**, *14* (5), 5600–5608. https://doi.org/10.1021/acsnano.9b10048.

(153)   Wang, X.; Shen, X.; Wang, Z.; Yu, R.; Chen, L. Atomic-Scale Clarification of Structural Transition of MoS2 upon Sodium Intercalation. *ACS Nano* **2014**, *8* (11), 11394–11400. https://doi.org/10.1021/nn505501v.

(154)   Tang, Q.; Jiang, D. E. Mechanism of Hydrogen Evolution Reaction on 1T-MoS2 from First Principles. *ACS Catal.* **2016**, *6* (8), 4953–4961. https://doi.org/10.1021/acscatal.6b01211.

(155)   Liu, M.; Wang, Z.; Liu, J.; Wei, G.; Du, J.; Li, Y.; An, C.; Zhang, J. Synthesis of Few-Layer 1T'-MoTe2 Ultrathin Nanosheets for High-Performance Pseudocapacitors. *J. Mater. Chem. A* **2017**, *5*, 1035–1042. https://doi.org/10.1039/c6ta08206h.

(156)   Wang, R.; Li, X.; Gao, T.; Yao, T.; Liu, S.; Wang, X.; Han, J.; Zhang, P.; Cao, X.; Zhang, X.; Zhang, Y.; Song, B. Beyond 1T-Phase? Synergistic Electronic Structure and Defects Engineering in 2H-MoS2xSe2(1-x) Nanosheets for Enhanced Hydrogen Evolution Reaction and Sodium Storage. *ChemCatChem* **2019**, *11* (14), 3200–3211. https://doi.org/10.1002/cctc.201900682.

(157)   Lin, L.; Miao, N.; Wen, Y.; Zhang, S.; Ghosez, P.; Sun, Z.; Allwood, D. A. Sulfur-Depleted Monolayered Molybdenum Disulfide Nanocrystals for Superelectrochemical Hydrogen Evolution Reaction. *ACS Nano* **2016**, *10* (9), 8929–8937. https://doi.org/10.1021/acsnano.6b04904.

(158)   Vrubel, H.; Moehl, T.; Grätzel, M.; Hu, X. Revealing and Accelerating Slow Electron Transport in Amorphous Molybdenum Sulphide Particles for Hydrogen Evolution Reaction. *Chem. Commun.* **2013**, *49* (79), 8985–8987. https://doi.org/10.1039/c3cc45416a.

(159)   Sarwar, S.; Ali, A.; Liu, Z.; Li, J.; Uprety, S.; Lee, H.; Wang, R.; Park, M.; Bozack, M. J.; Adamczyk, A. J.; Zhang, X. Towards Thermoneutral Hydrogen Evolution Reaction Using Noble Metal Free Molybdenum Ditelluride/Graphene Nanocomposites. *J. Colloid Interface Sci.* **2020**, *581* (Pt B), 847–859. https://doi.org/10.1016/j.jcis.2020.07.122.

(160)   Escalera-López, D.; Niu, Y.; Yin, J.; Cooke, K.; Rees, N. V.; Palmer, R. E. Enhancement of the Hydrogen Evolution Reaction from Ni-MoS2 Hybrid Nanoclusters. *ACS Catal.* **2016**, *6* (9), 6008–6017. https://doi.org/10.1021/acscatal.6b01274.

(161)   Dai, X.; Du, K.; Li, Z.; Liu, M.; Ma, Y.; Sun, H.; Zhang, X.; Yang, Y. Co-Doped MoS2

Nanosheets with the Dominant CoMoS Phase Coated on Carbon as an Excellent Electrocatalyst for Hydrogen Evolution. *ACS Appl. Mater. Interfaces* **2015**, *7* (49), 27242–27253. https://doi.org/10.1021/acsami.5b08420.

(162) Staszak-Jirkovský, J.; Malliakas, C. D.; Lopes, P. P.; Danilovic, N.; Kota, S. S.; Chang, K. C.; Genorio, B.; Strmcnik, D.; Stamenkovic, V. R.; Kanatzidis, M. G.; Markovic, N. M. Design of Active and Stable Co-Mo-Sx Chalcogels as PH-Universal Catalysts for the Hydrogen Evolution Reaction. *Nat. Mater.* **2016**, *15* (2), 197–203. https://doi.org/10.1038/nmat4481.

(163) Zang, X.; Qin, Y.; Wang, T.; Li, F.; Shao, Q.; Cao, N. 1T/2H Mixed Phase MoS2Nanosheets Integrated by a 3D Nitrogen-Doped Graphene Derivative for Enhanced Electrocatalytic Hydrogen Evolution. *ACS Appl. Mater. Interfaces* **2020**, *12* (50), 55884–55893. https://doi.org/10.1021/acsami.0c16537.

(164) Dong, H.; Liu, C.; Ye, H.; Hu, L.; Fugetsu, B.; Dai, W.; Cao, Y.; Qi, X.; Lu, H.; Zhang, X. Three-Dimensional Nitrogen-Doped Graphene Supported Molybdenum Disulfide Nanoparticles as an Advanced Catalyst for Hydrogen Evolution Reaction. *Sci. Rep.* **2015**, *5* (174), 2–11. https://doi.org/10.1038/srep17542.

(165) Deng, J.; Li, H.; Xiao, J.; Tu, Y.; Deng, D.; Yang, H.; Tian, H.; Li, J.; Ren, P.; Bao, X. Triggering the Electrocatalytic Hydrogen Evolution Activity of the Inert Two-Dimensional MoS2 Surface via Single-Atom Metal Doping. *Energy Environ. Sci.* **2015**, *8* (5), 1594–1601. https://doi.org/10.1039/c5ee00751h.

(166) Zhao, H.; Li, Z.; Dai, X.; Cui, M.; Nie, F.; Zhang, X.; Ren, Z.; Yang, Z.; Gan, Y.; Yin, X.; Wang, Y.; Song, W. Heterostructured CoP/MoO2 on Mo Foil as High-Efficiency Electrocatalysts for the Hydrogen Evolution Reaction in Both Acidic and Alkaline Media. *J. Mater. Chem. A* **2020**, *8* (14), 6732–6739. https://doi.org/10.1039/c9ta13553g.

(167) Lu, K.; Liu, Y.; Lin, F.; Cordova, I. A.; Gao, S.; Li, B.; Peng, B.; Xu, H.; Kaelin, J.; Coliz, D.; Wang, C.; Shao, Y.; Cheng, Y. LixNiO/Ni Heterostructure with Strong Basic Lattice Oxygen Enables Electrocatalytic Hydrogen Evolution with Pt-like Activity. *J. Am. Chem. Soc.* **2020**, *142* (29), 12613–12619. https://doi.org/10.1021/jacs.0c00241.

(168) Li, S.; Zang, W.; Liu, X.; Pennycook, S. J.; Kou, Z.; Yang, C.; Guan, C.; Wang, J. Heterojunction Engineering of MoSe2/MoS2 with Electronic Modulation towards Synergetic Hydrogen Evolution Reaction and Supercapacitance Performance. *Chem. Eng. J.* **2019**, *359* (November 2018), 1419–1426. https://doi.org/10.1016/j.cej.2018.11.036.

(169) Kosmala, T.; Coy Diaz, H.; Komsa, H. P.; Ma, Y.; Krasheninnikov, A. V.; Batzill, M.; Agnoli, S. Metallic Twin Boundaries Boost the Hydrogen Evolution Reaction on the Basal Plane of Molybdenum Selenotellurides. *Adv. Energy Mater.* **2018**, *8* (20), 1–8. https://doi.org/10.1002/aenm.201800031.

(170) Gong, Q.; Cheng, L.; Liu, C.; Zhang, M.; Feng, Q.; Ye, H.; Zeng, M.; Xie, L.; Liu, Z.; Li, Y. Ultrathin MoS2(1-x)Se2x Alloy Nanoflakes for Electrocatalytic Hydrogen Evolution Reaction. *ACS Catal.* **2015**, *5* (4), 2213–2219. https://doi.org/10.1021/cs501970w.

(171) Konkena, B.; Masa, J.; Xia, W.; Muhler, M.; Schuhmann, W. MoSSe@reduced Graphene Oxide Nanocomposite Heterostructures as Efficient and Stable Electrocatalysts for the Hydrogen Evolution Reaction. *Nano Energy* **2016**, *29*, 46–53.

https://doi.org/10.1016/j.nanoen.2016.04.018.

(172) Lin, J.; Zhou, J.; Zuluaga, S.; Yu, P.; Gu, M.; Liu, Z.; Pantelides, S. T.; Suenaga, K. Anisotropic Ordering in 1T' Molybdenum and Tungsten Ditelluride Layers Alloyed with Sulfur and Selenium. *ACS Nano* **2018**, *12* (1), 894–901. https://doi.org/10.1021/acsnano.7b08782.

(173) Sarwar, S.; Ali, A.; Wang, Y.; Ahasan, M. R.; Wang, R.; Adamczyk, A. J.; Zhang, X. Enhancement of Hydrogen Evolution Reaction Activity Using Metal–rich Molybdenum Sulfotelluride with Graphene Support: A Combined Experimental and Computational Study. *Nano Energy* **2021**, *90* (Part B), 106599. https://doi.org/10.1016/j.nanoen.2021.106599.

(174) Sabatier, P. Hydrogénations et Déshydrogénations Par Catalyse. *Berichte der Dtsch. Chem. Gesellschaft* **1911**, *44* (3), 1984–2001. https://doi.org/10.1002/cber.19110440303.

(175) Sabatier, P. *La Catalyse En Chimie Organique*; Paris ; Liége : C. Béranger, 1913.

(176) Grabow, L. C. Computational Catalyst Screening. In *Computational Catalysis*; Asthagiri, A., Janik, M. J., Eds.; The Royal Society of Chemistry, 2014; pp 1–58.

(177) Sabatier, P.; Reid (Translator), E. E. *Catalysis in Organic Chemistry*; D. Van Nostrand Company: New York, 1922.

(178) Lindgren, P.; Kastlunger, G.; Peterson, A. A. A Challenge to the ΔG~0 Interpretation of Hydrogen Evolution. *ACS Catal.* **2020**, *10* (1), 121–128. https://doi.org/10.1021/acscatal.9b02799.

(179) Exner, K. S. Is Thermodynamics a Good Descriptor for the Activity? Re-Investigation of Sabatier's Principle by the Free Energy Diagram in Electrocatalysis. *ACS Catal.* **2019**, *9* (6), 5320–5329. https://doi.org/10.1021/acscatal.9b00732.

(180) Trasatti, S. Work Function, Electronegativity, and Electrochemical Behaviour of Metals. III. Electrolytic Hydrogen Evolution in Acid Solutions. *J. Electroanal. Chem.* **1972**, *39* (1), 163–184. https://doi.org/10.1016/S0022-0728(72)80485-6.

(181) Perdew, J. P.; Chevary, J. A.; Vosko, S. H.; Jackson, K. A.; Pederson, M. R.; Singh, D. J.; Fiolhais, C. Atoms, Molecules, Solids, and Surfaces: Applications of the Generalized Gradient Approximation for Exchange and Correlation. *Phys. Rev. B* **1992**, *46* (11), 6671–6687. https://doi.org/10.1103/PhysRevB.46.6671.

(182) Santos, E.; Schmickler, W. Recent Advances in Theoretical Aspects of Electrocatalysts. In *Theory and Experiment in Electrolysis*; Balbuena, P. B., Subramanian, V. R., Eds.; Springer, 2010; pp 25–88.

(183) Zeradjanin, A. R.; Grote, J. P.; Polymeros, G.; Mayrhofer, K. J. J. A Critical Review on Hydrogen Evolution Electrocatalysis: Re-Exploring the Volcano-Relationship. *Electroanalysis* **2016**, *28* (10), 2256–2269. https://doi.org/10.1002/elan.201600270.

(184) Adamczyk, A. J. First-Principles Analysis of Acetonitrile Reaction Pathways to Primary, Secondary, and Tertiary Amines on Pd(111). *Surf. Sci.* **2019**, *682* (111), 84–98. https://doi.org/10.1016/j.susc.2018.09.006.

(185)   Lozano-Blanco, G.; Adamczyk, A. J. Cobalt-Catalyzed Nitrile Hydrogenation: Insights into the Reaction Mechanism and Product Selectivity from DFT Analysis. *Surf. Sci.* **2019**, *688* (June), 31–44. https://doi.org/10.1016/j.susc.2019.06.003.

(186)   Wu, S.; Tatarchuk, B. J.; Adamczyk, A. J. Ethylene Oxidation on Unpromoted Silver Catalysts: Reaction Pathway and Selectivity Analysis Using DFT Calculations. *Surf. Sci.* **2021**, *708* (February), 121834. https://doi.org/10.1016/j.susc.2021.121834.

(187)   Murthy, A. P.; Theerthagiri, J.; Madhavan, J. Insights on Tafel Constant in the Analysis of Hydrogen Evolution Reaction. *J. Phys. Chem. C* **2018**, *122* (42), 23943–23949. https://doi.org/10.1021/acs.jpcc.8b07763.

(188)   Cheng, J.; Hu, P.; Ellis, P.; French, S.; Kelly, G.; Lok, C. M. Brønsted-Evans-Polanyi Relation of Multistep Reactions and Volcano Curve in Heterogeneous Catalysis. *J. Phys. Chem. C* **2008**, *112* (5), 1308–1311. https://doi.org/10.1021/jp711191j.

(189)   Nørskov, J. K.; Bligaard, T.; Logadottir, A.; Bahn, S.; Hansen, L. B.; Bollinger, M.; Bengaard, H.; Hammer, B.; Sljivancanin, Z.; Mavrikakis, M.; Xu, Y.; Dahl, S.; Jacobsen, C. J. H. Universality in Heterogeneous Catalysis. *J. Catal.* **2002**, *209* (2), 275–278. https://doi.org/10.1006/jcat.2002.3615.

(190)   Yeh, K.-Y.; Janik, M. J. Density Functional Theory Methods for Electrocatalysis. In *Computational Catalysis*; Asthagiri, A., Janik, M. J., Eds.; The Royal Society of Chemistry, 2014; pp 116–156.

(191)   Kioseoglou, G.; Hanbicki, A. T.; Currie, M.; Friedman, A. L.; Jonker, B. T. Optical Polarization and Intervalley Scattering in Single Layers of MoS 2 and MoSe 2. *Sci. Rep.* **2016**, *6* (April), 1–8. https://doi.org/10.1038/srep25041.

(192)   Pan, Y.; Zheng, F.; Wang, X.; Qin, H.; Liu, E.; Sha, J.; Zhao, N.; Zhang, P.; Ma, L. Enhanced Electrochemical Hydrogen Evolution Performance of WS2 Nanosheets by Te Doping. *J. Catal.* **2020**, *382*, 204–211. https://doi.org/10.1016/j.jcat.2019.12.031.

(193)   Ma, N.; Jiang, X. Y.; Zhang, L.; Wang, X. S.; Cao, Y. L.; Zhang, X. Z. Novel 2D Layered Molybdenum Ditelluride Encapsulated in Few-Layer Graphene as High-Performance Anode for Lithium-Ion Batteries. *Small* **2018**, *14* (14), 1–8. https://doi.org/10.1002/smll.201703680.

(194)   Liu, M.; Lu, X.; Guo, C.; Wang, Z.; Li, Y.; Lin, Y.; Zhou, Y.; Wang, S.; Zhang, J. Architecting a Mesoporous N-Doped Graphitic Carbon Framework Encapsulating CoTe2 as an Efficient Oxygen Evolution Electrocatalyst. *ACS Appl. Mater. Interfaces* **2017**, *9* (41), 36146–36153. https://doi.org/10.1021/acsami.7b09897.

(195)   Xin, Y.; Li, S.; Qian, Y.; Zhu, W.; Yuan, H.; Jiang, P.; Guo, R.; Wang, L. High-Entropy Alloys as a Platform for Catalysis : Progress , Challenges , and Opportunities. **2020**. https://doi.org/10.1021/acscatal.0c03617.

(196)   Altaf, S.; Haider, A.; Naz, S.; Ul-Hamid, A.; Haider, J.; Imran, M.; Shahzadi, A.; Naz, M.; Ajaz, H.; Ikram, M. Comparative Study of Selenides and Tellurides of Transition Metals (Nb and Ta) with Respect to Its Catalytic, Antimicrobial, and Molecular Docking Performance. *Nanoscale Res. Lett.* **2020**, *15* (1). https://doi.org/10.1186/s11671-020-03375-0.

(197) Exner, K. S. Does a Thermoneutral Electrocatalyst Correspond to the Apex of a Volcano Plot for a Simple Two-Electron Process? *Angew. Chemie* **2020**, *59* (26), 10236–10240. https://doi.org/10.1002/ange.202003688.

(198) Exner, K. S. Beyond the Traditional Volcano Concept: Overpotential-Dependent Volcano Plots Exemplified by the Chlorine Evolution Reaction over Transition-Metal Oxides. *J. Phys. Chem. C* **2019**, *123* (27), 16921–16928. https://doi.org/10.1021/acs.jpcc.9b05364.

(199) Ursua, A.; Sanchis, P.; Gandia, L. M. Hydrogen Production from Water Electrolysis : Current Status and Future Trends. *Proc. IEEE* **2012**, *100* (2), 410–426.

(200) Chi, J.; Yu, H. Water Electrolysis Based on Renewable Energy for Hydrogen Production. *Cuihua Xuebao/Chinese J. Catal.* **2018**, *39* (3), 390–394. https://doi.org/10.1016/S1872-2067(17)62949-8.

(201) Shiva Kumar, S.; Himabindu, V. Hydrogen Production by PEM Water Electrolysis – A Review. *Mater. Sci. Energy Technol.* **2019**, *2* (3), 442–454. https://doi.org/10.1016/j.mset.2019.03.002.

(202) Li, A.; Sun, Y.; Yao, T.; Han, H. Earth-Abundant Transition-Metal-Based Electrocatalysts for Water Electrolysis to Produce Renewable Hydrogen. *Chem. - A Eur. J.* **2018**, *24* (69), 18334–18355. https://doi.org/10.1002/chem.201803749.

(203) Eftekhari, A. Electrocatalysts for Hydrogen Evolution Reaction. *Int. J. Hydrogen Energy* **2017**, *42* (16), 11053–11077. https://doi.org/10.1016/j.ijhydene.2017.02.125.

(204) Zheng, Y.; Jiao, Y.; Zhu, Y.; Li, L. H.; Han, Y.; Chen, Y.; Jaroniec, M.; Qiao, S. Z. High Electrocatalytic Hydrogen Evolution Activity of an Anomalous Ruthenium Catalyst. *J. Am. Chem. Soc.* **2016**, *138* (49), 16174–16181. https://doi.org/10.1021/jacs.6b11291.

(205) Smiljanic, M.; Rakocevic, Z.; Maksic, A.; Strbac, S. Hydrogen Evolution Reaction on Platinum Catalyzed by Palladium and Rhodium Nanoislands. *Electrochim. Acta* **2014**, *117*, 336–343. https://doi.org/10.1016/j.electacta.2013.11.142.

(206) Zhou, G.; Shan, Y.; Wang, L.; Hu, Y.; Guo, J.; Hu, F.; Shen, J.; Gu, Y.; Cui, J.; Liu, L.; Wu, X. Photoinduced Semiconductor-Metal Transition in Ultrathin Troilite FeS Nanosheets to Trigger Efficient Hydrogen Evolution. *Nat. Commun.* **2019**, *10* (1). https://doi.org/10.1038/s41467-019-08358-z.

(207) Wang, R.; Han, J.; Zhang, X.; Song, B. Synergistic Modulation in MX2 (Where M = Mo or W or V, and X = S or Se) for an Enhanced Hydrogen Evolution Reaction. *J. Mater. Chem. A* **2018**, *6* (44), 21847–21858. https://doi.org/10.1039/c8ta05912h.

(208) Majhi, K. C.; Yadav, M. Transition Metal Chalcogenides Based Nanocomposites as Efficient Electrocatalyst for Hydrogen Evolution Reaction over the Entire PH Range. *Int. J. Hydrogen Energy* **2020**, *45* (46), 24219–24231. https://doi.org/10.1016/j.ijhydene.2020.06.230.

(209) Bhat, K. S.; Nagaraja, H. S. Performance Evaluation of Molybdenum Dichalcogenide (MoX2; X= S, Se, Te) Nanostructures for Hydrogen Evolution Reaction. *Int. J. Hydrogen Energy* **2019**, *44* (33), 17878–17886. https://doi.org/10.1016/j.ijhydene.2019.05.179.

(210) Du, H.; Kong, R. M.; Guo, X.; Qu, F.; Li, J. Recent Progress in Transition Metal Phosphides

155

with Enhanced Electrocatalysis for Hydrogen Evolution. *Nanoscale* **2018**, *10* (46), 21617–21624. https://doi.org/10.1039/c8nr07891b.

(211) Shi, Y.; Zhang, B. Recent Advances in Transition Metal Phosphide Nanomaterials: Synthesis and Applications in Hydrogen Evolution Reaction. *Chem. Soc. Rev.* **2016**, *45* (6), 1529–1541. https://doi.org/10.1039/c5cs00434a.

(212) Meyer, S.; Nikiforov, A. V.; Petrushina, I. M.; Köhler, K.; Christensen, E.; Jensen, J. O.; Bjerrum, N. J. Transition Metal Carbides (WC, Mo2C, TaC, NbC) as Potential Electrocatalysts for the Hydrogen Evolution Reaction (HER) at Medium Temperatures. *Int. J. Hydrogen Energy* **2015**, *40* (7), 2905–2911. https://doi.org/10.1016/j.ijhydene.2014.12.076.

(213) Chen, W. F.; Muckerman, J. T.; Fujita, E. Recent Developments in Transition Metal Carbides and Nitrides as Hydrogen Evolution Electrocatalysts. *Chem. Commun.* **2013**, *49* (79), 8896–8909. https://doi.org/10.1039/c3cc44076a.

(214) Li, Y.; Yu, Y.; Huang, Y.; Nielsen, R. A.; Goddard, W. A.; Li, Y.; Cao, L. Engineering the Composition and Crystallinity of Molybdenum Sulfide for High-Performance Electrocatalytic Hydrogen Evolution. *ACS Catal.* **2015**, *5* (1), 448–455. https://doi.org/10.1021/cs501635v.

(215) Park, S. K.; Kim, J. K.; Kang, Y. C. Amorphous Molybdenum Sulfide on Three-Dimensional Hierarchical Hollow Microspheres Comprising Bamboo-like N-Doped Carbon Nanotubes as a Highly Active Hydrogen Evolution Reaction Catalyst. *ACS Sustain. Chem. Eng.* **2018**, *6* (10), 12706–12715. https://doi.org/10.1021/acssuschemeng.8b01843.

(216) Xie, S.; Sun, B.; Sun, H.; Zhan, K.; Zhao, B.; Yan, Y.; Xia, B. Y. Engineering of Molybdenum Sulfide Nanostructures towards Efficient Electrocatalytic Hydrogen Evolution. *Int. J. Hydrogen Energy* **2019**, *44* (29), 15009–15016. https://doi.org/10.1016/j.ijhydene.2019.04.106.

(217) Du, C.; Huang, H.; Jian, J.; Wu, Y.; Shang, M.; Song, W. Enhanced Electrocatalytic Hydrogen Evolution Performance of MoS2 Ultrathin Nanosheets via Sn Doping. *Appl. Catal. A Gen.* **2017**, *538*, 1–8. https://doi.org/10.1016/j.apcata.2017.03.010.

(218) Ghorbani-Asl, M.; Kretschmer, S.; Spearot, D. E.; Krasheninnikov, A. V. Two-Dimensional MoS2 under Ion Irradiation: From Controlled Defect Production to Electronic Structure Engineering. *2D Mater.* **2017**, *4* (2). https://doi.org/10.1088/2053-1583/aa6b17.

(219) Zhao, G.; Rui, K.; Dou, S. X.; Sun, W. Heterostructures for Electrochemical Hydrogen Evolution Reaction: A Review. *Adv. Funct. Mater.* **2018**, *28* (43), 1–26. https://doi.org/10.1002/adfm.201803291.

(220) Li, M.; Yu, M.; Li, X. Improving the Catalytic Activity of Amorphous Molybdenum Sulfide for Hydrogen Evolution Reaction Using Polydihydroxyphenylalanine Modified MWCNTs. *Appl. Surf. Sci.* **2018**, *439*, 343–349. https://doi.org/10.1016/j.apsusc.2018.01.063.

(221) Ou, G.; Fan, P.; Ke, X.; Xu, Y.; Huang, K.; Wei, H.; Yu, W.; Zhang, H.; Zhong, M.; Wu, H.; Li, Y. Defective Molybdenum Sulfide Quantum Dots as Highly Active Hydrogen Evolution Electrocatalysts. *Nano Res.* **2018**, *11* (2), 751–761. https://doi.org/10.1007/s12274-017-1684-2.

(222) Shi, W.; Li, G.; Wang, Z. Triggering Catalytic Active Sites for Hydrogen Evolution Reaction by Intrinsic Defects in Janus Monolayer MoSSe. *J. Phys. Chem. C* **2019**, *123* (19), 12261–12267. https://doi.org/10.1021/acs.jpcc.9b01485.

(223) Yuan, J.; Shan, Y.; Li, T. Electronic Structure and Hydrogen Evolution Reaction in Janus Monolayer MoSSe Regulated by Strain Engineering. *J. Phys. D. Appl. Phys.* **2020**, *53* (12). https://doi.org/10.1088/1361-6463/ab622e.

(224) Li, S.; Zang, W.; Liu, X.; Pennycook, S. J.; Kou, Z.; Yang, C.; Guan, C.; Wang, J. Heterojunction Engineering of MoSe2/MoS2 with Electronic Modulation towards Synergetic Hydrogen Evolution Reaction and Supercapacitance Performance. *Chem. Eng. J.* **2019**, *359* (November 2018), 1419–1426. https://doi.org/10.1016/j.cej.2018.11.036.

(225) Zhang, J.; Jia, S.; Kholmanov, I.; Dong, L.; Er, D.; Chen, W.; Guo, H.; Jin, Z.; Shenoy, V. B.; Shi, L.; Lou, J. Janus Monolayer Transition-Metal Dichalcogenides. *ACS Nano* **2017**, *11* (8), 8192–8198. https://doi.org/10.1021/acsnano.7b03186.

(226) Yang, J.; Liu, Y.; Shi, C.; Zhu, J.; Yang, X.; Liu, S.; Li, L.; Xu, Z.; Zhang, C.; Liu, T. Carbon Nanotube with Vertical 2D Molybdenum Sulphoselenide Nanosheet Arrays for Boosting Electrocatalytic Hydrogen Evolution. *ACS Appl. Energy Mater.* **2018**, *1* (12), 7035–7045. https://doi.org/10.1021/acsaem.8b01466.

(227) Yang, H.; Zhang, T.; Zhu, H.; Zhang, M.; Wu, W. W.; Du, M. L. Synthesis of a MoS2(1−x)Se2x Ternary Alloy on Carbon Nanofibers as the High Efficient Water Splitting Electrocatalyst. *Int. J. Hydrogen Energy* **2017**, *42* (4), 1912–1918. https://doi.org/10.1016/j.ijhydene.2016.10.075.

(228) Hussain, S.; Patil, S. A.; Vikraman, D.; Rabani, I.; Arbab, A. A.; Jeong, S. H.; Kim, H. S.; Choi, H.; Jung, J. Enhanced Electrocatalytic Properties in MoS2/MoTe2 Hybrid Heterostructures for Dye-Sensitized Solar Cells. *Appl. Surf. Sci.* **2020**, *504* (October 2019), 144401. https://doi.org/10.1016/j.apsusc.2019.144401.

(229) Yagmurcukardes, M.; Sevik, C.; Peeters, F. M. Electronic, Vibrational, Elastic, and Piezoelectric Properties of Monolayer Janus MoSTe Phases: A First-Principles Study. *Phys. Rev. B* **2019**, *100* (4), 1–8. https://doi.org/10.1103/PhysRevB.100.045415.

(230) Idrees, M.; Din, H. U.; Ali, R.; Rehman, G.; Hussain, T.; Nguyen, C. V.; Ahmad, I.; Amin, B. Optoelectronic and Solar Cell Applications of Janus Monolayers and Their van Der Waals Heterostructures. *Phys. Chem. Chem. Phys.* **2019**, *21* (34), 18612–18621. https://doi.org/10.1039/c9cp02648g.

(231) Srivastava, G. P.; Weaire, D. The Theory of the Cohesive Energies of Solids. *Adv. Phys.* **1987**, *36* (4), 463–517.

(232) Lozano-Blanco, G.; Adamczyk, A. J. Reaction Mechanisms and Microkinetic Modeling of Nitrile Hydrogenation to Higher Amines on Pd (111) and Co (0001) Surfaces. In *National Meeting of the American Chemical Society*; Orlando, 2019.

(233) Lozano-Blanco, G.; Tatarchuk, B. J.; Adamczyk, A. J. Building a Microkinetic Model from First Principles for Higher Amine Synthesis on Pd Catalyst. *Ind. Eng. Chem. Res.* **2019**, *58* (41), 19022–19032. https://doi.org/10.1021/acs.iecr.9b03577.

(234) Ali, A.; Sarwar, S.; Pollard, D. R.; Wei, Z.; Wan, R.; Zhang, X.; Adamczyk, A. J. A Systematic

Mapping of Electrocatalytic Descriptors for Hybrid and Non-Hybrid Molybdenum Dichalcogenides with Graphene Support for Cathodic Hydrogen Generation. *J. Phys. Chem. C* **2022**.

(235)   Payne, M. C.; Teter, M. P.; Allan, D. C.; Arias, T. A.; Joannopoulos, J. D. Iterative Minimization Techniques for Ab Initio Total-Energy Calculations: Molecular Dynamics and Conjugate Gradients. *Rev. Mod. Phys.* **1992**, *64* (4), 1045–1097. https://doi.org/10.1103/RevModPhys.64.1045.

(236)   Sun, H.; Ma, Z.; Qiu, Y.; Liu, H.; Gao, G. gang. Ni@NiO Nanowires on Nickel Foam Prepared via "Acid Hungry" Strategy: High Supercapacitor Performance and Robust Electrocatalysts for Water Splitting Reaction. *Small* **2018**, *14* (31), 1–12. https://doi.org/10.1002/smll.201800294.

(237)   Tanford, C.; Roxby, R. Interpretation of Protein Titration Curves. Application to Lysozyme. *Biochemistry* **1972**, *11* (11), 2192–2198. https://doi.org/10.1021/bi00761a029.

(238)   Polydorides, S.; Simonson, T. Monte Carlo Simulations of Proteins at Constant PH with Generalized Born Solvent, Flexible Sidechains, and an Effective Dielectric Boundary. *J. Comput. Chem.* **2013**, *34* (31), 2742–2756. https://doi.org/10.1002/jcc.23450.

(239)   Sham, Y. Y.; Chu, Z. T.; Warshel, A. Consistent Calculations of PKa's of Ionizable Residues in Proteins: Semi-Microscopic and Microscopic Approaches. *J. Phys. Chem. B* **1997**, *101* (22), 4458–4472. https://doi.org/10.1021/jp963412w.

(240)   Lu, H.; Diaz, D. J.; Czarnecki, N. J.; Zhu, C.; Kim, W.; Shroff, R.; Acosta, D. J.; Alexander, B. R.; Cole, H. O.; Zhang, Y.; Lynd, N. A.; Ellington, A. D.; Alper, H. S. Machine Learning-Aided Engineering of Hydrolases for PET Depolymerization. *Nature* **2022**, *604* (7907), 662–667. https://doi.org/10.1038/s41586-022-04599-z.

(241)   Mazurenko, S.; Prokop, Z.; Damborsky, J. Machine Learning in Enzyme Engineering. *ACS Catal.* **2020**, *10* (2), 1210–1223. https://doi.org/10.1021/acscatal.9b04321.

(242)   Yan, X.; Javed, R.; Gong, Y.; Ye, D.; Zhao, H. Fundamentals of Water Electrolysis. In *Electrochemical Water Electrolysis: Fundamentals and Technologies*; Zhang;, L., Zhao;, H., Wilkinson, D. P., Sun, X., Zhnag, J., Eds.; CRC Press, Taylor and Francis Group, 2020; pp 1–26. https://doi.org/10.1201/9780429447884.

(243)   Kastlunger, G.; Lindgren, P.; Peterson, A. A. Controlled-Potential Simulation of Elementary Electrochemical Reactions: Proton Discharge on Metal Surfaces. *J. Phys. Chem. C* **2018**, *122* (24), 12771–12781. https://doi.org/10.1021/acs.jpcc.8b02465.

(244)   Enyo, M.; Yokoyama, T. The Hydrogen-Electrode Reaction in the Isotopically Mixed System-I. The Relation between Forward and Backward Unidirectional Rates and Evaluation of the Stoichiometric Number of the Rate-Determining Step. *Electrochim. Acta* **1967**, *12* (12), 1631–1639. https://doi.org/10.1016/0013-4686(67)80077-X.

(245)   Laidler, K. J.; Glasstone, S.; Eyring, H. Application of the Theory of Absolute Reaction Rates to Heterogeneous Processes. II. Chemical Reactions on Surfaces. *J. Chem. Phys.* **1940**, *8* (9), 667–676. https://doi.org/10.1063/1.1750737.

(246)   Hillson, P. J.; Rideal, E. K. On Overpotential and the Photovoltaic Process at Polarized Electrodes. *Proc. R. Soc. London. Ser. A. Math. Phys. Sci.* **1949**, *199* (1058), 295–310.

https://doi.org/10.1098/rspa.1949.0139.

(247) Zhang, J.; Hu, P.; Wang, H. Amorphous Catalysis: Machine Learning Driven High-Throughput Screening of Superior Active Site for Hydrogen Evolution Reaction. *J. Phys. Chem. C* **2020**, *124* (19), 10483–10494. https://doi.org/10.1021/acs.jpcc.0c00406.

(248) Sun, X.; Zheng, J.; Gao, Y.; Qiu, C.; Yan, Y.; Yao, Z.; Deng, S.; Wang, J. Machine-Learning-Accelerated Screening of Hydrogen Evolution Catalysts in MBenes Materials. *Appl. Surf. Sci.* **2020**, *526* (May), 146522. https://doi.org/10.1016/j.apsusc.2020.146522.

(249) Wu, S.; Wang, Z.; Zhang, H.; Cai, J.; Li, J. Deep Learning Accelerates the Discovery of Two-Dimensional Catalysts for Hydrogen Evolution Reaction. *Energy Environ. Mater.* **2021**, 1–7. https://doi.org/10.1002/eem2.12259.

(250) Choi, Y.; Adamczyk, A. J. Tuning Hydrogenated Silicon, Germanium, and SiGe Nanocluster Properties Using Theoretical Calculations and a Machine Learning Approach. *J. Phys. Chem. A* **2018**, *122* (51), 9851–9868. https://doi.org/10.1021/acs.jpca.8b09797.

(251) Choi, Y.; Preston, T. J.; Adamczyk, A. J. Data-Driven Investigation of Monosilane and Ammonia Co-Pyrolysis to Silicon-Nitride-Based Ceramic Nanomaterials. *ChemPhysChem* **2020**, *21* (22), 2627–2642. https://doi.org/10.1002/cphc.202000561.

(252) Choi, Y.; Adamczyk, A. J. Competitive Hydrogen Migration in Silicon Nitride Nanoclusters: Reaction Kinetics Generalized from Supervised Machine Learning. *J. Phys. Chem. A* **2022**, *126* (17), 2677–2689. https://doi.org/10.1021/acs.jpca.2c01050.

(253) Zheng, J.; Sun, X.; Hu, J.; Wang, S.; Yao, Z.; Deng, S.; Pan, X.; Pan, Z.; Wang, J. Symbolic Transformer Accelerating Machine Learning Screening of Hydrogen and Deuterium Evolution Reaction Catalysts in MA2Z4Materials. *ACS Appl. Mater. Interfaces* **2021**, *13* (43), 50878–50891. https://doi.org/10.1021/acsami.1c13236.

(254) Wang, X.; Wang, C.; Ci, S.; Ma, Y.; Liu, T.; Gao, L.; Qian, P.; Ji, C.; Su, Y. Accelerating 2D MXene Catalyst Discovery for the Hydrogen Evolution Reaction by Computer-Driven Workflow and an Ensemble Learning Strategy. *J. Mater. Chem. A* **2020**, *8* (44), 23488–23497. https://doi.org/10.1039/d0ta06583h.

(255) Liang, H.; Xu, M.; Asselin, E. A Study of Two-Dimensional Single Atom-Supported MXenes as Hydrogen Evolution Reaction Catalysts Using DFT and Machine Learning. *ChemRxiv* **2021**. https://doi.org/10.26434/chemrxiv.14566656.v1.